EXPERIMENTAL AND NUMERICAL INVESTIGATION OF TURBINE BLADE LEADING EDGE HEAT TRANSFER WITH JET IMPINGEMENT AND FILM COOLING

A Dissertation

by

MINGJIE ZHANG

Submitted to the Office of Graduate and Professional Studies of
Texas A&M University
in partial fulfillment of the requirements for the degree of

DOCTOR OF PHILOSOPHY

Chair of Committee,	Je-Chin Han
Committee Members,	Yassin A. Hassan
	Alan Palazzolo
	Sy-Bor Wen
Head of Department,	Andreas A. Polycarpou

December 2018

Major Subject: Mechanical Engineering

ABSTRACT

Modern gas turbines engines are designed with higher turbine inlet temperatures to increase the overall thermal efficiency and power output. Advanced cooling technologies are needed to protect turbine blades from hot gas and increase the lifetime of blades. The leading edge of turbine blades is subjected to very high heat loads. In order to reduce the temperature and increase the durability of turbine blades, film cooling and jet impingement cooling have been used in the leading edge portion. This study includes three topics: (1) influence of turbine blade leading edge profile on film cooling with shaped holes, (2) internal heat transfer of film-cooled leading edge model with normal and tangential impinging jets, (3) overall effectiveness of film-cooled leading edge model with normal and tangential impinging jets. The results provide baseline information for turbine blade leading edge cooling design and heat transfer analysis.

Topic 1 presents the turbine blade leading edge model film cooling effectiveness with shaped holes, using the pressure sensitive paint (PSP) mass transfer analogy method. The effects of leading edge profile, coolant to mainstream density ratio and blowing ratio are studied. Computational simulations are performed using the realizable k-ε turbulence model. Effectiveness obtained by CFD simulations are compared with experiments.

Topic 2 investigates turbine blade leading edge internal heat transfer for normal and tangential impinging jets with mainstream flow. Leading edge detailed internal heat transfer distributions are obtained. Experiments are carried out using transient liquid crystal method. CFD simulations using realizable k-ε (RKE) turbulence model are compared with experimental data.

Topic 3 studies turbine blade leading edge overall cooling effectiveness for normal and tangential impinging jets with mainstream flow. Pressure sensitive paint (PSP) technique is used

to measure the adiabatic effectiveness. Liquid crystal technique is used to obtain the overall effectiveness. Conjugate heat transfer simulations using realizable k-ε (RKE) turbulence model are applied to calculate the adiabatic effectiveness and overall effectiveness.

DEDICATION

To my parents

ACKNOWLEDGEMENTS

I would like to thank my committee chair, Dr. Han, and my committee members, Dr. Hassan, Dr. Palazzolo, and Dr. Wen. I am extremely grateful to Dr. Han for his guidance, advice and support throughout my course and research in Texas A&M University.

I would also like to thank Nian Wang, Andrew F Chen, and my colleagues in the Turbine Heat Transfer Laboratory. Thanks to the faculty and staff in the Department of Mechanical Engineering. This thesis cannot be completed without their help and support.

CONTRIBUTORS AND FUNDING SOURCES

Contributors

This work was supported by a thesis (or) dissertation committee consisting of Professor Je-Chin Han, Professor Alan Palazzolo and Professor Sy-Bor Wen of the Department of Mechanical Engineering and Professor Yassin A. Hassan of the Department of Nuclear Engineering.

All work for the thesis (or) dissertation was completed by the student, in collaboration with Nian Wang and Andrew F Chen of the Department of Mechanical Engineering.

Funding Sources

This work was supported through the Marcus Easterling endowment fund. The numerical simulations were supported by High Performance Research Computing of Texas A&M University.

NOMENCLATURE

Bi	Biot number
d	Diameter of hole
d_c	Diameter of film cooling hole
d_j	Diameter of jet impinging hole
D	Diameter of the semi cylinder model
DR	Coolant-to-mainstream density ratio = ρ_c / ρ_m
h	Heat transfer coefficient ($W/m^2 \cdot K$)
I	Emission intensity of PSP
k	Gas thermal conductivity ($W/m \cdot K$)
K	Solid material thermal conductivity ($W/m \cdot K$)
M	Blowing ratio = $\rho_c v_c / \rho_m v_m$
Nu	Nusselt number, $Nu = h_j d_j / k$
p	Hole pitch
P	Static pressure
R	Radius of the semi-cylinder model
Re_j	Reynolds number, $Re_j = \rho V_j d_j / \mu$
s	Distance from the stagnation line (arc length)
T	Temperature (K)
t	Time (s)
Tu	Turbulence intensity
V	Velocity (m/s)

W	Molecular weight
X	Span-wise direction
y+	Non-dimensional wall distance

α	Film cooling hole inclination angle to the surface
η	Film cooling effectiveness or adiabatic effectiveness
ϕ	Overall effectiveness
θ	Dimensionless temperature
ρ	Fluid density (kg/m^3)
μ	Fluid dynamic viscosity (Pa·s)

air	Property with air injection
blk	Black or dark condition
c	Coolant
i	Initial
j	Jet
∞, m	Mainstream
mix	Property with foreign gas injection
ref	Reference condition
w	Wall

TABLE OF CONTENTS

Page

ABSTRACT ii

DEDICATION iv

ACKNOWLEDGEMENTS v

CONTRIBUTORS AND FUNDING SOURCES vi

NOMENCLATURE vii

TABLE OF CONTENTS ix

LIST OF FIGURES xi

LIST OF TABLES xv

1. INTRODUCTION 1

    1.1 Literature Review on Influence of Blade Leading Edge Profile 1
    1.2 Literature Review on Internal Heat Transfer of Film-Cooled Leading Edge 4
    1.3 Literature Review on Conjugate Heat Transfer of Film-Cooled Leading Edge 7
    1.4 Objective of the Study 10

2. INFLUENCE OF TURBINE BLADE LEADING EDGE PROFILE ON FILM COOLING WITH SHAPED HOLES 12

    2.1 Experimental Setup and Method 12
    2.2 Numerical Setup and Method 21
    2.3 Experimental Results and Discussion 23
    2.4 Numerical Results and Discussion 31
    2.5 Conclusions 43

3. INTERNAL HEAT TRANSFER OF FILM-COOLED LEADING EDGE MODEL WITH NORMAL AND TANGENTIAL IMPINGING JETS 44

    3.1 Experimental Setup and Method 44
    3.2 Numerical Setup and Method 54
    3.3 Experimental Results and Discussion 61
    3.4 Numerical Results and Discussion 68
    3.5 Conclusions 79

Page

4. OVERALL EFFECTIVENESS OF FILM-COOLED LEADING EDGE MODEL WITH NORMAL AND TANGENTIAL IMPINGING JETS 80

4.1 Experimental Setup and Method 80
4.2 Numerical Setup and Method 95
4.3 Experimental Results and Discussion 98
4.4 Numerical Results and Discussion 110
4.5 Conclusions 122

5. SUMMARY 123

REFERENCES 124

LIST OF FIGURES

Page

Figure 1 Schematic diagram of the test facility and test section. 14

Figure 2 Leading edge models and shaped holes configuration. 15

Figure 3 Schematic of leading edge film cooling with adiabatic wall. 18

Figure 4 PSP calibration curves. 19

Figure 5 Schematic of computational domain and grid. 22

Figure 6 Film cooling effectiveness contour plot for 1.0*R*. 25

Figure 7 Film cooling effectiveness contour plot at *DR* = 1.5. 26

Figure 8 Effect of blowing ratio on span-wise averaged film cooling effectiveness. 28

Figure 9 Effect of density ratio on span-wise averaged film cooling effectiveness. 29

Figure 10 Effect of leading edge profile on span-wise averaged film cooling effectiveness. 29

Figure 11 Area averaged film cooling effectiveness. 30

Figure 12 Leading edge span-wise averaged static pressure distributions. 32

Figure 13 Static pressure contours. 34

Figure 14 Velocity magnitude contours and streamlines. 34

Figure 15 Coolant path lines and dimensionless temperature. 35

Figure 16 Mass flow rates for *DR* = 1.5. 36

Figure 17 Local blowing ratios for *DR* = 1.5. 36

Figure 18 CFD predicted and PSP measured span-wise averaged film cooling effectiveness. 38

Figure 19 CFD predicted span-wise averaged effectiveness for 1.0R and 2.0R profiles. 38

Figure 20 Mass flow rates for 1.0R profile. 40

Figure 21 Local blowing ratios for 1.0R profile. 40

Page

Figure 22 Film cooling effectiveness contour plot for 1.0R M1.5. 42

Figure 23 CFD predicted and PSP measured span-wise averaged film cooling effectiveness.... 42

Figure 24 Geometry of the leading edge model..... 45

Figure 25 Schematic of experimental setup..... 48

Figure 26 Jet inlet temperature as functions of time..... 50

Figure 27 Schematic of the liquid crystal calibration and camera view. 51

Figure 28 Liquid crystal calibration curves. 52

Figure 29 Schematic of CFD geometry with unstructured mesh..... 56

Figure 30 Schematic of computational domain for the normal jet. 57

Figure 31 Grid independent test. RKE model..... 58

Figure 32 Comparison of span-wise averaged Nu between TLC, RKE and SST. 59

Figure 33 Nu contours by SST model..... 60

Figure 34 Nusselt number contours - TLC normal jet..... 62

Figure 35 Nusselt number contours - TLC tangential jet. 63

Figure 36 Span-wise averaged Nu – TLC..... 65

Figure 37 Stream-wise averaged Nu - TLC..... 67

Figure 38 Velocity magnitude contours and streamlines..... 70

Figure 39 Local blowing ratio distribution. 71

Figure 40 Nusselt number contours – RKE. 73

Figure 41 Span-wise averaged Nu - TLC and RKE. 74

Figure 42 Stream-wise averaged Nu – RKE..... 75

Figure 43 Area averaged Nu on leading edge internal surface. 75

Page

Figure 44 Nu contour on the film cooling hole surface for the normal jet. 76

Figure 45 Nu contour on the film cooling hole surface for the tangential jet. 77

Figure 46 Area averaged Nu on film cooling hole surface. 78

Figure 47 Geometry of the leading edge model. 81

Figure 48 Schematic of experimental setup. 84

Figure 49 Schematic of leading edge conjugate heat transfer. 85

Figure 50 Camera view of test section and calibration. 87

Figure 51 Liquid crystal calibration curves. 88

Figure 52 Coolant temperature as functions of time. 90

Figure 53 Mainstream temperature as functions of time. 91

Figure 54 Span-wise averaged overall effectiveness at different time for the normal jet. 92

Figure 55 Span-wise averaged overall effectiveness at different time for the tangential jet. 93

Figure 56 Schematic of computational domain for the normal jet. 96

Figure 57 Adiabatic effectiveness contours. 100

Figure 58 Span-wise averaged adiabatic effectiveness. 101

Figure 59 Stream-wise averaged adiabatic effectiveness. 101

Figure 60 Overall effectiveness contours. 104

Figure 61 Span-wise averaged overall effectiveness. 105

Figure 62 Span-wise averaged overall effectiveness. 106

Figure 63 Stream-wise averaged overall effectiveness. 107

Figure 64 Comparison between measured adiabatic effectiveness and overall effectiveness ... 108

Figure 65 Comparison between measured adiabatic effectiveness and overall effectiveness ... 109

Page

Figure 66 Velocity magnitude contours and streamlines. 111

Figure 67 Adiabatic effectiveness contours for the normal jet. 113

Figure 68 Adiabatic effectiveness contours for the tangential jet. 114

Figure 69 Comparison of span-wise averaged effectiveness between experiments and CFD. . 115

Figure 70 Stream-wise averaged adiabatic effectiveness by CFD. 116

Figure 71 Overall effectiveness contours by simulations at M = 1.54 for the normal jet. 118

Figure 72 Overall effectiveness contours for the normal jet by simulations. 119

Figure 73 Overall effectiveness contours for the tangential jet by simulations. 120

Figure 74 Comparison of overall effectiveness between experiments and simulations. 121

LIST OF TABLES

Page

Table 1 Dimensions of cooling holes and leading edge models. 16

Table 2 Boundary conditions for the CFD model. 23

Table 3 Averaged total pressures and mass flow rate ratios for 1.0R profile. 40

Table 4 Dimensions of the leading edge model. 46

Table 5 CFD boundary conditions. 55

Table 6 Dimensions of the leading edge model. 82

Table 7 CFD boundary conditions. 97

Table 8 Averaged hf/hi and *Bi* for the normal jet and tangential jet. 98

1. INTRODUCTION

In modern gas turbine engines, advanced cooling technologies are needed to protect turbine blades from hot gases and increase the lifetime of blades. The leading edge of turbine blades is subjected to very high heat loads. In order to reduce the temperature and increase the durability of turbine blades, impinging cooling and film cooling have been used in the leading edge portion. Conjugate heat transfer has been widely used in gas turbine cooling designs, which combines film cooling, external and internal convective heat transfer, and solid conduction. Overall effectiveness, as the non-dimensional external surface temperature, is introduced to evaluate the conjugate heat transfer performance.

1.1 Literature Review on Influence of Blade Leading Edge Profile

Han et al. [1] documented many gas turbine cooling techniques. Among these techniques, film cooling is widely used in turbine blades under high temperature and high pressure conditions. Review articles on film cooling can be found in Bogard and Thole [2] and Han [3]. Goldstein et al. [4] pioneered in the research of film-hole geometry and coolant density effects on film cooling. Ekkad and Han [5] reviewed comprehensively the effects of film-hole geometry and coolant density on film cooling.

Several investigators simulated the airfoil leading edge film cooling using a cylinder with several film cooling rows such as Luckey et al. [6], Mick and Mayle [7]. Mehendale and Han [8] investigated the effect of free stream turbulence on heat transfer and film cooling effectiveness using a cylindrical leading edge model. They showed that the coolant jet traces are maintained over a longer distance at lower free stream turbulence. Ou et al. [9] presented the effect of film-

hole location and inclined film slots on the leading edge film cooling heat transfer using a cylindrical leading edge model. They showed that two-row injection (coolant flow doubled) performs better than one-row injection at a lower blowing ratio. Recently, some researchers studied leading edge film cooling with shaped holes. Reiss and Bölcs [10] investigated showerhead leading edge film cooling on a five-row cylinder model. Three configurations, including cylindrical holes, laidback holes, and fan-shaped holes were compared. Foreign gas (CO_2) was used yielding density ratio of 1.6. They found that laidback holes provided the best film cooling performance, due to better lateral spread and less tendency of jet detachment. Kim and Kim [11] studied a three-row leading edge model with cylindrical holes, laidback holes, and tear-drop shaped holes. The density ratio was nominally equal to 1. They found that laidback holes gave the best film cooling effectiveness. Mouzon et al. [12] studied a three-row leading edge model with cylindrical holes and laidback shaped holes. Shaped holes provided higher film cooling effectiveness and lower heat transfer coefficient, because of reduced interaction between the coolant and the mainstream. They found that shaped holes gave two to four times higher net heat flux reduction than cylindrical holes. Lu et al. [13] considered compound angle cylindrical holes and compound angle laidback fan-shaped holes on a three-row model. They also found that the shaped holes had much higher effectiveness than cylindrical holes.

Based on the heat and mass transfer analogy, the PSP technique is free from any thermal conduction error and is applicable to high curvature surfaces. Therefore, the PSP technique has been used to measure the film cooling effectiveness distributions on turbine blade leading edge, blade span, blade tips and end-wall region. Gao and Han [14] studied the effect of hole geometry and angle on blade leading edge film cooling using nitrogen as the coolant. They investigated three-row design and seven-row design to simulate turbine blade and turbine vane, and each design

has four different film cooling hole configurations, including radial angle cylindrical holes, compound angle cylindrical holes, radial angle shaped holes, and compound angle shaped holes. They found that shaped holes provided better film cooling effectiveness than cylindrical holes. Compared with compound angle holes, it was found that the coolant from radial angle holes can cover a wider range on the surface as the coolant is more deflected by the mainstream. Results showed that radial angle shaped holes gave the best film cooling effectiveness. Li et al. [15] studied coolant density effect on leading edge showerhead film cooling. They also investigated three-row design and seven-row design with four hole configurations, and coolant density ratio varies from 1.0, 1.5 to 2.0. Results showed that the density ratio effect is more evident for cylindrical holes than that for shaped holes, and radial angle shaped holes provided the best film cooling effectiveness at higher density ratio and blowing ratio conditions. In the present paper, radial angle shaped holes are used, as shaped holes with expanded film-hole exit area have better film cooling effectiveness compared with cylindrical holes.

In the open literature, most of the leading edge film cooling studies are based on the semi-cylindrical model. Cruse [16] et al. investigated various influences on turbine airfoil leading edge film cooling. They studied DR = 1.8, M = 2.0, Tu = 0.5% for circular and elliptical leading edge shapes with cylindrical holes. It was found that film cooling effectiveness distributions are similar. Chowdhury et al. [17] studied the leading edge shape effect on film cooling with radial angle cylindrical holes, including one semi-cylinder and two semi-ellipses leading edge. In the current study, cylindrical holes are changed to shaped holes. Compared with their results, we also found that shaped holes had much higher effectiveness than cylindrical holes for all the three leading edge shapes.

Many researchers numerically simulate leading edge film cooling using the realizable k-ε turbulence model. York and Leylek [18] studied film cooling on a turbine airfoil leading edge with diffused holes. Beimaert-Chartrel and Bogard [19] studied heat transfer coefficient augmentation of a three-row leading edge model with cylindrical holes. Rutledge and Polanka [20] studied the influence of fluid properties on a simulated turbine blade leading edge with one cylindrical hole. However, leading edge film cooling effectiveness comparisons with shaped hole designs between CFD and experiments are still limited in the open literature.

1.2 Literature Review on Internal Heat Transfer of Film-cooled Leading Edge

The leading edge of turbine blades is subjected to very high heat loads, in which jet impinging cooling have been widely used. Review articles can be found in [21-24]. Extensive works have been carried out to study the heat transfer performance and flow pattern inside the leading edge. Chupp et al. [25] made a correlation of leading edge jet impingement stagnation and averaged Nusselt number with jet Reynolds number from 3000 to 15000. Results showed that jet diameter, jet Reynolds number, jet-to-jet spacing, jet-to-target plate distance are important parameters that affect the heat transfer performance. Florschuetz et al. [26-28] made correlations of jet array impingement on a flat surface. They also point out that the cross flow can reduce the heat transfer performance. Metzger and Bunker [29-30] studied local heat transfer in turbine blade leading edge impingement cooling with and without film coolant extraction. Detailed surface Nusselt number distributions were obtained. Parameters including jet Reynolds number, leading edge sharpness, jet pitch-to-diameter ratio, and jet nozzle-to-apex distance were studied. Taslim et al. [31] studied leading edge impingement with and without showerhead and gill film holes. Jet Reynolds number ranges from 8000 to 48000. Numerical predictions of impingement heat transfer

coefficients using standard k-ε model for no-showerhead case agreed well with the experiment and showerhead case was under-predicted by 30%. Taslim et al. [32] experimentally and numerically studied the impingement heat transfer in the leading edge region with cross flow. Jet Reynolds numbers ranging from 8000 to 48000. It was found that cross flow can reduce the impingent heat transfer and the average difference between CFD and experiments ranges from 8% to 20%. Liu et al. [33] numerically investigated the effect of jet hole position on the leading edge impingement cooling, using k-ω SST turbulence model. The leading edge had one row of cylindrical impinging holes. Results shown that the averaged Nusselt number increases with the decreasing of the spacing between the jet hole position and the blade pressure side wall.

Transient liquid crystal method has been used by many researchers to study the leading edge internal heat transfer in order to obtain detailed heat transfer distributions. Huang et al. [34] studied an array of in-line circular jets impinging on a flat plate with Reynolds number from 4,800 to 18,300. They reported that the flow exit cross flow direction has a significant effect on the flow structure and heat transfer coefficient distributions on the target plate, and flow exiting in both sides can reduce the cross flow effect and obtain the highest heat transfer coefficients. Ekkad et al. [35] also studied an array of jets impinging on a target plate with film cooling holes and different exit flow orientations. The impinging holes are staggered with the film cooling holes. Jet Reynolds number ranges from 4000 to 20000. Results showed that with the film cooling holes, the cross flow effect decreased and the heat transfer on the surface increased. Jordan et al. [36-38] investigated jet impingement on a cylindrical surface with varying jet holes geometries. The effect of jet hole shape and hole inlet and exit conditions were studied. They found that the racetrack holes provide higher heat transfer compared with the cylindrical holes. For cylindrical jet holes, they studied the effects of impingement supply conditions and jet hole edge filleting degrees with

jet Reynolds number Re_j = 13600 and 27200. Results showed that cross flow can decrease Nusselt numbers on the target surface. In addition, jet hole with edge fillets can enhance or reduce the impingement heat transfer. Yang et al. [39] studied the effect of film cooling holes arrangement on leading edge impingement heat transfer. A 2/3 cylinder leading edge model with three arrays of film cooling holes was investigated. The film cooling holes position has a significant effect on the shape of high heat transfer zone in the stagnation region, and Nu in the stagnation region increases with decrease of pitch of film cooling holes. Numerical results using the SST model are comparable with experiments, and the heat transfer prediction difference is less than 15%.

Ling et al. [40] measured the heat transfer coefficients of a circular cooling passage with tangential injection by using the transient liquid crystal technique for jet Reynolds number from 7500 to 12500. The velocity field was measured by hot-wire anemometry. Results show that vortex cooling by tangential injection provides a more uniform heat transfer distribution in the axial direction and lower maximum heat transfer coefficient than the normal impingement cooling. At a low Reynolds number, the impingement cooling is more effective; at a high Reynolds number, the vortex cooling and impingement cooling are comparable. CFD prediction using k-ε turbulence model shows good agreement with the experimental data. In term of flow field prediction, the CFD simulations also showed a good agreement in near wall region but poor agreement near the core region.

Wang et al. [41] experimentally and numerically evaluated the leading edge impingement heat transfer by introducing one row of the normal or tangential jets with jet Reynolds number Re_j = 10000, 20000 and 30000. Transient liquid crystal method and RANS realizable k-ε model are used. A semi cylinder is used to simulate the leading edge surface. Jets through the impinging holes impinge on the semi cylinder and discharge from slots on the two sides. The heat transfer

contours on the test surface are significantly affected by the jet hole positions. The normal jet impingement produces circular Nu contour in the stagnation region, while, the tangential jet impingement produces the tear-drop contours. They also found that the tangential jet provides more uniform heat transfer distribution than the normal jet, and the area averaged Nusselt numbers are similar for the two jet hole positions. For normal jet impingement, CFD under-predicts the averaged Nu less than 10%; for tangential jet impingement, CFD predicts the heat transfer contour well but under-predicts the heat transfer about 20% at the jet entrance portion.

1.3 Literature Review on Conjugate Heat Transfer of Film-cooled Leading Edge

Conjugate heat transfer has been widely used in gas turbine cooling designs, which combines film cooling, external and internal convective heat transfer, and solid conduction. Overall effectiveness, as the non-dimensional external surface temperature, is introduced to evaluate the conjugate heat transfer performance. Hylton et al. [42-43] provided detailed surface temperature experimental data at the midspan of the Mark II and C3X vanes without film cooling. Turner et al. [44] experimentally measured surface temperature distributions of the C3X vanes with leading edge showerhead film cooling. Bohn et al. [45] numerically studied adiabatic effectiveness and conjugate heat transfer of a film-cooled duct wall for different configurations with cylindrical and shaped holes. The effect of conjugate heat transfer on the temperature field in the cooling film was studied. Results shown that the fan shaped configuration is up to three times effective than the cylindrical hole configuration. Kusterer et al. [46] numerically studied the conjugate heat transfer of a film-cooled blade with internal flow passages and cooling hole rows. The deficiencies of the blade cooling configuration close to the leading edge and blade tip have been found and improved based on conjugate heat transfer calculations. Ramachandran and Shih

[47] studied Biot number analogy for design of conjugate heat transfer experiments. They performed conjugate heat transfer numerical simulations of a plate with thermal barrier coating using SST turbulence model. The coolant side is enhanced by inclined ribs or pin fins. They found that Biot number is the most important dimensionless parameter. For their designs, the nondimensional temperature and heat flux distributions will be nearly the same if the Biot number distributions on the hot gas side and the coolant side are nearly matched.

Albert et al. [48] carried out a one-dimensional conjugate heat transfer analysis, which showed the importance of matching Biot number *Bi* and h_f/h_i to the engine conditions in conjugate heat transfer experiments. Here, h_f/h_i is the ratio between the external heat transfer coefficient and the internal heat transfer coefficient. They measured surface temperature and obtained overall effectiveness of a blade leading edge with three rows of shaped holes. Maikell et al. [49] experimentally studied blade leading edge conjugate heat transfer with three rows of cylindrical film cooling holes and the thermal barrier coating using IR camera technique. One row is located in the stagnation line, and other two rows are located at ±25 degrees measured from the stagnation line. They estimated *Bi* = 1.8 in their experiments, which is similar to the engine condition (about 1.0 to 2.1). The density ratio DR = 1.5, and the blowing ratio M = 1.0 and 2.0. Dyson et al. [50] studied overall effectiveness for the leading edge with varying hole pitch. Dobrowolski et al. [51] numerically simulated adiabatic effectiveness and overall effectiveness of the leading edge model using RKE turbulence model. Overall effectiveness predicted by simulations is higher than the experiments in the stagnation region and lower than the experiments in the downstream region. Ravelli et al. [52] numerically studied the effects of internal impingement cooling on the blade leading edge using RKE turbulence model. Three impingement plate designs were considered. Two designs have one row of impinging holes in the stagnation line

with varying hole diameters. The third designs have two rows of impinging holes along the ±25 degrees lines. Results showed that the overall effectiveness of the leading edge model was slightly increased by impinging cooling. Montomoli et al. [53] experimentally and numerically studied the benefit of high conductivity materials in film cooled leading edge with jet impingement, using liquid crystal method and in-house CFD solver. Polycarbonate (K = 0.2 W/mK) and stainless steel (K = W/mK) were selected. Results show that high conductivity materials can greatly reduce thermal gradient. Chandran and Prasad [54] studied conjugate heat transfer of leading edge of a turbine nozzle guide vane with impingement and showerhead film cooling. They used IR camera technique and k-w SST model to obtain the overall effectiveness. Two materials with thermal conductivity K = 0.2 W/mK and 14.9W/mK were studied. It was found that the blowing ratio effect on the overall effectiveness is greatly dependent on the material conductivity.

RKE model is used by many researchers which provides a good agreement with experiments in predicting leading edge heat transfer. Wang et al. [41] studied leading edge internal heat transfer with normal jet and tangential jet. Chowdhury et al. [17], and Zhang et al. [55] studied leading edge adiabatic effectiveness. York and Leylek [56-57] studied leading edge external heat transfer and adiabatic effectiveness

1.4 Objective of the Study

For the study of influence of leading edge profile on film cooling effectiveness with shaped holes, two semi-elliptical models are used in addition to the semi-cylindrical model. All three leading edge models are equipped with three rows of shaped cooling holes near the stagnation region. Typical ranges of blowing ratio (M = 0.5, 1.0, and 1.5) and density ratio (DR = 1.0, 1.5, and 2.0) are investigated. The PSP measurement technique is used to obtain the detailed film cooling effectiveness distributions on three leading edge profiles. In addition, the RKE model is used to simulate/predict the cooling flow distribution and film cooling effectiveness. Detailed film cooling effectiveness distributions (contours), span-wise averaged effectiveness, and area-averaged effectiveness will be presented, discussed, and compared.

In the open literature, most studies investigated leading edge impingement heat transfer without mainstream flow. As the mainstream flow can generate pressure gradient around the leading edge outside surface, resulting in different coolant flow rates from different film cooling rows and different flow distribution inside the leading edge cavity. In the present study, we considered the effect of mainstream flow on the leading edge internal heat transfer with jet impingement and film cooling. We use a semi-cylinder with three rows of film cooling holes to simulate the leading edge surface. In addition, the effects of jet holes position are considered for the normal jet and the tangential jet. The transient liquid crystal method is applied to measure the internal heat transfer and the RANS realizable k-ε (RKE) turbulence model are used to better understand the flow distribution and heat transfer behavior inside the leading edge cavity. RKE model is used by many researchers which provides a good agreement with experiments in predicting leading edge heat transfer. Jet Reynolds number Re ranges from 5000, 10000 to 15000, and the corresponding averaged blowing ratio is about 0.77, 1.54 and 2.31, respectively. We use

air as the coolant, and the density ratio between the coolant and the mainstream is about 1.0. Detailed flow distributions, Nu contours, span-wise averaged Nu, stream-wise averaged Nu, and area averaged Nu will be presented, discussed, and compared.

In the open literature, there are limited experimental data of turbine blade conjugate heat transfer. In this study, we investigates conjugate heat transfer of a half cylinder leading edge model with three rows of cylindrical film cooling holes. The experimental data of the whole blade leading edge is obtained. The PSP measurement technique is used to obtain the adiabatic effectiveness. The liquid crystal method is applied to measure the overall effectiveness. In addition, CFD simulations are applied to calculate the external/internal heat transfer, adiabatic effectiveness and overall effectiveness, using the realizable k-ε (RKE) turbulence model. For the present study, Biot number based on averaged external heat transfer coefficient obtained by the CFD is about 1.3 to 1.7, and $h_f/h_i$is about 2.2 to 1.0 for three jet Reynolds number. The influence of impinging jet holes position on conjugate heat transfer performance is considered for the normal jet and the tangential jet. Detailed effectiveness contours, span-wise, stream-wise, and area averaged effectiveness will be presented, discussed, and compared.

2. INFLUENCE OF TURBINE BLADE LEADING EDGE PROFILE ON FILM COOLING WITH SHAPED HOLES

2.1 Experimental Setup and Method

The experimental facility is a suction type low-speed wind tunnel. The wind tunnel width is 76.2 cm, and the distance between the turbulence grid and outlet to the suction blower is 185 cm. The mainstream velocity is about 20.89 m/s and mainstream Reynolds number is about 100,000 based on the cylinder's diameter. The turbulence intensity is 7% and turbulence integral length scale is about 1.5 cm measured near the cylinder. The hot-wire was used to measure the mainstream turbulence intensity. The distance between the measurement point and the stagnation point is about 15.24 cm. The stagnation line of the leading edge is at 70 cm downstream of the turbulence grid. Figure 1 schematically shows the test facilities and test section. Coolant comes into the leading edge from the bottom. Through an inside plenum, it impinges on the leading edge internal surface from a row of impingement holes. Figure 2(a) shows the top view of leading edge profiles, impingement plates and internal plenums; Front view of leading edge profiles and PSP painted areas are shown in Figure 2(b); Figure 2(c) shows the shaped hole geometry. Table 1 shows the dimensions of film cooling holes and leading edge.

There are three leading edge profiles, one semi-cylinder (1.0R) and two semi-ellipses (1.5R and 2.0R). The ratios of major to minor axis of two semi-elliptical cylinders are 1.5 and 2.0, respectively. There are 15 holes in each row with a hole-to-hole spacing $p = 4d$ in the span-wise direction, hole diameter d = 0.32cm. The impingement plate also has 15 holes with a diameter of 0.62cm. Impingement holes and leading edge cooling holes are staggered in the span-wise direction. During the experiment, only the middle seven cooling holes per row and the middle

seven impingement holes are opened. PSP was painted on the middle five holes per row on one side of the leading edge, as shown in Figure 2(b). For 1.0R model, it has an outer diameter of 7.62cm, a height of 25.4cm, and a thickness of 0.64cm. The impingement plate is behind the semi-cylinder. There are three rows of shaped cooling holes, located at 0 degrees (the stagnation row) and ± 30 degrees (the second row). For 1.5*R* and 2.0*R* models, height, thickness, and the distance between impingement plate and stagnation line are the same as 1.0*R* model. Row spacing (arc length) between two rows of shaped cooling holes (*S1* = 1.995 cm) is also the same. The cooling hole angle to surface (α) is 25 degrees. The lateral expansion angle (γ) is 5 degrees. The forward expansion angle (δ) is 5 degrees. Table 1 shows detailed dimensions of cooling holes and leading edge models.

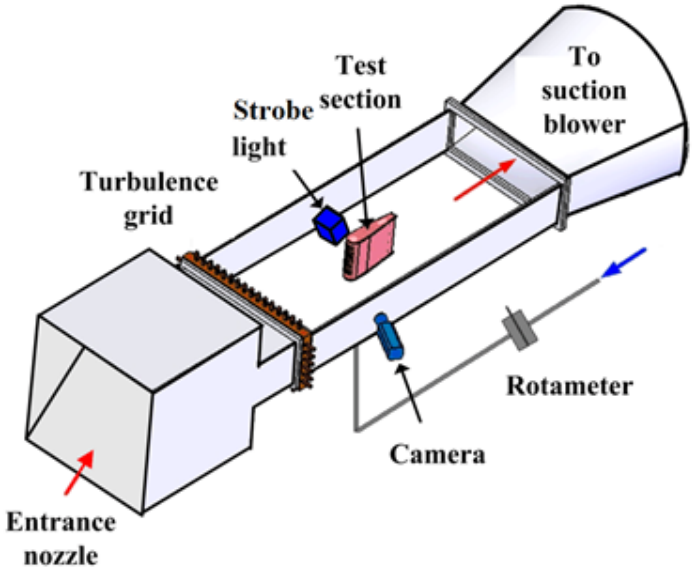

(a) Test facility

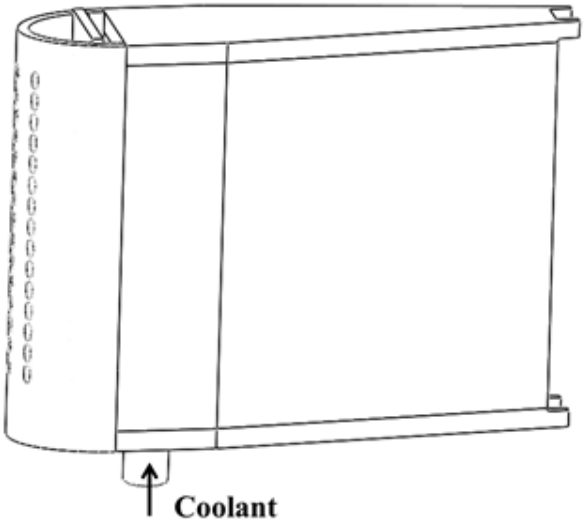

(b) Test section

Figure 1 Schematic diagram of the test facility and test section.

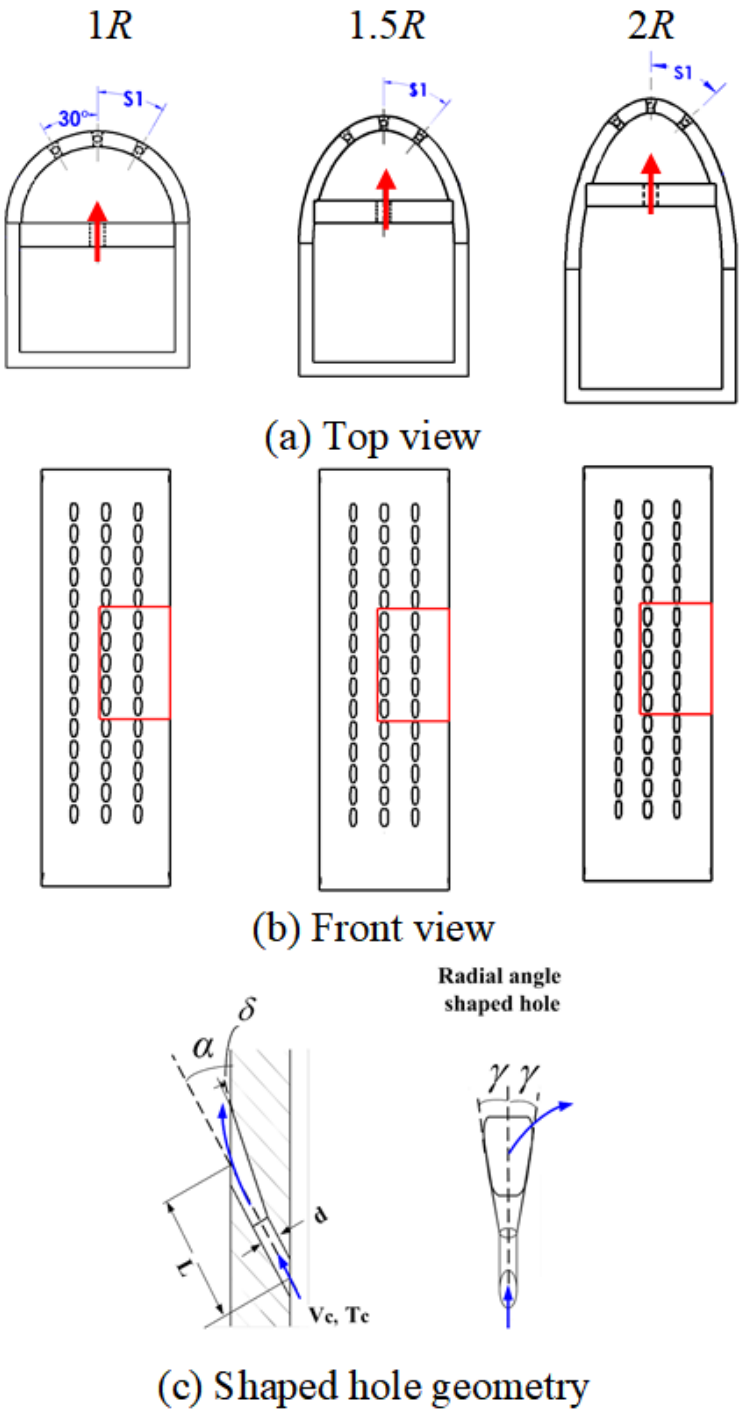

Figure 2 Leading edge models and shaped holes configuration.

Table 1 Dimensions of cooling holes and leading edge models.

Hole diameter (d, cm)	0.32
Leading edge to hole diameter ratio (D/d)	24
Hole to hole spacing (p/d)	4
Ratio of hole length to diameter (L/d)	4.73
Lateral expansion angle (γ) (degree)	5
Forward expansion angle (δ) (degree)	5
Angle to surface (α) (degree)	25
Ratio of hole breakout area to metering cross-section area	1.9
Impingement hole diameter (cm)	0.62
Impingement plate thickness (cm)	0.95
Row spacing between shaped cooling holes *S1* (cm)	1.995
Distance between impingement plate and stagnation line on leading edge inner surface (cm)	3.17

PSP is made of luminescent molecules embedded in an oxygen-permeable polymer binder. Upon excitation by a light source, the luminescent molecules then emit fluorescent light when it relaxes from the excited state to the ground state. The emitted light intensity is inversely proportional to the partial pressure of oxygen on the painted surface. The paint used in this study was UniFIB UF470-750 from ISSI Inc. As shown in Figure 1(a), a strobe light (470 nm) was used to excite the luminescent molecules in the paint, which then emits fluorescent light with wavelength larger than 600 nm. A Cooke Sensicam CCD camera with a long pass filter was used to capture the emission intensity of the paint.

Figure 3 shows schematics of leading edge film cooling with adiabatic wall boundary condition. T_c is the coolant temperature. Coolant with temperature T_c comes out from the film cooling hole and mixed with the mainstream. Taw is the adiabatic wall temperature, $T\infty$ is the mainstream temperature, T_{film} is the film temperature. Here we assume $T_{aw} = T_{film}$ is the driven temperature. Then we can obtain Taw and the driven temperature T_{film} by measure the wall temperature under adiabatic wall boundary condition.

Calibration was performed to obtain the relationship between the PSP emission intensity and the oxygen partial pressure, as presented in Figure 4(a). Figure 4(b) shows the calibration data points under different viewing angles to the surface by Shiau et al. [58] using the same calibration facilities. The angles range from 20° to 90°. The result indicates that there is no viewing angle effect on PSP measurements. As a result, PSP is an ideal tool for film cooling effectiveness measurements on curved surfaces. Nitrogen and CO_2 are selected to obtain the coolant to mainstream density ratio 1.0 and 1.5. A mixture of 15% SF_6 and 85% Ar is used for the density ratio 2.0.

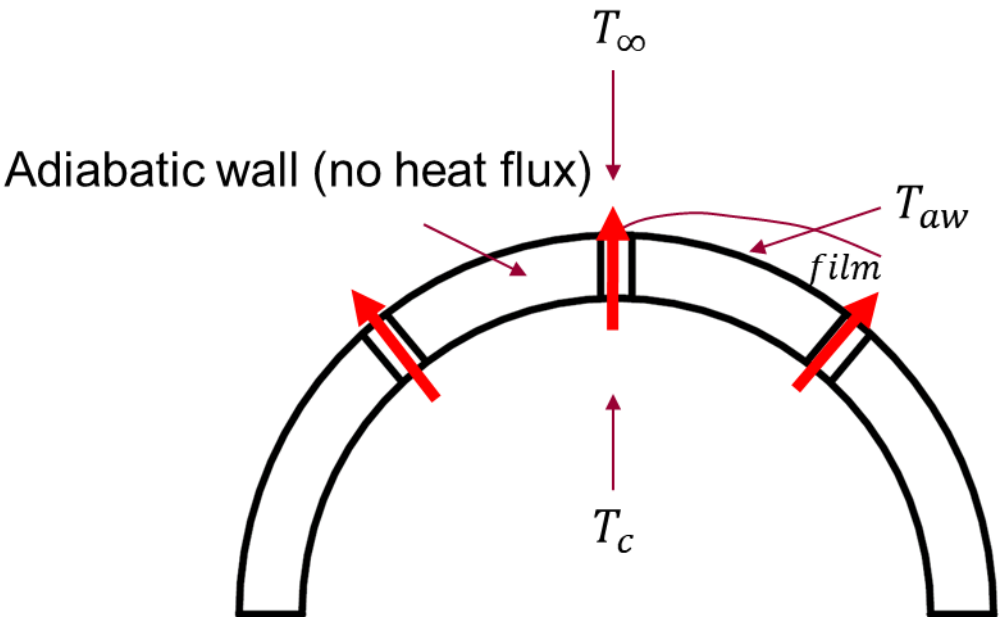

Figure 3 Schematic of leading edge film cooling with adiabatic wall.

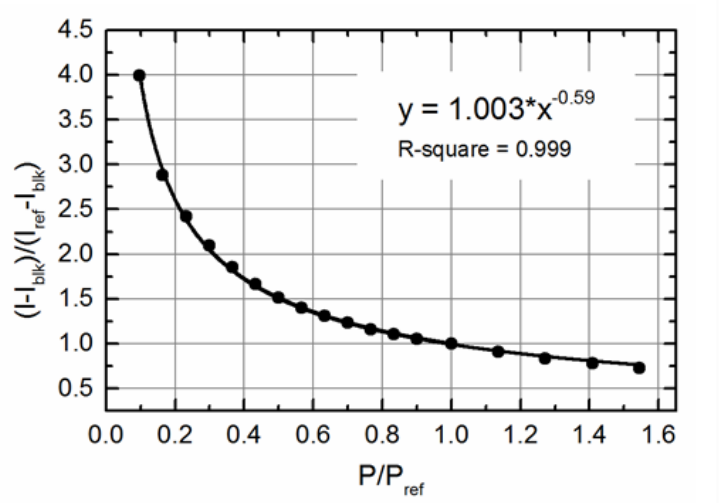

(a)

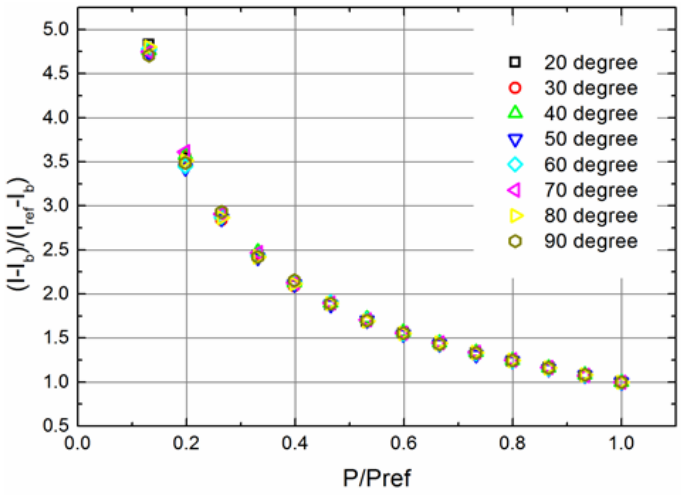

(b)

Figure 4 PSP calibration curves.

Four tests are needed to measure the film cooling effectiveness: the black background test, the reference test, the air injection test and the foreign gas injection test. For each test, 200 images were recorded and averaged to reduce the noise. The background noise intensity (I_{blk}) was acquired under dark condition. The reference image intensity (I_{ref}) was acquired with strobe light illumination. Both I_{blk} and I_{ref} were recorded with no flow condition. The air image intensity (I_{air}) was recorded with the mainstream flow on and air as the coolant. The foreign gas image intensity (I_{fg}) was recorded with the mainstream flow on and foreign gas (N_2, CO_2, or the mixture) as the coolant.

The relationship between PSP emitting light intensity and oxygen partial pressure can be expressed as follows:

$$\frac{I - I_{blk}}{I_{ref} - I_{blk}} = f\left(\frac{P_{O_2}}{\left(P_{O_2}\right)_{ref}}\right) \tag{2.1}$$

Based on mass transfer analogy, the film cooling effectiveness can be calculated as:

$$\eta = \frac{T_\infty - T_{aw}}{T_\infty - T_c} \approx \frac{C_{O_2,fg} - C_{O_2,air}}{C_{O_2,c} - C_{O_2,air}} = 1 - \frac{C_{O_2,fg}}{C_{O_2,air}} = 1 - \frac{1}{\left[1 + \left(\frac{P_{O_2,air}/P_{O_2,ref}}{P_{O_2,fg}/P_{O_2,ref}} - 1\right)\frac{W_{fg}}{W_{air}}\right]} \tag{2.2}$$

, where $C_{O2,c}$ is the oxygen concentration inside film cooling holes, $C_{O2,air}$ and $P_{O2,air}$ are the oxygen concentration and partial pressure with air injection, $C_{O2,fg}$ and $P_{O2,fg}$ are the oxygen concentration and partial pressure with foreign gas injection, W_{air} is the molecular weight of air, and W_{fg} is the

molecular weight of the foreign gas. The applicability of the heat-mass analogy is based on the assumption that the turbulent Lewis number is close to unity. Flow over the leading edge model becomes turbulent boundary layer flow due to the interaction/mixing between highly disturbed mainstream and film cooling jet from the stagnation row. So, we think the heat-mass analogy is applicable in this study.

2.2 Numerical Setup and Method

Computational simulations in this study were done using ANSYS FLUENT 17.1. Grids including unstructured meshes and structured meshes were generated using ICEM CFD. Unstructured meshes are generated near the leading edge, and structured meshes are generated away from the leading edge to simulate the wind tunnel environment. The total computational domain is 185 cm × 38.1 cm × 1.28 cm. Mesh interface is used between the two types of meshes. There are 20 prism layers in the walls of leading edge and cooling holes, with $y+$ value less than 1. The total number of grids was about 4 million (3.5 million unstructured meshes and 0.5 million structured meshes). To test the grid independence, mesh near the leading edge surface is refined (about 5 million unstructured meshes and 1 million structured meshes). The difference in effectiveness between the two meshes is less than 1%. Periodic and symmetric boundary conditions were used to save computational time.

Figure 5 shows schematic of the computational domain with unstructured mesh for 1.0R profile. The realizable k-ε (RKE) model and the SIMPLE method are used. The fluid is incompressible ideal gas, and fluid properties were temperature dependent. Table 2 shows boundary conditions of the CFD model. Note that density ratio between the coolant and the mainstream is obtained by varying the coolant air temperature. Nitrogen (DR = 0.97) is used as the

coolant for *DR* = 1.0 cases in experiments and the density ratio is also set to 0.97 for *DR* = 1.0 cases in CFD simulations.

Simulations were assumed converged when the residuals were in order 10^{-8} for energy, in order 10^{-5} for the continuity equation, and in order 10^{-6} for all other residuals, and the span-wise averaged effectiveness was not changed after additional 1000 iterations.

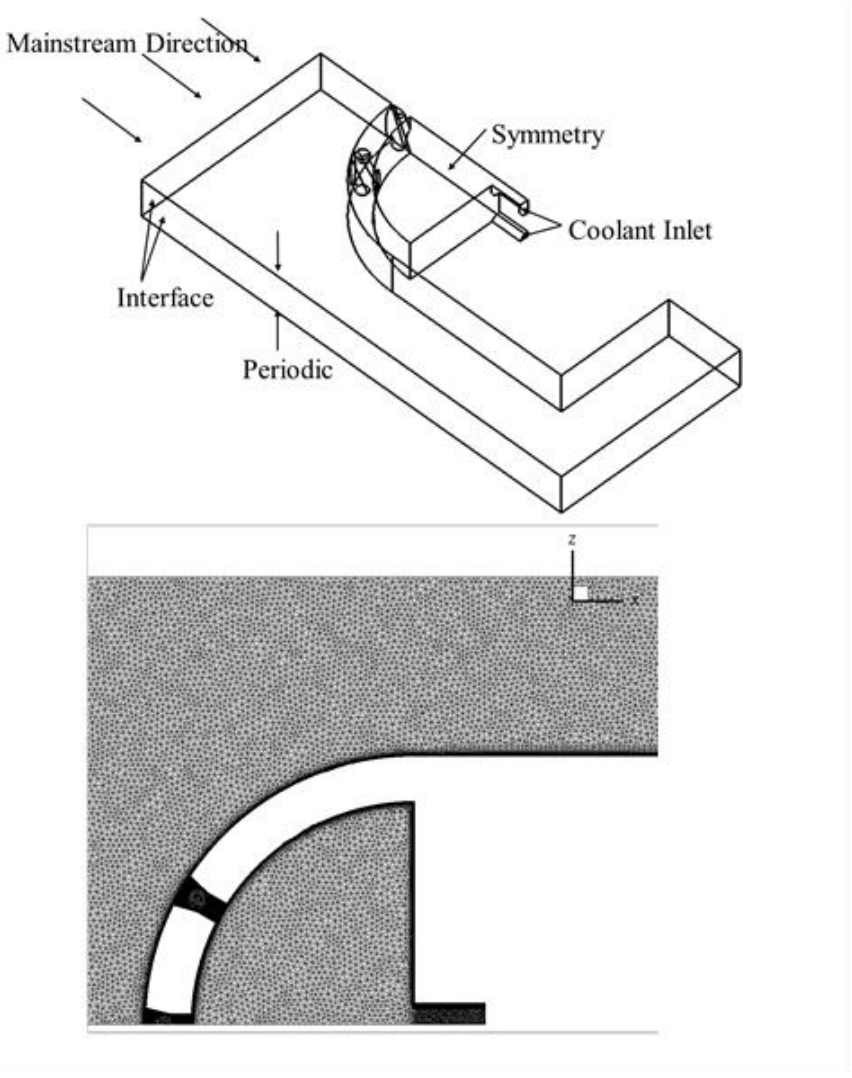

Figure 5 Schematic of computational domain and grid.

Table 2 Boundary conditions for the CFD model.

Inlet mainstream velocity (m/s)	20.89
Inlet mainstream temperature (K)	296
Inlet mainstream turbulence intensity	7%
Coolant temperature (K)	148, 197.3, 306.2
Coolant turbulence intensity	5%
Coolant turbulent integral length scale (mm)	6.2

2.3 Experimental Results and Discussion

For the experimental study, three density ratios (1.0, 1.5 and 2.0) and three blowing ratios (0.5, 1.0 and 1.5) were investigated for the three leading edge models (1.0*R*, 1.5*R*, and 2.0*R*). It should be noted that the blowing ratio is based on the mainstream velocity (20.89 m/s) and the corresponding density and velocity values.

Experimental data are shown by effectiveness contour plots, span-wise averaged effectiveness plots, and area averaged effectiveness plots. Averaged effectiveness plots include the film-hole area where the effectiveness is very high (0.9-1.0). Blowing ratio effect, density ratio effect, and leading edge profile effect are investigated.

2.3.1 Film cooling effectiveness contours

Detailed film cooling effectiveness distributions of semi-cylinder profile (1.0*R*) are presented in Figure 6 for *DR* = 1.0 and 2.0, and *M* = 0.5, 1.0 and 1.5. The horizontal axis is *s/d* (mainstream direction) and the vertical axis is *z/d* (span-wise direction). The stagnation row is at *s/d* = 0. At low blowing ratio *M* = 0.5, as the mainstream static pressure is high, there is no coolant coming out of the stagnation row. In the downstream row region (*s/d* > 7), as the mainstream

momentum increases, the coolant is deflected by the mainstream and the film traces become longer. When the density ratio increases from 1.0 to 2.0, the film cooling effectiveness traces become wider and cover more region in the span-wise direction.

As shown in Figure 6, for a fixed density ratio, film effectiveness increases with increasing blowing ratio. At low blowing ratio (M = 0.5), the effectiveness of DR = 2.0 is lower than DR = 1.0. This is because the coolant with insufficient momentum is difficult to eject from shaped holes, especially for high density coolant (DR = 2.0) with low momentum. As there is nearly no coolant coming out from the stagnation row, it is inappropriate to use low blowing ratio in these shaped hole designs. At high blowing ratios (M = 1.0 and 1.5), the effectiveness of DR = 2.0 is higher than DR = 1.0. The reason is that, for a given blowing ratio, the coolant momentum decreases when density increases, so the jet has a higher tendency to adhere to the surface.

Figure 7 shows the film cooling effectiveness distributions of DR = 1.5, at M = 0.5, 1.0 and 1.5, respectively for three leading edge profiles. For lower blowing ratio M = 0.5, there is almost no coolant coming out from stagnation row region ($0 < s/d < 5$); film effectiveness level is low and about the same in the downstream row region ($s/d > 7$) for all three leading edge profiles. For high blowing ratios M = 1.0 and 1.5, film effectiveness for 1.0R and 1.5R are higher than 2.0R. Overall, 1.0R and 1.5R show the higher film cooling effectiveness, 2.0R shows the lower effectiveness.

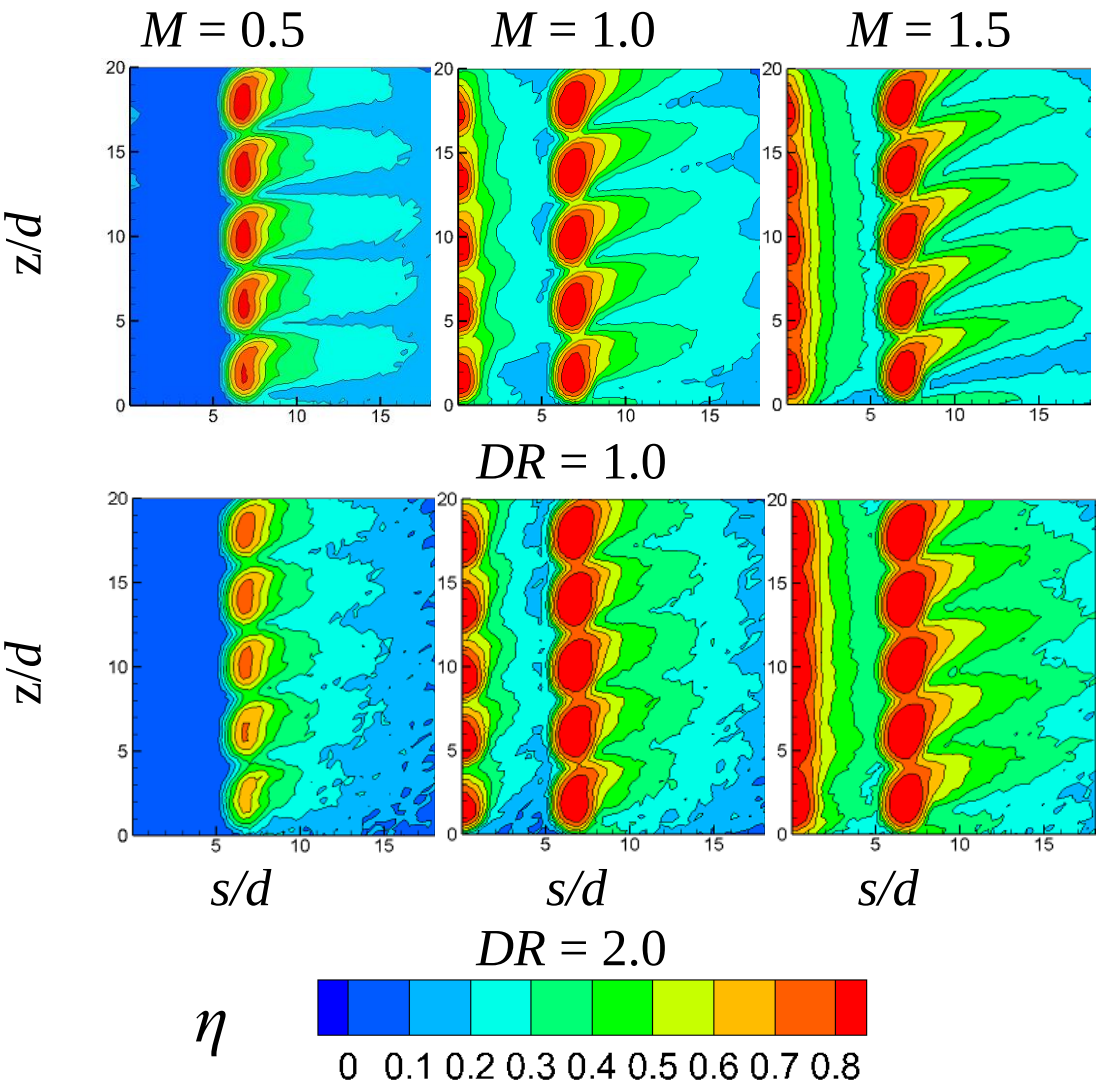

Figure 6 Film cooling effectiveness contour plot for 1.0*R*.

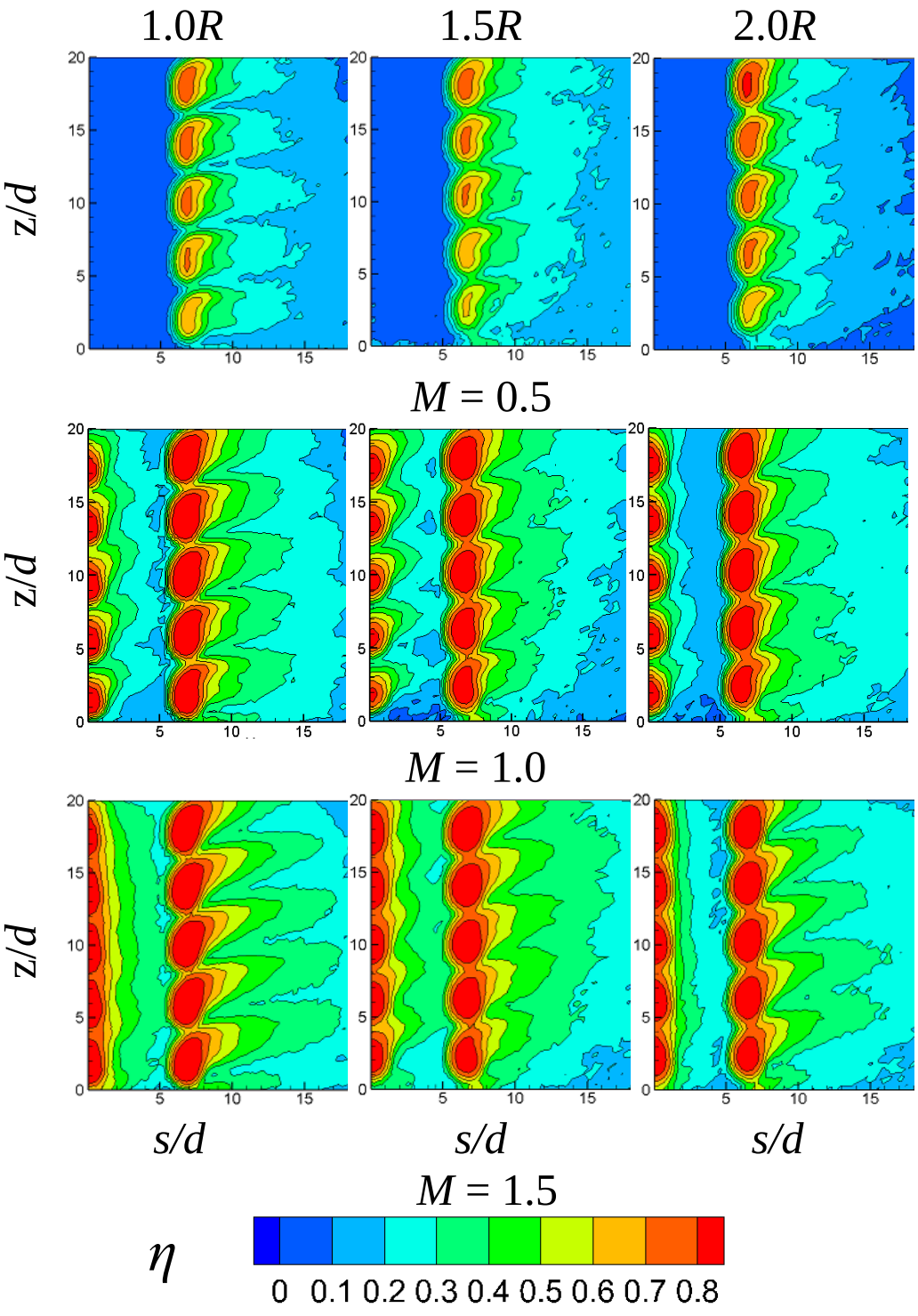

Figure 7 Film cooling effectiveness contour plot at *DR* = 1.5.

2.3.2 Span-wise averaged film cooling effectiveness

Figure 8 shows the blowing ratio effect on the span-wise averaged film effectiveness. It is found that, for a fixed profile (1.0*R*, 1.5*R*, or 2.0*R*) and density ratio (*DR*=1.0 or 2.0), higher blowing ratio gives higher effectiveness. For M = 0.5, film effectiveness is very low in the stagnation row region ($0 < s/d < 5$). Film effectiveness increases significantly for high density coolant (DR = 2.0) than low density coolant (DR = 1.0) when the blowing ratio increases from 1.0 to 1.5. It may be caused by very high coolant momentum at DR = 1.0 which lead to stronger mixing with the mainstream. In the downstream portion ($7 < s/d < 20$), blowing ratio showed significant effect at DR = 2.0 than DR = 1.0 for all three profiles. At DR = 1.0, blowing ratio has relatively small effect for the 1.5 R and 2.0*R* profile.

Figure 9 shows the density ratio effect on the span-wise averaged film effectiveness. The results show that, at high blowing ratio (M = 1.5), film cooling effectiveness increases with increasing density ratio for all three leading edge profiles. At low blowing ratio (M = 0.5), in general, there is small effect in the density ratio.

Figure 10 shows the leading edge profile effect on the span-wise averaged film effectiveness. Overall, for DR = 1.0, 1.0*R* is a little better than 1.5*R*, and 2.0*R* is the worst; for DR = 1.5, 1.0*R* and 1.5*R* are almost the same, and 2.0*R* is the worst; for DR = 2.0, 1.5*R* is the best, 1.0*R* and 2.0*R* are almost the same.

It is observed that, for DR = 1.0 and 1.5 at M = 1.5, the effectiveness is almost the same at the stagnation line (s/d = 0) for three profiles, however, the effectiveness of 2.0*R* is much lower in the region ($2 < s/d < 5$). This is due to relatively high curvature in this region for 2.0*R*, so the coolant may have more tendency to lift off, resulting in low effectiveness. As the density ratio

increases to *DR* = 2.0, effectiveness for 2.0*R* improves significantly. It may be explained by the fact that the high density coolant has more tendency to adhere to the surface.

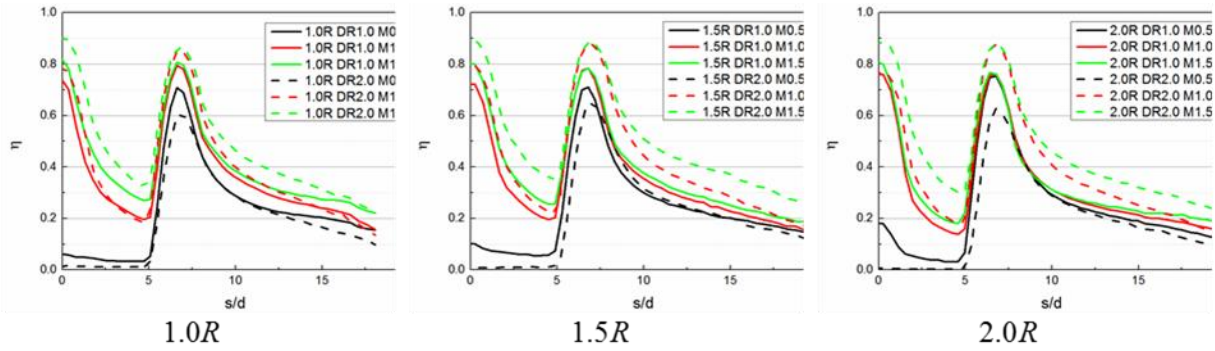

Figure 8 Effect of blowing ratio on span-wise averaged film cooling effectiveness.

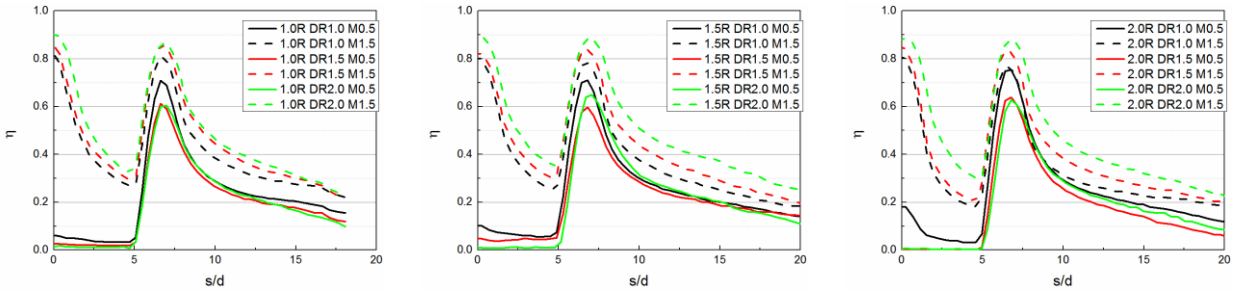

1.0*R* 1.5*R* 2.0*R*

Figure 9 Effect of density ratio on span-wise averaged film cooling effectiveness.

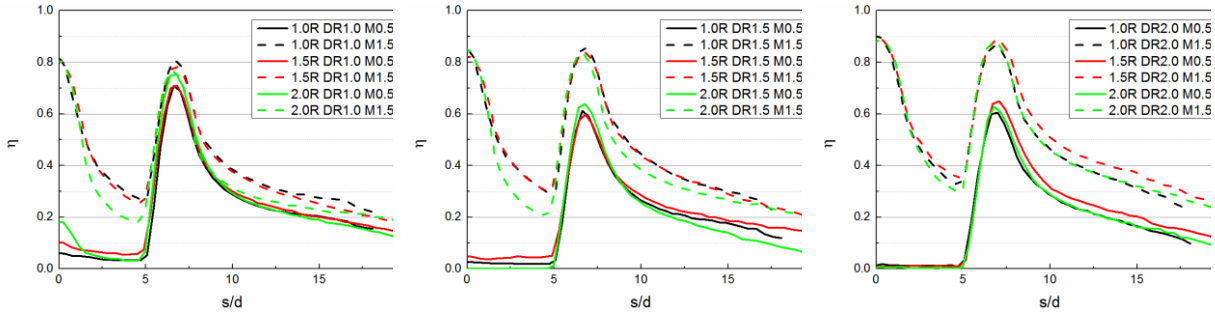

DR = 1.0 *DR* = 1.5 *DR* = 2.0

Figure 10 Effect of leading edge profile on span-wise averaged film cooling effectiveness.

2.3.3 Area averaged film cooling effectiveness

As shown in Figure 11, area averaged film effectiveness for total 27 cases is calculated with 0 < s/d < 18 and 0 < z/d < 20 for three leading edge profiles. The best case is 1.5R at DR = 2.0 and M = 1.5. At M = 1.0 and 1.5, effectiveness values clearly increase with increasing density ratio. M = 0.5 is not effective for leading edge film cooling with shaped holes. At DR = 1.0 and 1.5, effectiveness value decreases from 1.0R to 1.5R and 2.0R, for M = 1.0 or 1.5. However, at the highest density ratio DR = 2, 1.5R outperformed 1.0R and 2.0R at all three blowing ratios.

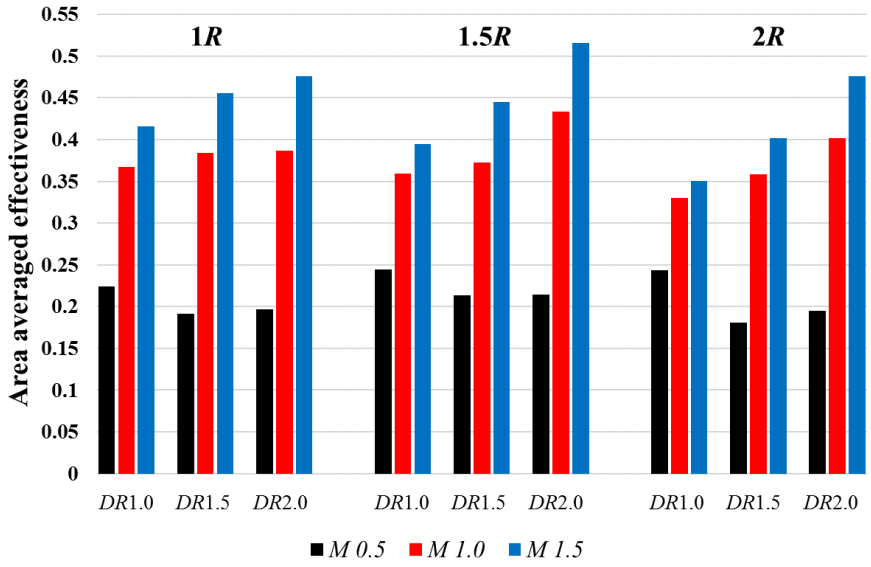

Figure 11 Area averaged film cooling effectiveness.

2.4 Numerical Results and Discussion

In this section, computational simulations for three leading edge profiles at DR = 1.5, and M = 1.0 and 1.5 are discussed first. Results are shown by static pressure distribution plots, velocity magnitude contour plots, coolant path lines plots, and span-wise averaged effectiveness plots. Mass flow rates and local blowing ratios are calculated. Then, we focus on 1.0R profile at DR = 1.0, 1.5, 2.0 and M = 1.0 and 1.5. Effectiveness contour plots and span-wise averaged effectiveness plots are presented.

Figure 12 shows leading edge span-wise averaged static pressure distributions for three profiles at DR = 1.5 and M = 1.0. The static pressure here is the gauge pressure. It is observed that, for all three leading edge profiles, the static pressure decreases between the stagnation row and the second row, and then increases and decreases after the second row. Before the second row, the static pressure for 1.0R is higher than 1.5R and 2.0R respectively. After the second row, the static pressure for 1.0R is lower than 1.5R and 2.0R respectively.

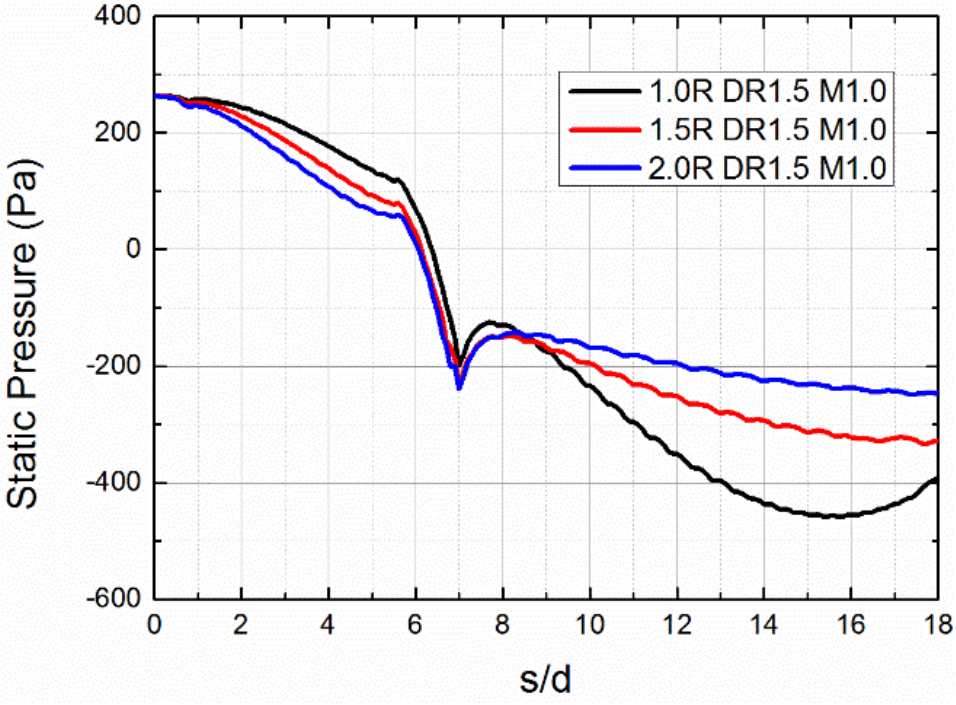

Figure 12 Leading edge span-wise averaged static pressure distributions.

Static pressure contours and velocity magnitude contours in the middle plane for three profiles at DR = 1.5 and M = 1.0 are shown in Figure 13 and Figure 14. The static pressure in the plenum is about the same, with the highest static pressure at the stagnation point in the plenum. The outside surface static pressure decreases and the local mainstream velocity increases from the stagnation region to the downstream. As shown in Figure 14, the coolant impinges on the leading edge inside surface and generates the vortex in the cavity. Before the second row, the local mainstream velocity for 1.0R is lower than 1.5R and 2.0R. After the second row, the local mainstream velocity for 1.0R is higher than 1.5R and 2.0R.

Figure 15 presents coolant path lines for three profiles at DR = 1.5 and M = 1.0 colored by dimensionless temperature $\theta = (T\infty-T) / (T\infty-Tc)$.

In the plenum, the coolant temperature is the same as the inlet. The coolant is mixed with the mainstream and the coolant temperature increases just after it ejects from the cooling holes. Before the second row, the dimensionless temperature path lines show some different for three leading edge profiles. However, in the downstream, the dimensionless temperature path lines are about the same for three leading edge profiles.

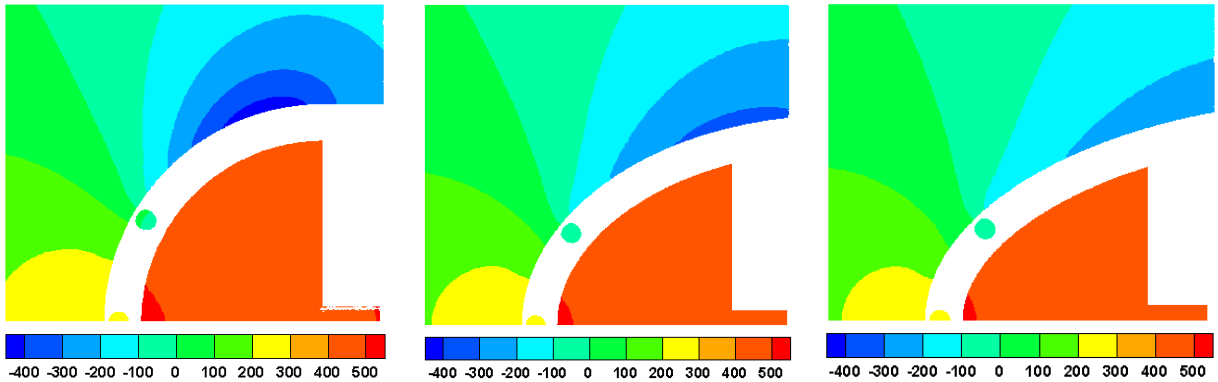

Figure 13 Static pressure contours.

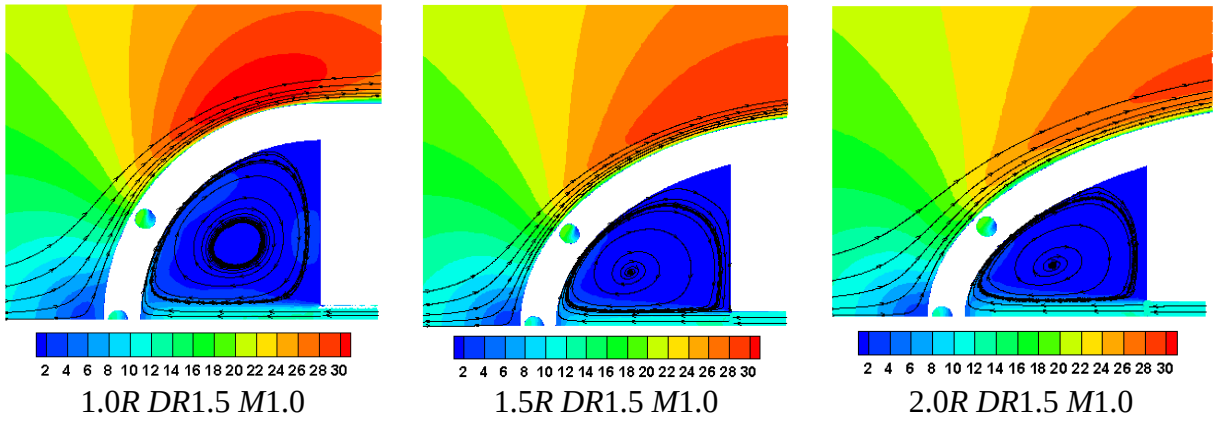

Figure 14 Velocity magnitude contours and streamlines.

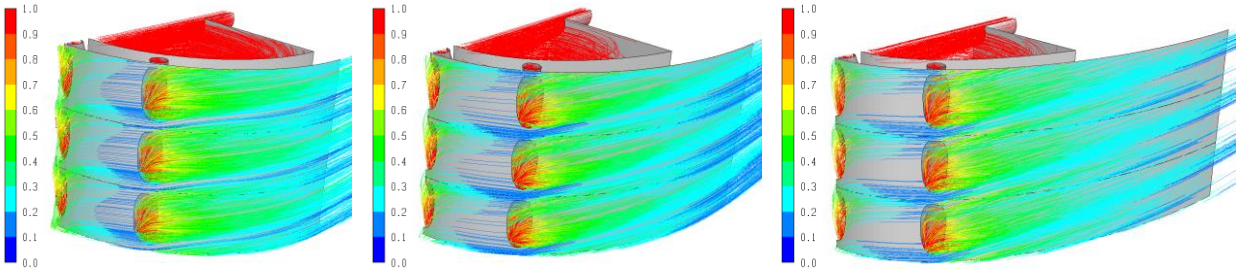

Figure 15 Coolant path lines and dimensionless temperature.

Figure 16 and Figure 17 show mass flow rates (10^{-4} kg/s) for DR = 1.5 (from one cooling hole) and local blowing ratios for different cases. Here, local blowing ratios are calculated based on mass flow rates and the hole diameter. The mainstream velocity and the local mainstream velocity near the second row are used in calculating the local blowing ratios of the stagnation row and the second row, respectively. Compared with holes in the second row, there is less coolant ejecting from holes in the stagnation row. In addition, for the same blowing ratio M, in the stagnation row, the coolant mass flow rate decreases a little when the profile changes from 1.0R to 1.5R and 2.0R.

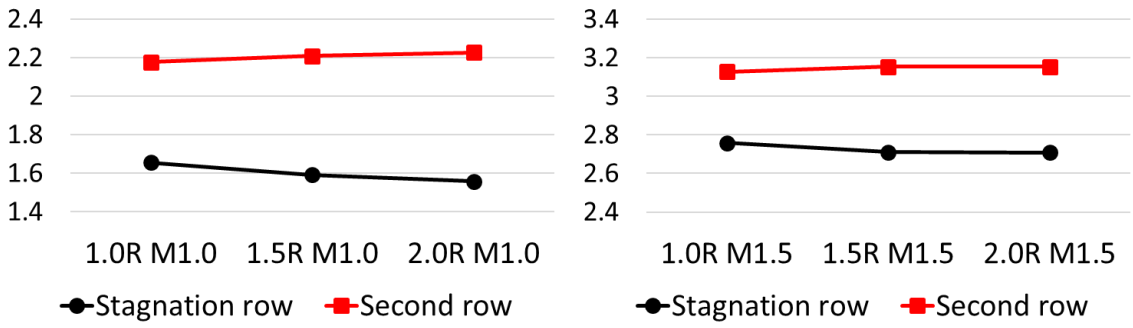

Figure 16 Mass flow rates for *DR* = 1.5.

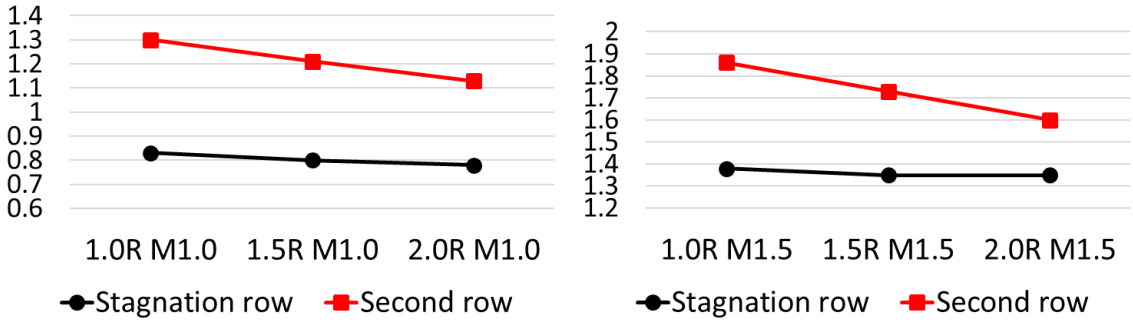

Figure 17 Local blowing ratios for *DR* = 1.5.

The reason is that the outside static pressure near the stagnation row is about the same for three profiles; the outside static pressure near the second row is lower than the stagnation row, and decreases from 1.0R to 1.5R and 2.0R. So more coolant comes out from the stagnation row for 1.0R than that for 1.5R and 2.0R. It should be noted that although the mass flow rate of the second row for 1.0R is lower than 1.5R and 2.0R, the calculated local blowing ratio of the second row for 1.0R is higher than 1.5R and 2.0R, because of local mainstream velocity near the second row increases from 1.0R to 1.5R and 2.0R.

Figure 18 shows comparisons of CFD and PSP in terms of span-wise averaged film cooling effectiveness for three profiles at DR = 1.5. In the stagnation region ($0 < s/d < 5$), CFD is in good agreement with experiments for 1.0R and 1.5R. For 2.0R, it seems that CFD under predicts the coolant lift off due to high curvature at $2 < s/d < 5$. In the downstream region, CFD under predicts the effectiveness just after the second row ($7 < s/d < 8$), and over predicts the effectiveness at $s/d > 8$. This may be due to CFD under predicts the coolant jet lateral spreading at $s/d > 8$. As shown in Figure 19, the predicted effectiveness for 1.0R is a little higher than 2.0R in the stagnation region ($0 < s/d < 5$), which is consistent with experiments.

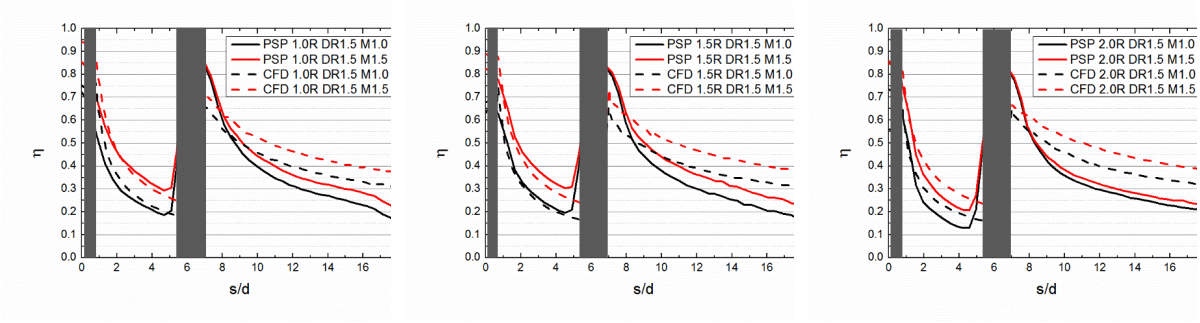

1.0*R DR*1.5 1.5*R DR*1.5 2.0*R DR*1.5

Figure 18 CFD predicted and PSP measured span-wise averaged film cooling effectiveness.

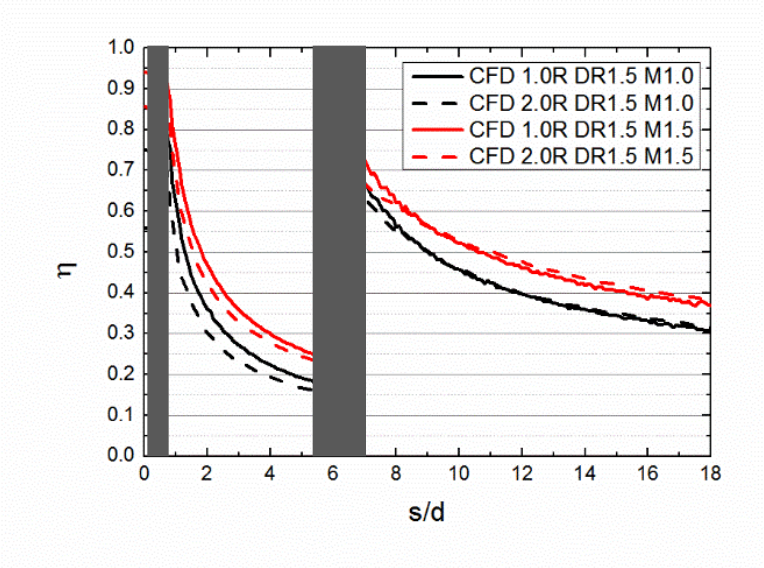

Figure 19 CFD predicted span-wise averaged effectiveness for 1.0R and 2.0R profiles.

Then we focus on 1.0R leading edge profile. Figure 20 and Figure 21 present mass flow rates (10^{-4} kg/s) (from one cooling hole) and local blowing ratios for different cases. It is observed that, for the same blowing ratio M, increasing coolant density decreases mass flow rate from the stagnation row, which can be explained by the pressure difference, as showing in Table 3.

The coolant mass flow rate from different rows can be expressed as follows:

$$MFR_i = C_D \rho_c A_i \sqrt{(2(P_T - P_i)/\rho_c)}, i = 1, 2. \qquad (2.3)$$

, where MFR_1 and MFR_2 are the mass flow rates of the stagnation row and the second row respectively. C_D is the discharge coefficient, Ai is the area of cooling holes, P_T is the total pressure in the plenum, and Pi is the outside surface static pressure near cooling holes. The pressure difference between P_T and P_i is the driven force to let the coolant eject from cooling holes. Assume P_T and C_D of the two rows are about the same, then the mass flow rate ratio between the stagnation row and the second row can be calculated by

$$MFR_1/MFR_2 = \sqrt{(P_T - P_1)} / \sqrt{(P_T - P_2)} \qquad (2.4)$$

When $P_T > P_1 > P_2$, the partial derivative of the mass flow rate ratio with respect to P_T is positive, so the ratio will decrease if P_T decreases.

Table 3 shows the averaged total pressure in the plenum and the mass flow rate ratio for 1.0R profile. Generally, higher P_T gives higher MFR1/MFR2 for all six cases. For a fixed blowing ratio M, when DR increases, P_T decreases and P_i are about the same, so the ratio decreases.

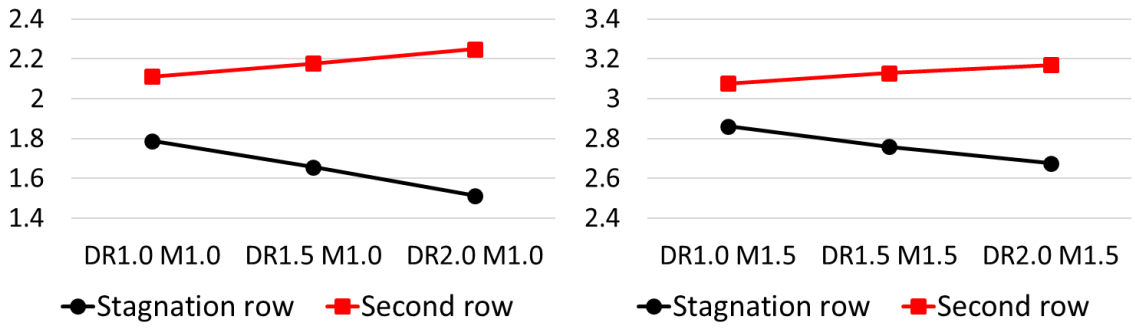

Figure 20 Mass flow rates for 1.0R profile.

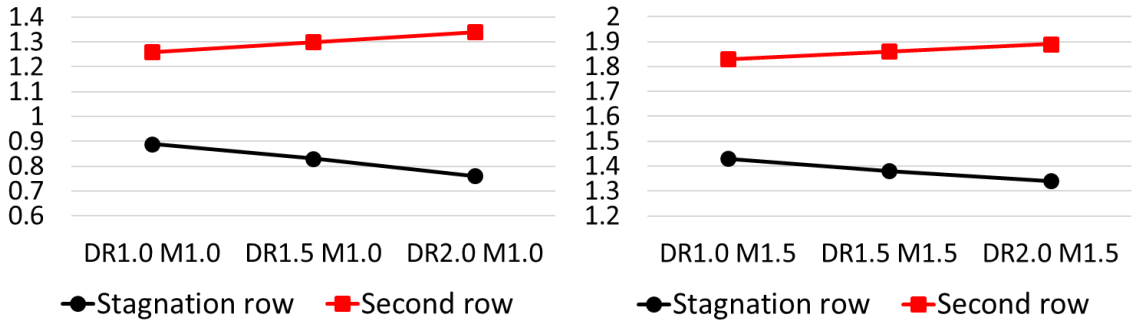

Figure 21 Local blowing ratios for 1.0R profile.

Table 3 Averaged total pressures and mass flow rate ratios for 1.0R profile.

	P_T (Pa)		MFR_1/MFR_2	
	M 1.0	*M* 1.5	*M* 1.0	*M* 1.5
DR 1.0	677	1304	0.85	0.93
DR 1.5	490	877	0.76	0.88
DR 2.0	418	700	0.67	0.84

Figure 22 shows CFD predicted effectiveness contours at DR = 1.0, 1.5 and 2.0, and M = 1.5. When DR increases from 1.0 to 2.0, the effectiveness traces become wider and cover more region in the span-wise direction.

Note that different leading edge profiles result in different coolant mass flow rate distribution. Based on the CFD results (DR = 1.5, M = 1.0 and 1.5), for the same coolant flow condition, the difference of coolant MFR distribution for the three profiles is within 2%. We think the effect of leading edge profile on the film cooling effectiveness is more significant than the effect of coolant flow distribution. For example, the difference of coolant MFR from the stagnation row between 1.5R and 2.0R is less than 1%; However, the effectiveness for 1.5R is much higher than 2.0R in the stagnation region.

Comparisons of CFD simulations and PSP experiments in terms of span-wise averaged effectiveness for the 1.0 R profile are shown in Figure 23. In the stagnation row region ($0 < s/d < 5$), CFD is in good agreement with experiments. In the downstream region, CFD under predicts the effectiveness when $7 < s/d < 8$, and over predicts the effectiveness when $s/d > 8$. The reason may be because CFD under predicts the interaction between the coolant and the mainstream in the downstream region and the coolant is more attached to the surface resulting in higher film cooling effectiveness. CFD also under predicts the effectiveness between rows of cooling holes in the downstream region, which may be due to CFD under predicts the coolant lateral mixing.

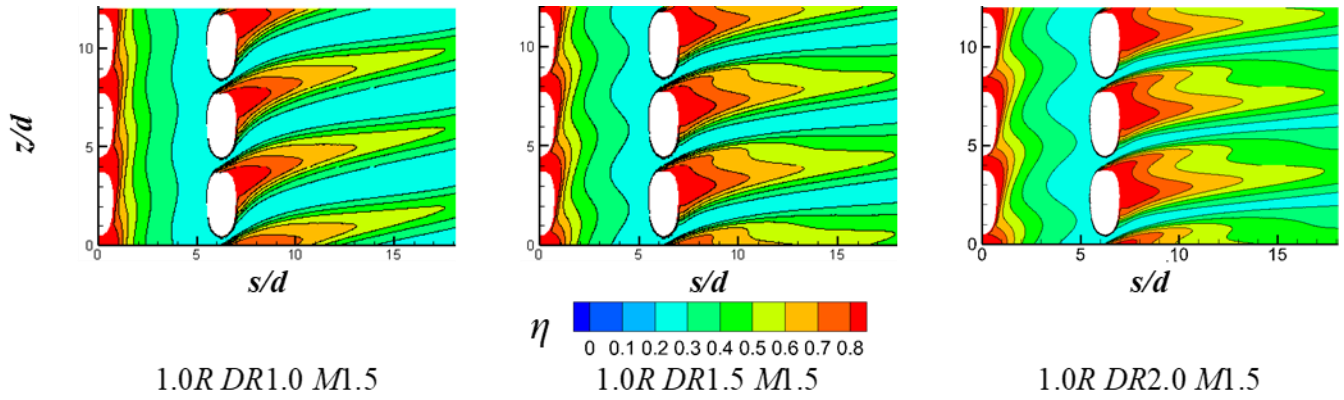

Figure 22 Film cooling effectiveness contour plot for 1.0R M1.5.

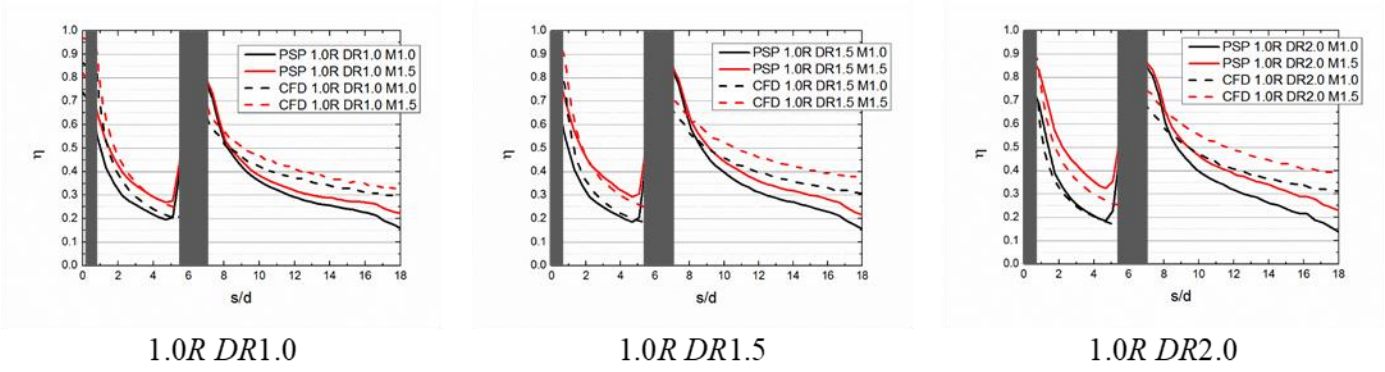

Figure 23 CFD predicted and PSP measured span-wise averaged film cooling effectiveness.

2.5 Conclusions

Film cooling effectiveness of three leading edge profiles is investigated using PSP measurement technique. Mass flow rates and local blowing ratios of cooling holes are calculated by CFD using RKE turbulence model to understand coolant distributions through each row of leading edge film holes. Generally, in the stagnation row region, span-wise averaged effectiveness and effectiveness contours obtained by CFD are in good agreement with experiments. However, in the downstream region, CFD always over predicts effectiveness about 30%. The main conclusions are drawn as follows.

Blowing Ratio Effect: In general, leading edge region film cooling effectiveness with radial-angle shaped holes increases with increasing blowing ratio (M = 0.5, 1.0, and 1.5) for three density ratios (DR = 1.0, 1.5, and 2.0) and three profiles.

Density Ratio Effect: At high blowing ratios (M = 1.0 and 1.5), film effectiveness increases with increasing density ratio. The coolant momentum decreases when density ratio increases, so the jet has a higher tendency to adhere to the surface. At low blowing ratio (M = 0.5), the reverse is generally true.

Leading Edge Profile Effect: At low density ratio (DR = 1.0), 1.0R is little better than 1.5R, while 2.0R is the worst due to its higher surface curvature in the stagnation region; the area-averaged effectiveness for 1.0R is about 5% and 20% higher than 1.5R and 2.0R respectively at M = 1.5, however, the profile effect reduces for lower blowing ratio. At high density ratio (DR = 2.0), 1.5R is the best, while 1.0R and 2.0R are about the same; the area-averaged effectiveness for 1.5R is about 10% higher than 1.0R and 2.0R for all tested blowing ratios.

3. INTERNAL HEAT TRANSFER OF FILM-COOLED LEADING EDGE MODEL WITH NORMAL AND TANGENTIAL IMPINGING JETS

3.1 Experimental Setup and Method

Figure 24 and Table 4 show the geometry of the leading edge model, which consist of a half cylinder, an impinging plate, and a rectangle plenum. The leading edge has three rows of film cooling holes, located at 0^o and $\pm 40^o$ of the leading edge half circle measured from the stagnation line. The leading edge external diameter is 7.62 cm, the leading edge thickness is 0.635 cm, and the height is 25.4 cm. The leading edge cavity is a half cylinder with internal diameter 6.35 cm and internal height 24.13 cm. For each row, there are 16 film cooling holes with diameter 0.318 cm. Hole spacing between two film cooling holes is 1.27 cm. Film cooling holes are at an inclined angle of 25^o relatives to the surface. The impinging plate also has 16 jet impinging holes with diameter 0.635 cm. There are two jet impingement designs: the normal jet and the tangential jet. The normal jet design has one row of 16 normal impinging holes which is perpendicular to the stagnation line. Note that for the normal jet, impinging holes and leading edge cooling holes are staggered in the span-wise direction. The tangential jet design has two rows of tangential impinging holes located tangentially to the leading edge half circle. Each row has 8 holes alternatively distributed on the two sides. The dimension of the rectangle plenum before the impingement plate is 6.35×5.08×50.8 cm. The coolant comes into the leading edge from the bottom. Through an inside rectangle plenum, it impinges on the leading edge internal surface from impinging holes, and discharges from leading edge film cooling holes. The leading edge cylinder is made of transparent Plexiglas in order to measure the internal heat transfer using transient liquid crystal method.

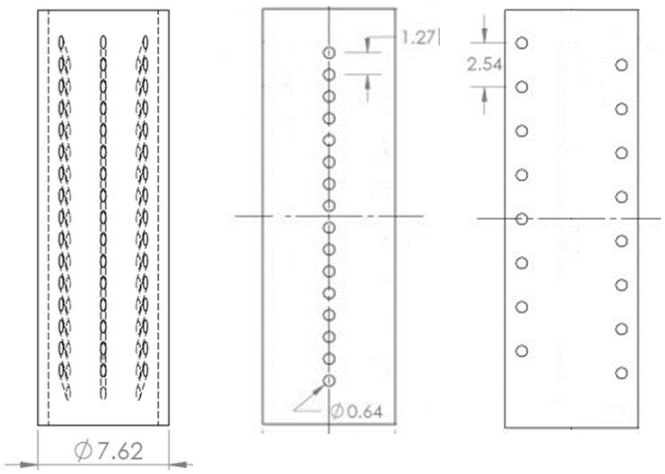

3 row film Normal jet Tangential jet

(a) Front view of leading edge and impinging plate

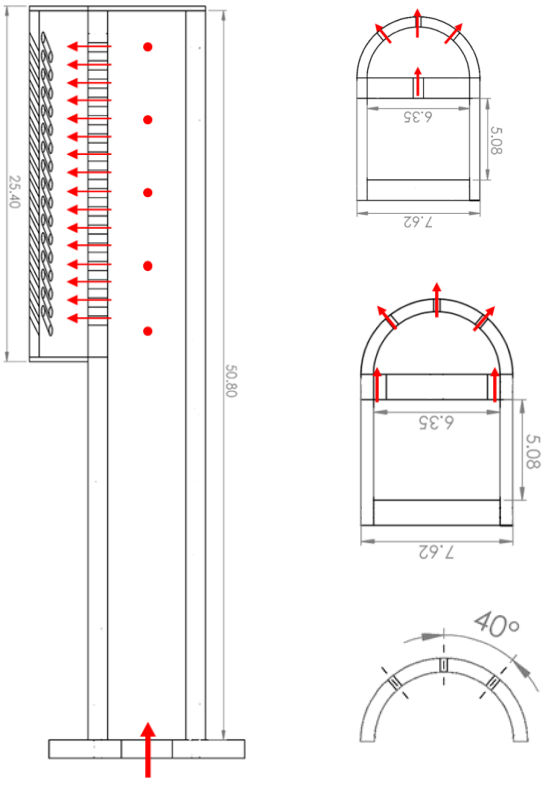

(b) Side view (c) Top view

Figure 24 Geometry of the leading edge model.

Table 4 Dimensions of the leading edge model.

Leading edge height (cm)	25.4
Leading edge external diameter (D, cm)	7.62
Leading edge thickness (cm)	0.635
Film cooling hole diameter (d_c, cm)	0.318
Film cooling hole to hole distance (p, cm)	1.27
Leading edge to hole diameter ratio (D/d_c)	24
Film cooling hole to hole spacing (p/d_c)	4
Angle to surface (α) (°)	25
Impinging hole diameter (d_j, cm)	0.635
Normal jet impinging hole to hole distance (cm)	1.27
Tangential jet impinging hole to hole distance (cm)	2.54
Impinging plate thickness (cm)	1.27

The experimental facility is a suction type low-speed wind tunnel. The wind tunnel width is 76.2 cm, height is 25.4 cm, and the distance between the turbulence grid and outlet to the suction blower is 185 cm. The mainstream velocity is about 20.89 m/s and mainstream Reynolds number is about 100,000 based on the cylinder's diameter. The turbulence intensity is 7% and the length scale is 0.127 cm. The stagnation line of the leading edge is at 70 cm downstream of the turbulence grid. Schematics and dimensions of the wind tunnel can see Zhang et al. [55] for detail.

Figure 25 shows the experimental setup schematically. In this study, transient liquid crystal method is applied to measure the internal heat transfer coefficient. The leading edge internal surface is painted with a thin layer of liquid crystal sprayer coating (Hallcrest R30C5W). The coolant air flow is supplied by an air compressor system with a rotameter to measure the air flow rate. A pipe heater is employed to heat the flow. A valve is used to guild the preheated air flow to the leading edge test section. Five thermocouples are placed in the rectangle plenum before the impinging plate to record the jet temperatures during the test, as noted in Figure 24(b). The inlet jet temperature for different x/d then is calculated by polynomial fitting. Figure 26 shows temperatures as functions of time at $Re_j = 10000$ for the normal jet.

A digital camera is used to capture the leading edge surface liquid crystal color change. The inlet temperatures and liquid crystal images are recorded every 0.5 seconds, and it takes about 1 to 2 minutes to finish the data recording process. The camera is located in the middle plane of the leading edge model. The direction is toward the second film cooling row (40º), with the 40º camera viewing angle from the stagnation line. After the experiments, images captured by the camera are coordinate transformed from pixels to the arc length in the half circle measured from the stagnation point and the height in the span-wise direction.

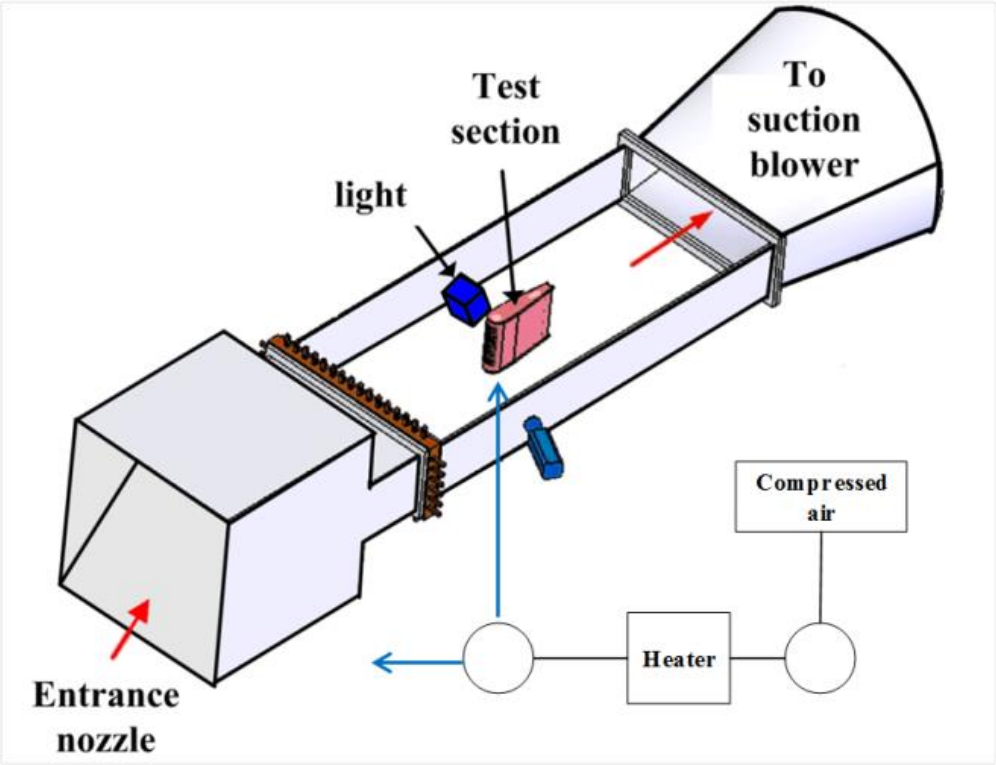

Figure 25 Schematic of experimental setup.

Due to the curved test surface and the angle between the camera and the light, a calibration test was carried out. In the calibration, a semi-cylindrical aluminum with outside diameter = 6.35 cm and inside diameter = 5.08 cm is attached to the leading edge internal surface. The aluminum internal surface is attached with a rubber heater to provide uniform heat flux. Figure 27 shows the schematics of camera view and calibration. Six thermocouples are embedded in the aluminum to measure the temperatures, with temperature difference less than 0.1 ºC during the calibration test. The thermocouples are located in the 0º and ±45º of the half circle. Three of them are in the leading edge midspan, as shown in Figure 4. The other three thermocouples are located in the plane with the distance of 6.35 cm measured from the hub. The distance between the thermocouples and the aluminum external surface is 0.16 cm. The calibration tests are performed under the same testing environment as experiments but without flow conditions. Based on the temperatures and the hue values, the hue to temperature relation at each point on the leading edge surface can be obtained. Figure 28 shows calibration curves. It includes three degrees, and three positions in the hub to tip direction which are the same as thermocouples Tc_2, Tc_3 and Tc_4. Here, temperature values are averaged by the six thermocouples. The stagnation line is at 0 degree and the side of half cylinder is at 90 degrees. It shows that at a fixed temperature, Hue value decreases when the degree increases.

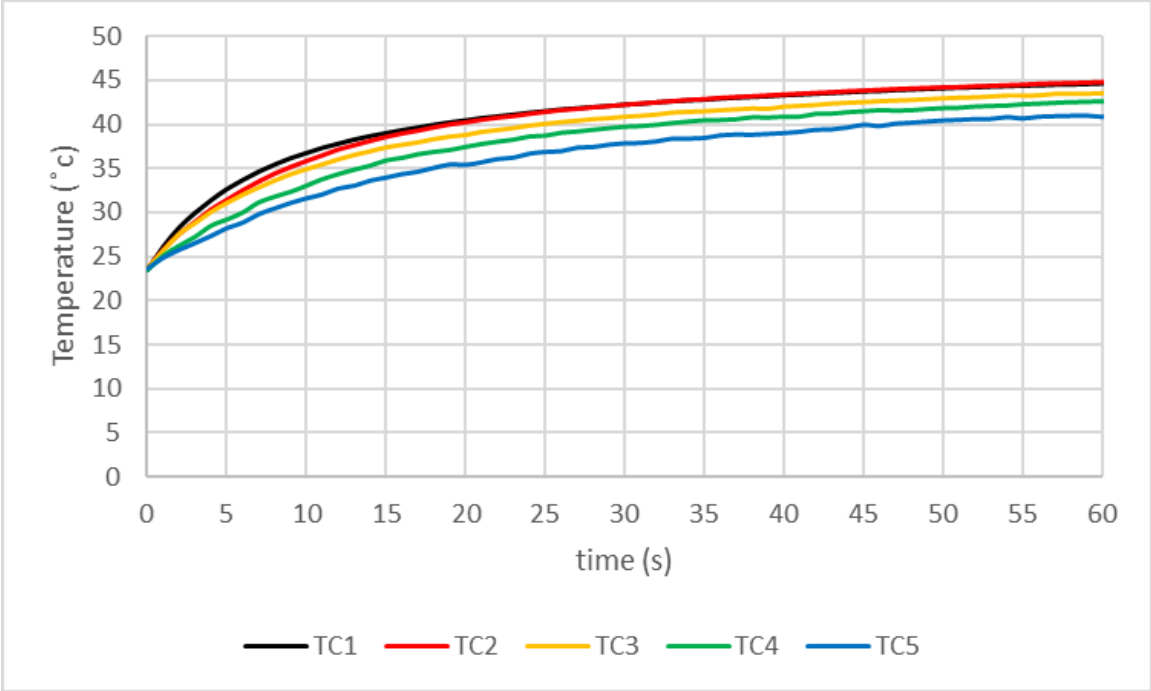

Figure 26 Jet inlet temperature as functions of time.

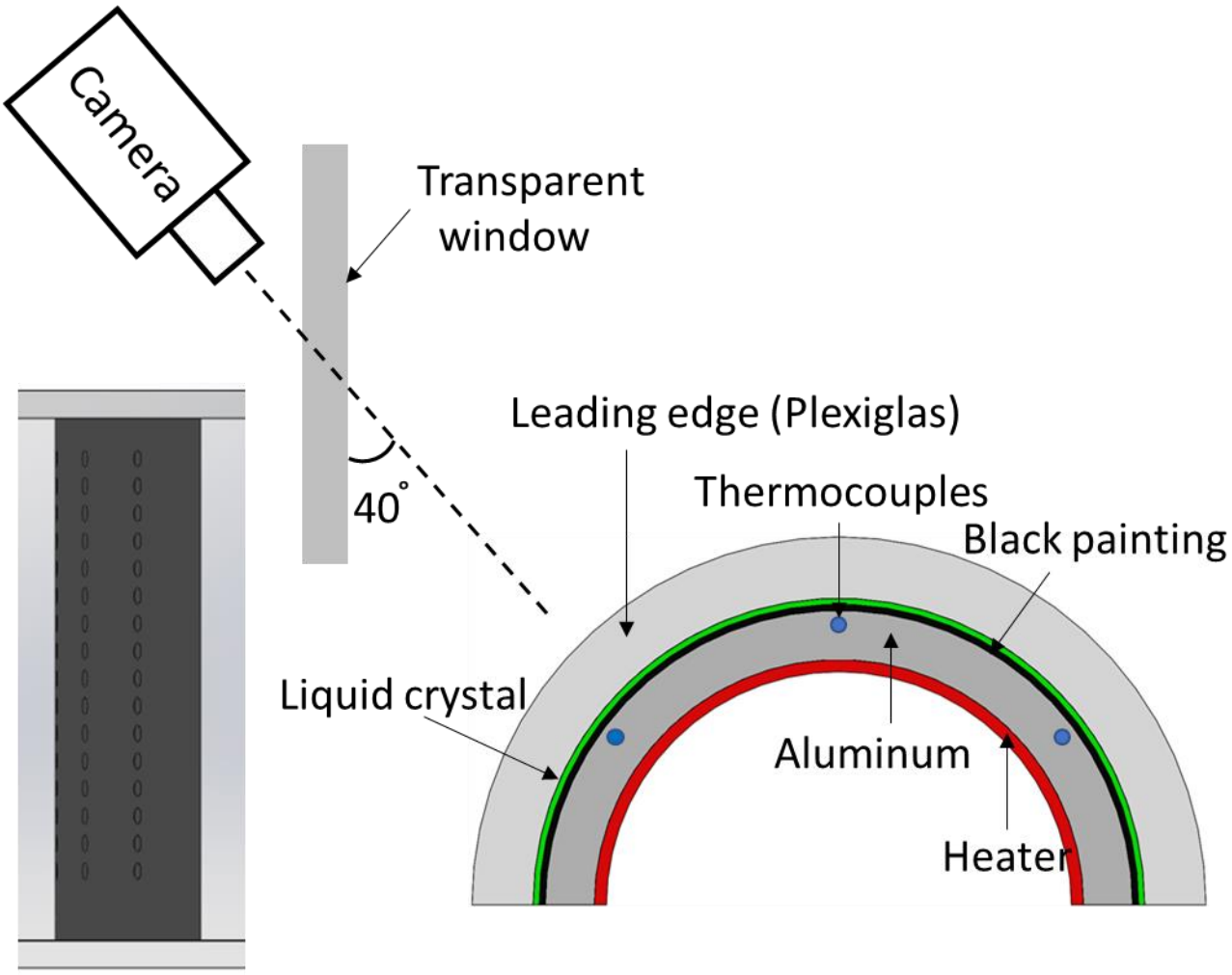

Figure 27 Schematic of the liquid crystal calibration and camera view.

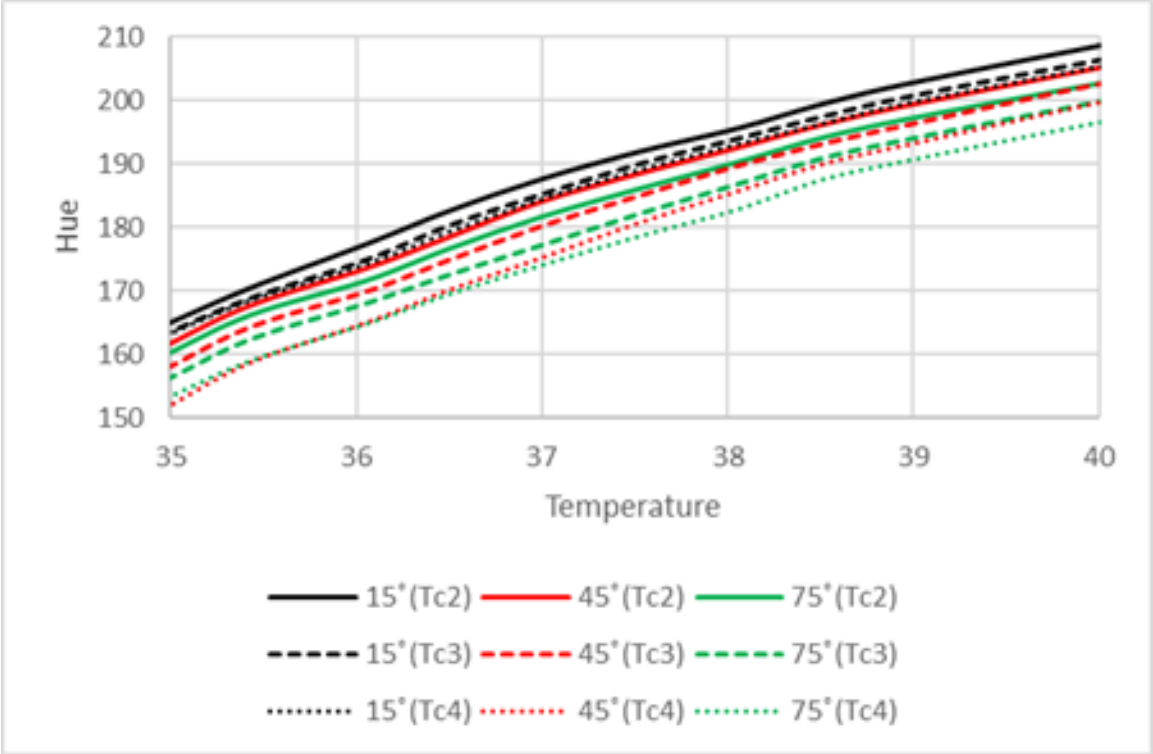

Figure 28 Liquid crystal calibration curves.

The leading edge test surface is made of Plexiglas and the thickness is 0.635cm. The assumption of one-dimensional semi -infinite transient conduction with convection boundary condition is applied. Using the Duhamel's superposition theorem, the test surface temperature can be calculated by as follows:

$$\frac{T_w - T_i}{T_m - T_i} = 1 - exp\left(\frac{h^2 \alpha t}{k^2}\right) erfc\left(\frac{h\sqrt{\alpha t}}{k}\right) \qquad (3.1)$$

$$T_w - T_i = \sum_{j=1}^{N} \left[1 - exp\left(\frac{h^2 \alpha (t - \tau_j)}{k^2}\right) \times erfc\left(\frac{h\sqrt{\alpha (t - \tau_j)}}{k}\right)\right] \left[\Delta T_{m_j}\right] \qquad (3.2)$$

Here $\Delta T_m \; and \; \tau_j$ are the temperatures and time step. The heat transfer coefficient h at each pixel can be obtained from Eq. (3.2) by knowing the initial surface temperature (T_i), impinging jet temperature (T_m) as a function of time measured by thermocouples and the surface temperature (T_w) measured by liquid crystal images. Details of this method are documented by Ekkad and Han [59].

The uncertainty of the jet Reynolds number is about 2%. The uncertainty of jet inlet temperature measured by thermocouples is about 2%. The uncertainty of experimental time reading is about 2%, the surface wall thermo-physical properties are about 3%. According to the method proposed by Kline and McClintock [60], the overall uncertainty in heat transfer coefficient calculations is estimated at 7%.

3.2 Numerical Setup and Method

Numerical simulations were done using ANSYS FLUENT 18.2. Grids including unstructured meshes and structured meshes were generated using ICEM CFD. Unstructured meshes are generated near the leading edge model and structured meshes are generated away from the leading edge to simulate the wind tunnel environment. There are 20 prism layers near the walls of leading edge, film cooling holes, impinging jet holes, and plenum with $y+ \leq 1$. The total number of meshes was about 18 million (16 million unstructured meshes and 2 million structured meshes). Mesh interface is used between the two types of meshes. The height and width of wind tunnel are 25.4 cm and 76.2 cm, respectively. The mainstream inlet is located 38.1 cm in front of the stagnation line of leading edge. Figure 29 shows schematic of the leading edge geometry with unstructured mesh. Figure 30 shows schematic of the computational meshes near the leading edge for the normal jet. Boundary conditions are summarized in Table 5. To calculate the internal heat transfer, constant heat flux 2000 W/m^2k is applied on the leading edge internal surface.

Two additional meshes were generated to test the grid independence, with total mesh number about 13 million and 26 million. Figure 31 presents the span-wise averaged Nu at Re_j = 10000 for three meshes using RKE model. Figure 32 shows the span-wise averaged Nu comparison between TLC and CFD at Re_j = 10000. Two turbulence models: RKE and SST are used. For the normal jet, SST model overpredicts Nu about 20% to 30% between film cooling rows; for the tangential jet, SST model overpredicts Nu about 20% to 30%. On the other hand, RKE model predicts well with TLC results. In addition, compared with Chupp's correlation in the stagnation line, RKE is also in good agreement with Chupp's correlation, but SST overpredicts the stagnation Nu. Figure 33 shows Nu contours by SST model. Nu contours by RKE model will be presented in the next section. Note that, for the tangential jet, the jet contour predicted by SST model is divided

into two branches after it attaches the half cylinder, which is different from TLC results. So, in this paper, we select the RKE model to simulate the leading edge internal heat transfer. Calculations were assumed converged when the residuals were in order 10^{-8} for energy, in order 10^{-5} for the continuity equation, and in order 10^{-6} for all other residuals.

Table 5 CFD boundary conditions.

Mainstream velocity (m/s)	20.89
Mainstream temperature (K)	296
Coolant temperature (K)	296
Internal surface heat flux ($W/m^2 \cdot K$)	2000
Coolant jet Reynolds number Re_j	5000,10000,15000

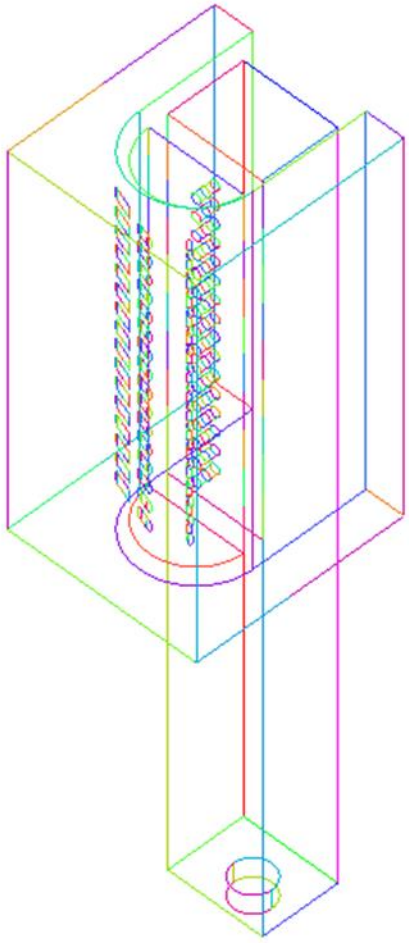

Figure 29 Schematic of CFD geometry with unstructured mesh.

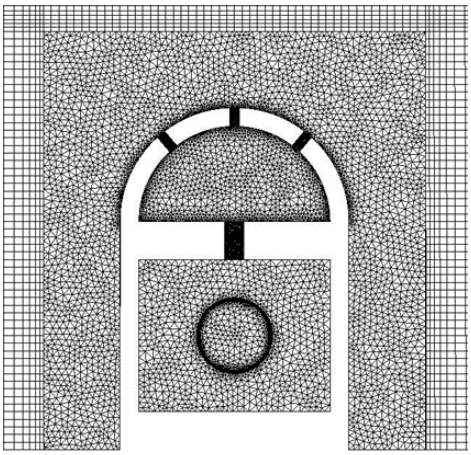

(a) Bottom view

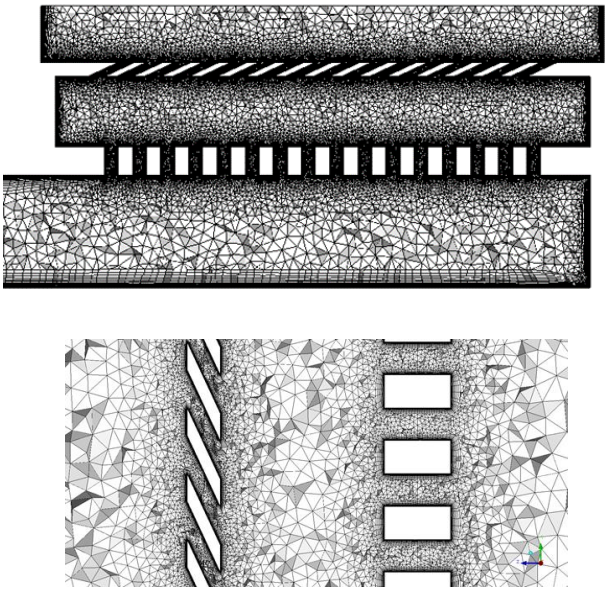

(b) Middle cut plane

Figure 30 Schematic of computational domain for the normal jet.

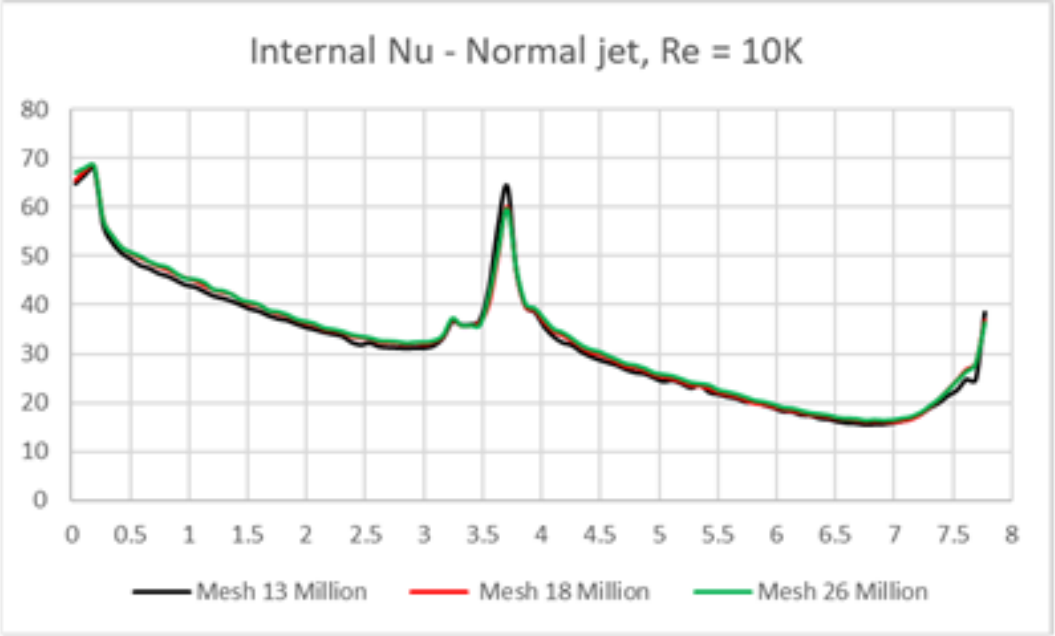

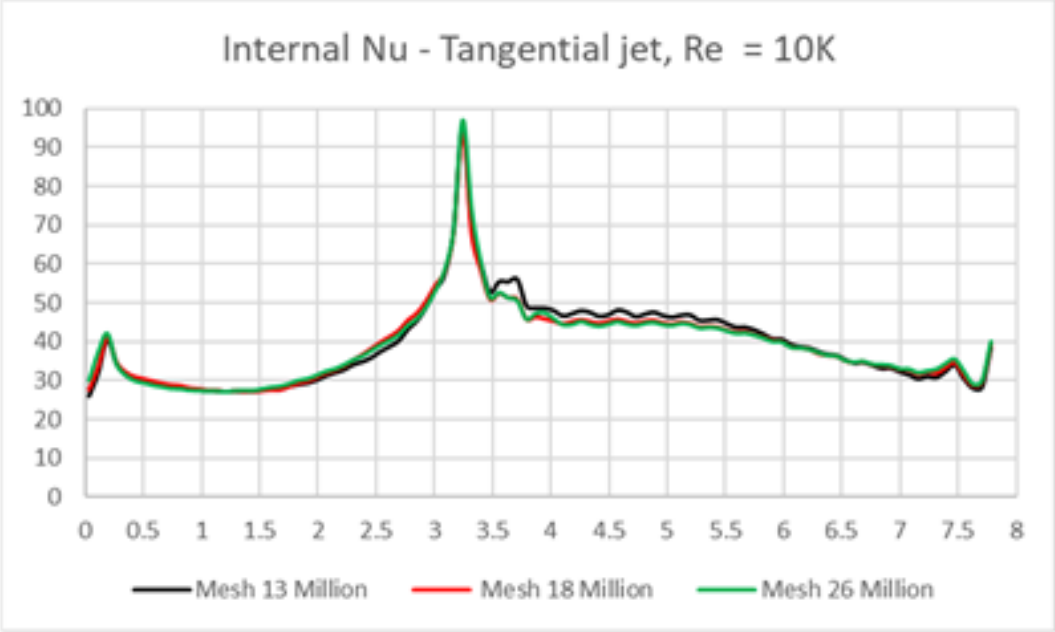

Figure 31 Grid independent test. RKE model.

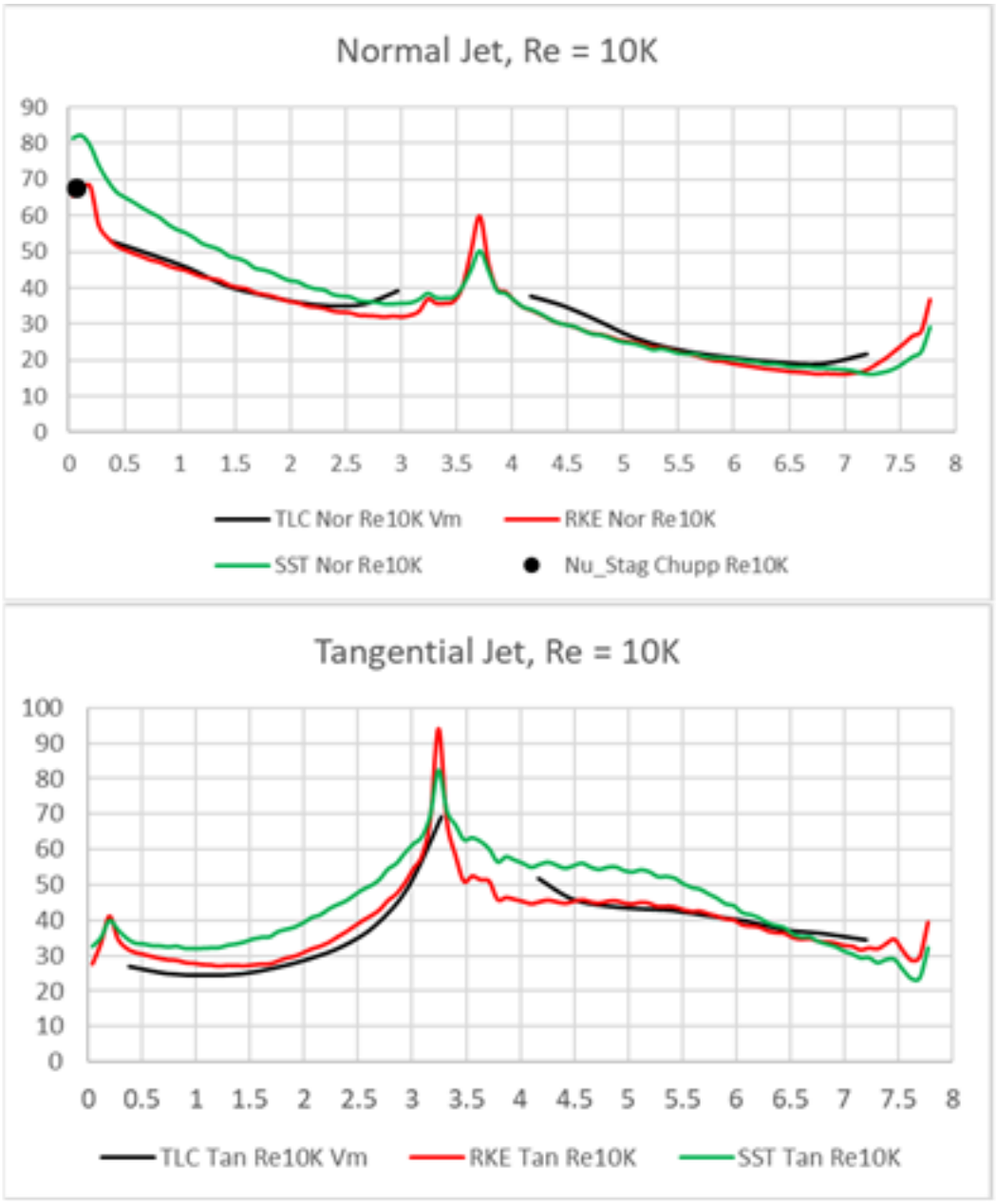

Figure 32 Comparison of span-wise averaged Nu between TLC, RKE and SST.

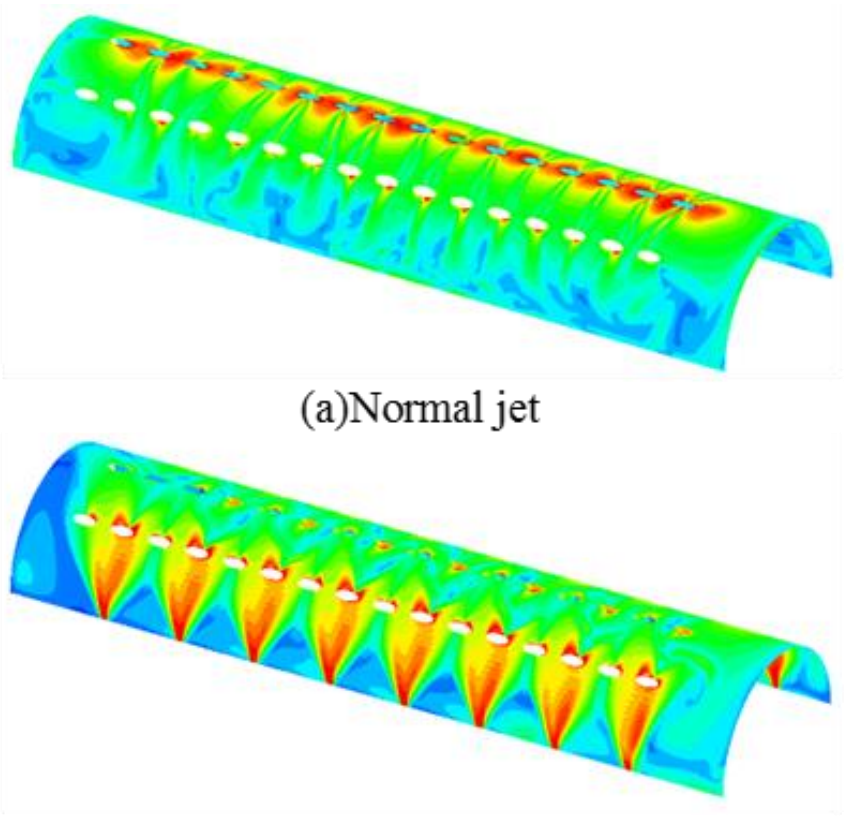

Figure 33 Nu contours by SST model.

3.3 Experimental Results and Discussion

In this section, leading edge internal heat transfer at jet Reynolds number Re_j = 5000, 10000 and 15000 with one row of normal jet or two rows of tangential jet are discussed. Experiments are conducted both with the mainstream flow and without the mainstream flow. Results are shown by Nu contours, span-wise averaged Nu, and stream-wise averaged Nu.

3.3.1 Nusselt number distribution

Figure 34 shows TLC Nu contours for the normal jet with and without mainstream flow. The stagnation row (0º) locates at s/d = 0 and the second row (40º) locates at s/d = 3.5. In the experiments, close to the film cooling rows, the view of leading edge internal surface which is painted with liquid crystal coating is blocked by the inclined film cooling holes surface (not transparent), so Nu data in the range 3 < s/d < 4 is not shown in the figures. Nu reaches the maximum in the stagnation region. High Nu values are observed around film cooling holes due to coolant entrance effect (thinner boundary layer around film cooling holes). After the second row (40º), Nu decreases as the boundary layer becomes thicker. Increasing Re_j increases Nu. For Re_j = 5000, Nu with mainstream is higher than without mainstream. For Re_j = 15000, Nu with mainstream and without mainstream are about the same.

Figure 35 shows TLC Nu contours for the tangential jet with and without mainstream flow. Periodical triangle shape contours are observed in the side of leading edge internal surface, as jets spread in the span-wise direction after attach on the leading edge side surface. For Re_j = 5000, mainstream decreases Nu before the second row and increases Nu after the second row. For Re_j = 10000 and 15000, a slight increase of Nu after the second row is observed with mainstream flow.

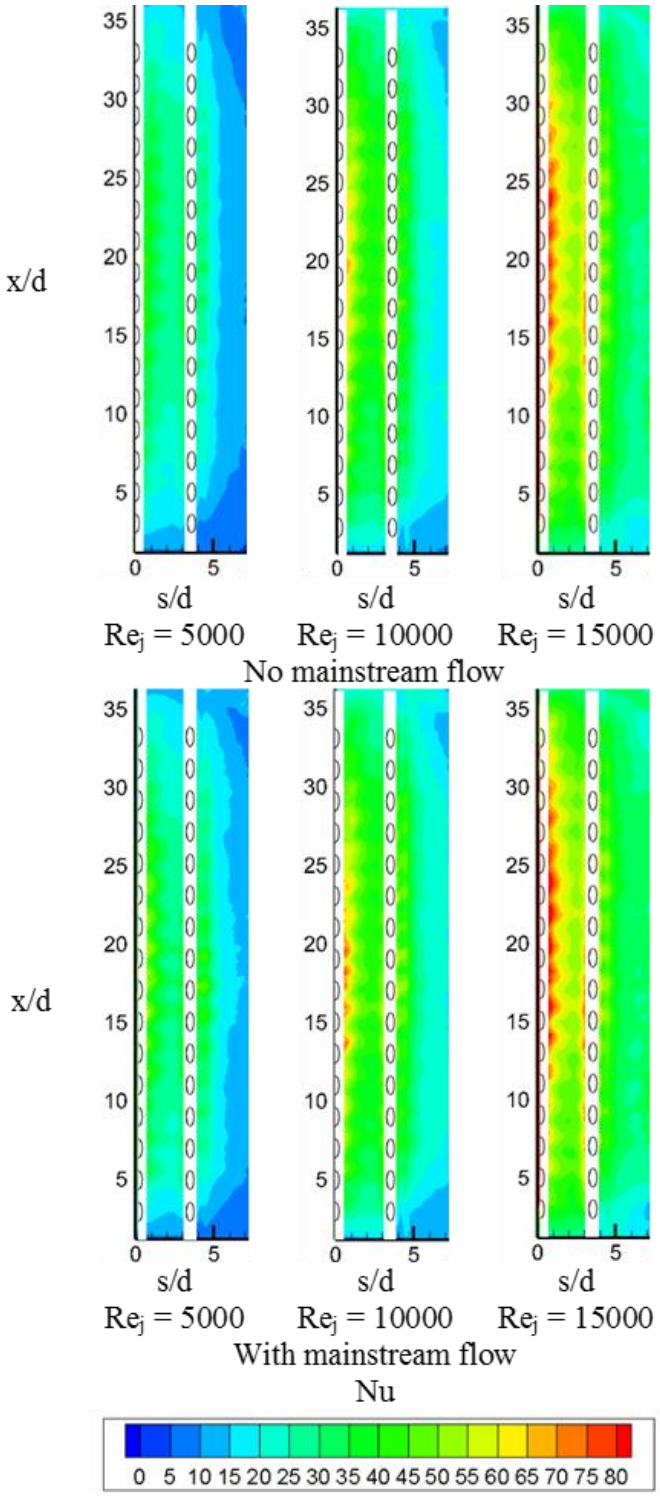

Figure 34 Nusselt number contours - TLC normal jet.

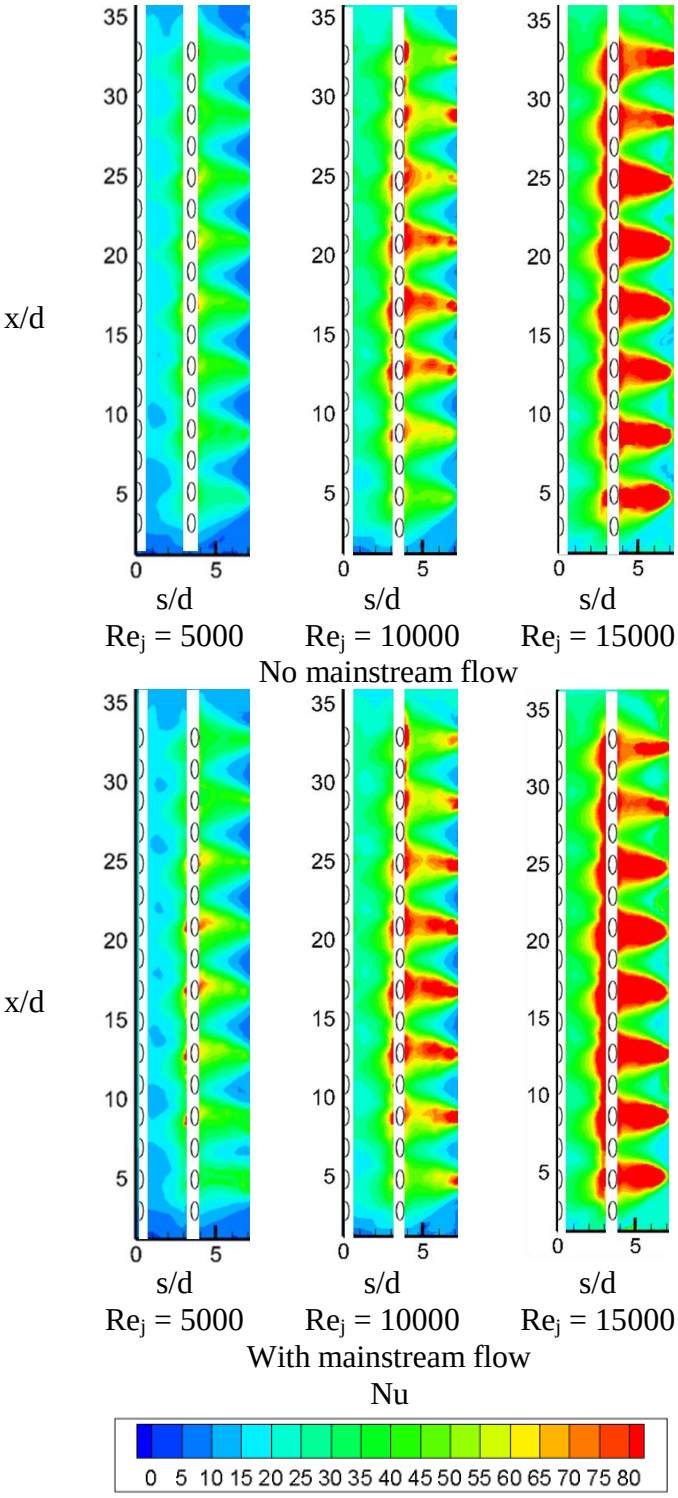

Figure 35 Nusselt number contours - TLC tangential jet.

3.3.2 Span-wise averaged Nusselt number

Figure 36 shows the span-wise averaged Nu by TLC. Note that the Nu data ($3 < x/d < 35$) is used to obtain the span-wise averaged Nu. For the normal jet, from the stagnation row ($s/d = 0$), Nu first decreases and then increases when approaching the second row ($s/d = 3.5$). After the second row, Nu decrease again. On the other hand, for the tangential jet, from the stagnation line, Nu first decreases a little and then increases. It reaches the maximum when approaching the second row and then decreases again in the downstream. In Figure 36, Nu Correlations at the stagnation line by Chupp et al. [25] are shown for comparison. Note that the correlation data is without film cooling holes in the stagnation region.

Then we consider the effect of mainstream on the span-wise averaged Nu. For the normal jet, in general, mainstream increases Nu. When Re_j =5000, Nu increases about 10% to 20% before the second row and increases about 20% to 30% after the second row. As Re_j increases, the mainstream effect decreases. For the tangential jet, when Re_j =5000, mainstream decreases Nu before the second row and increases Nu after the second row; when Re_j = 10000 and 15000, mainstream increases Nu after the second row. Mainstream effect also decreases when Re_j increases. After the second row, mainstream increase Nu about 10%, 10% and 5% for Re_j = 5000, 10000 and 15000, respectively.

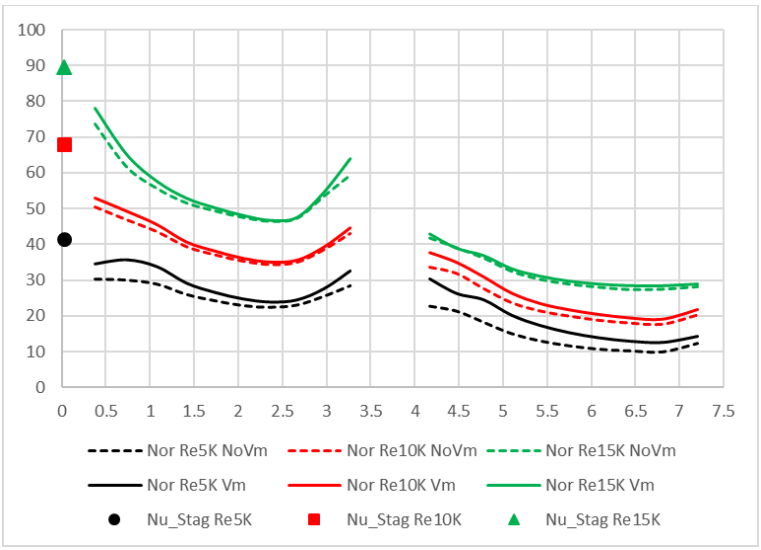

(a) Normal jet

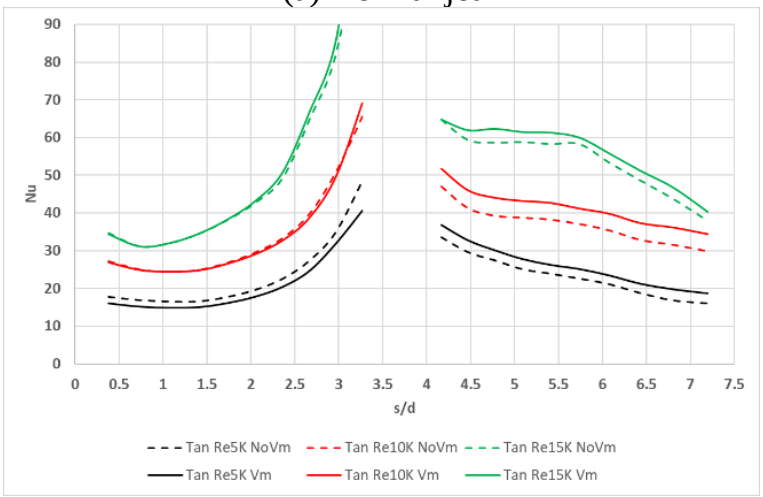

Tangential jet

Figure 36 Span-wise averaged Nu – TLC.

Mainstream will affect leading edge external surface pressure distributions and thus coolant flow rates discharged from each film cooling rows. Without mainstream, coolant flow from three film cooling rows is about the same. With mainstream, the external surface static pressure around the stagnation row is higher than the static pressure around the second row, thus the coolant from the stagnation row decreases and the coolant from the ±40 ° row increases. The difference of mass flow rate among cooling rows decreases when jet Reynolds number increases, so the mainstream effect decrease. Due to different impinging jet inlet locations and flow fields in the leading edge cavity, mainstream effect is different for the two designs. For the normal jet, jets impinge on the stagnation line. With mainstream, less coolant discharges directly through the stagnation row, so the vortex strength in the leading edge increases and Nu increases, compared with no mainstream. On the other hand, for the tangential jet, jet comes from one side (90°) and discharges through three rows (from 40°, 0° to -40°). With mainstream, more coolant comes out from the second row, so Nu increases between the side and the second row. As Re increases, the difference of flow rate among different rows decreases, so the mainstream effect will also decrease.

3.3.3 Stream-wise averaged Nusselt number

Figure 37 shows the stream-wise averaged Nu by TLC for the normal jet and the tangential jet. We can find that mainstream effect decreases as Re_j increases. Note that the data around film cooling holes ($3 < s/d < 4$) are not used in calculating stream-wise averaged Nu.

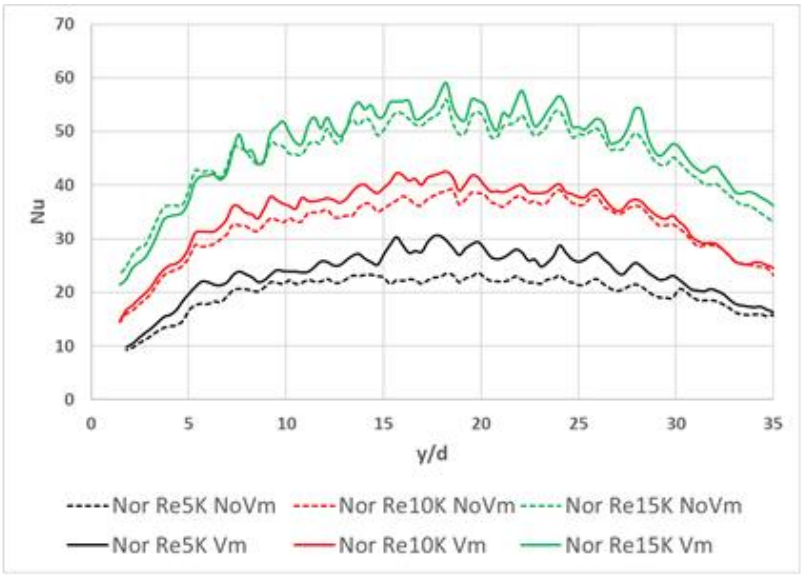

Normal jet

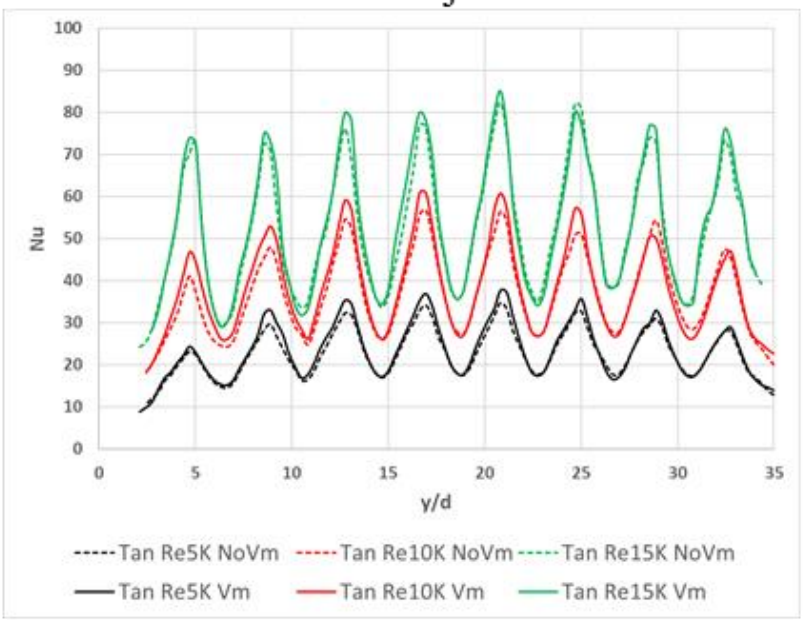

Tangential jet

Figure 37 Stream-wise averaged Nu - TLC.

3.4 Numerical Results and Discussion

In this section, CFD simulations using RKE model are carried out with mainstream flow. Results are shown by velocity magnitude contours and streamlines, Nu contours, followed by span-wise averaged Nu, stream-wise averaged Nu, and area averaged Nu.

3.4.1 Velocity contours and streamlines

Velocity magnitude contours and streamlines of leading edge jet impingement with film cooling are presented in Figure 38. Figure 38(a) and Figure 38(b) show velocity contours and streamlines in the symmetry cut plane. The coolant enters the rectangle plenum from the bottom, impinges on the leading edge internal surface through impinging holes, and discharges from film cooling holes. Figure 38(c) and Figure 38(d) show velocity contours in the middle cut plane. Local mainstream velocity increases from the stagnation line to the downstream. Note that for the tangential jet, the cut plane is in the middle of the left row of the tangential jet, and the velocity contour and flow pattern will reverse when the cut plane is in the middle of the right row.

It is found that the flow structure in the half cylinder is different for the two designs. See Figure 38(c) and Figure 38(d), for the normal jet, there are two symmetric vortexes in the leading edge cut plane. For the tangential jet, the two vortexes are not symmetry. One vortex is located near the second (40º) row in the same side of the tangential jet, which is generated by the interaction between the left side tangential jet and the reverse flow from the right side tangential jet. The other vortex is located between the second row and the impingement plate on the opposite side of the tangential jet. It should be pointed out that the vortex rotation directions of the two designs are also reverse. For the normal jet, the left vortex is in anticlockwise and the right vortex is in clockwise. For the tangential jet, the left vortex is in clockwise while the right vortex is in

anticlockwise. In the stagnation region, the flow direction is also different. For the normal jet, jets impinge on the stagnation line and discharges to the two sides; however, for the tangential jet, the flow direction is from right to left.

3.4.2 Blowing ratio distribution

Based on the total coolant mass flow rates and the wind tunnel mainstream velocity, the averaged blowing ratios are about 0.77, 1.54 and 2.31 for three jet Reynolds numbers. In addition, using the coolant mass flow rates from each film cooling rows obtained by CFD simulations and the wind tunnel mainstream velocity, we can calculate the local blowing ratios from each row. As shown in Figure 39, with mainstream, the local blowing ratio is about 0.5, 1.3 and 2.1 in the stagnation row and about 0.9, 1.6 and 2.4 in the second row for Re_j = 5000, 10000, and 15000, respectively. Note that local blowing ratio for the normal jet and the tangential jet is about the same at a given jet Reynolds number because the total pressure in the leading edge cavity is about the same and thus the coolant flow rate distribution is mainly dependent on the outside static pressure near the film cooling holes which is about the same for the two designs.

3.4.3 Nusselt number distribution

Detailed Nu contours are presented in Figure 40. Between the stagnation row and the second row, the normal jet is higher than the tangential jet; after the second row, the normal jet is lower than the tangential jet. The contours are similar to TLC. For the normal jet, after the second row, it is found that TLC is more uniform in the span-wise direction which means that RKE model may underpredict the coolant interaction and mix in this region.

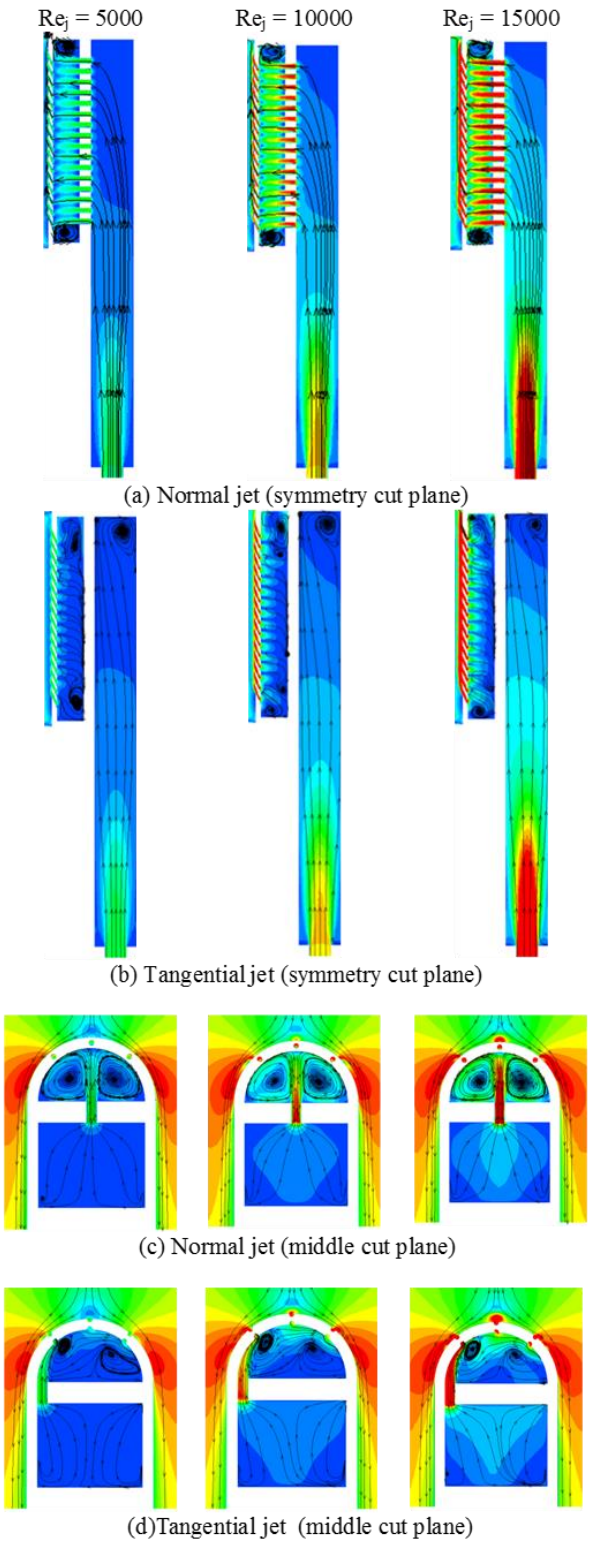

Figure 38 Velocity magnitude contours and streamlines.

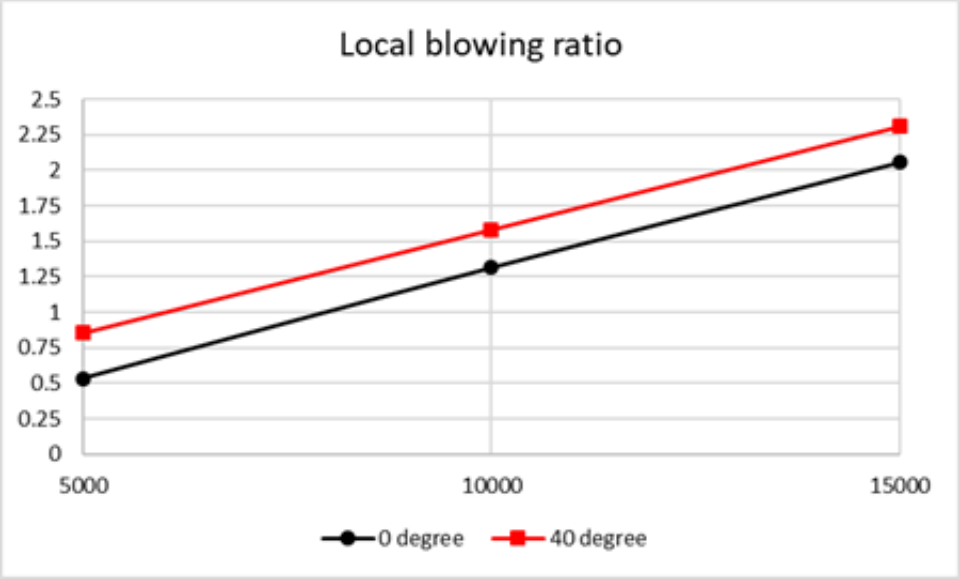

Figure 39 Local blowing ratio distribution.

3.4.4 Span-wise averaged Nusselt number

Figure 41 shows the comparison of span-wise averaged Nu between TLC and RKE with mainstream flow. Around the second row (s/d = 3.5), Nu peak value is observed in the downstream of coolant flow, that is 3 < s/d < 3.5 for the tangential jet and 3.5 < s/d < 4 for the normal jet. When Rej = 5000, for the normal jet, RKE under predicts Nu about 10% to 30%; for the tangential jet, the difference between RKE and TLC is less than 20%. When Rej = 10000 and 15000, RKE agrees well with TLC. Compared the normal jet and the tangential jet, it is found that for about 0 < s/d < 2.5, the normal jet is higher than the tangential jet; for about s/d > 2.5, the normal jet is lower than the tangential jet.

3.4.5 Stream-wise averaged Nusselt number

Figure 42 shows the stream-wise averaged Nu by RKE with mainstream flow. Results show that the tangential jet is higher than the normal jet. Note that Nu data is averaged from -90^o to 90^o of the half circle in the CFD; while, Nu data is averaged from 0^o to 90^o in the experiments.

3.4.6 Area averaged Nusselt number

Figure 43 presents area averaged Nu on the whole leading edge internal surface for three Reynolds number and two jet holes position designs. Increases Re_j increases Nu. Compared the normal jet and the tangential jet, it is found that with mainstream, the tangential jet is higher than the normal jet about 20%, 15%, and 18%, for varying Re_j from 5000, 10000 to15000.

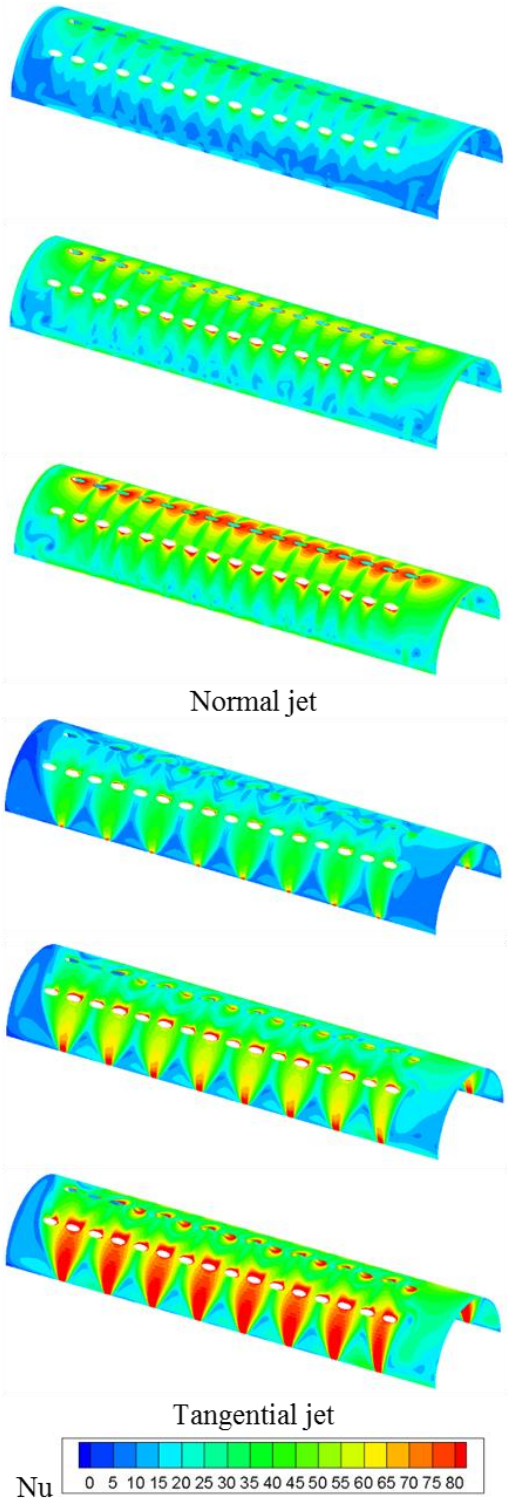

Figure 40 Nusselt number contours – RKE.

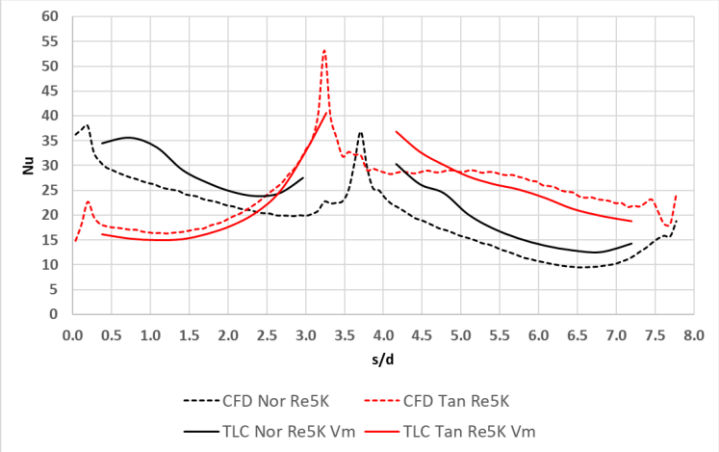

$Re_j = 5000$

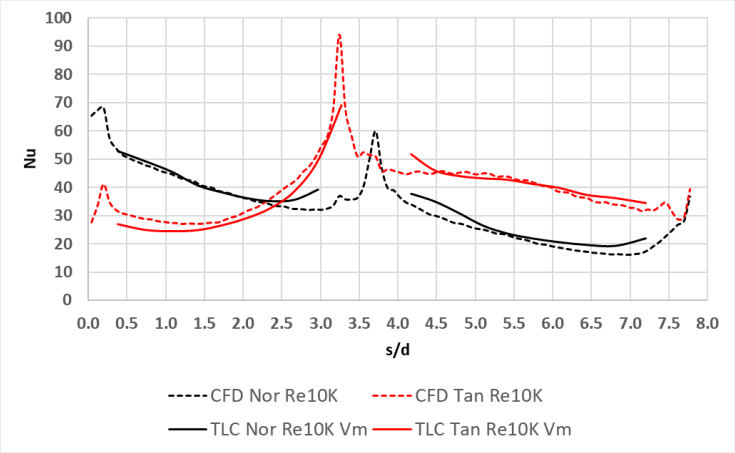

$Re_j = 10000$

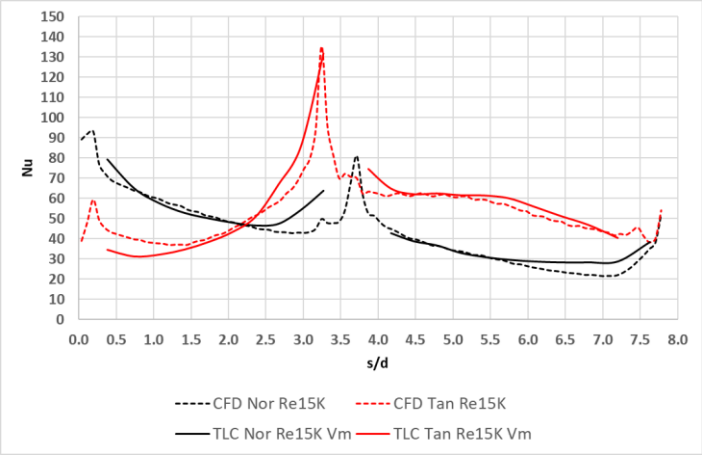

$Re_j = 15000$

Figure 41 Span-wise averaged Nu - TLC and RKE.

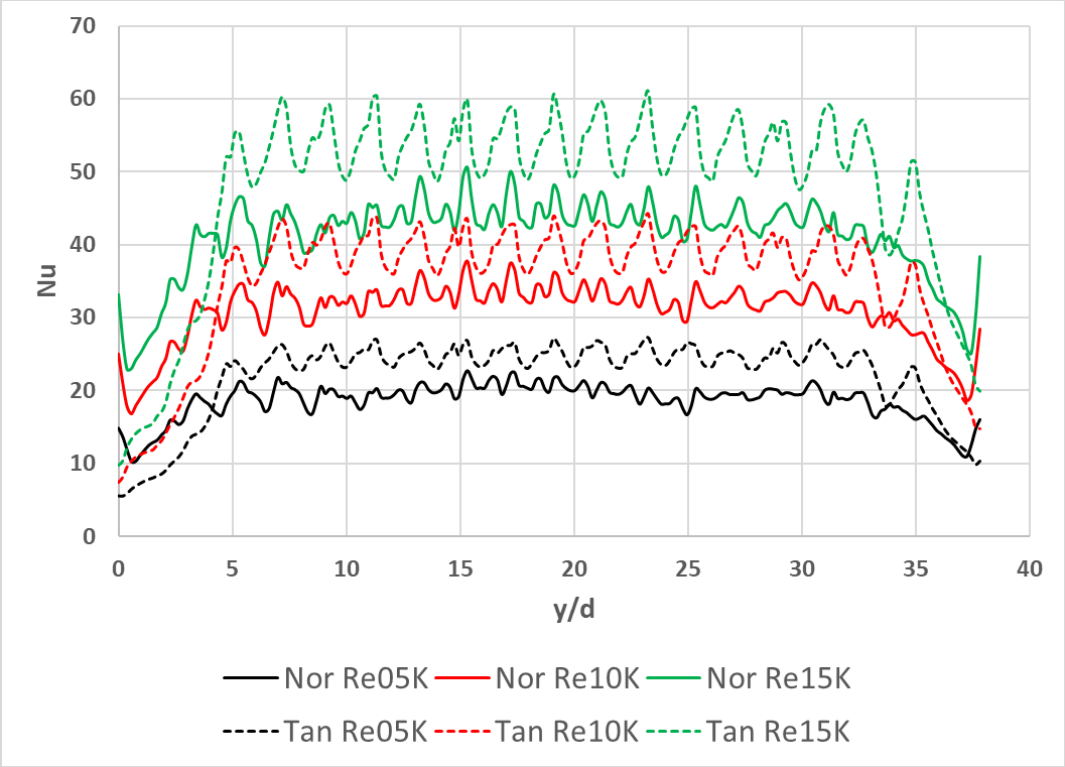

Figure 42 Stream-wise averaged Nu – RKE.

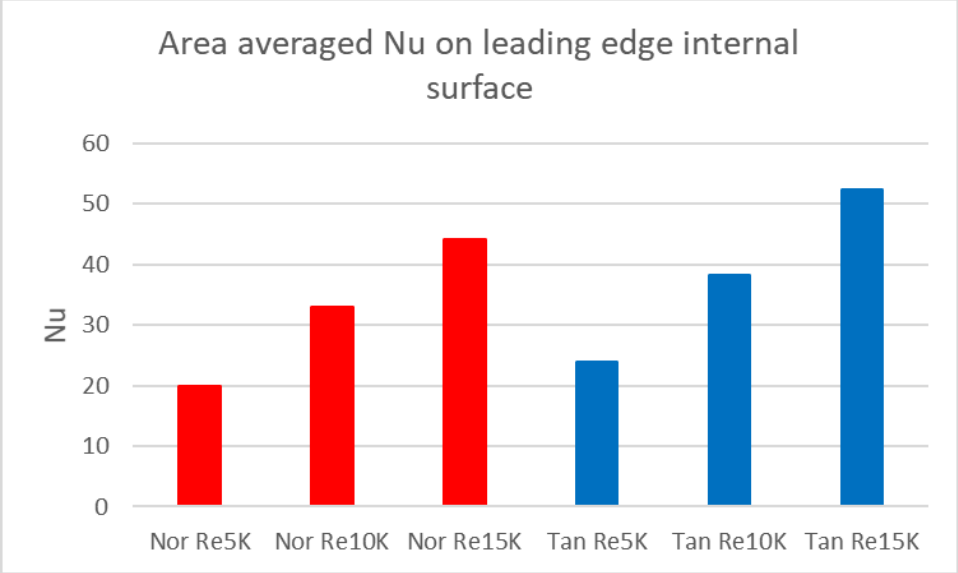

Figure 43 Area averaged Nu on leading edge internal surface.

3.4.7 Nusselt number on the film cooling hole surface

The Nusselt number on the film cooling hole surface is calculated using RKE model. Figure 44 and Figure 45 show Nu contours at Re_j = 10000 for two designs. Coolant flow directions are schematically presented. It is observed that, for a film cooling hole, Nu is higher on the side facing the coolant flow and lower on the other side. For example, for the normal jet, in the 40° row, Nu is higher on the side away from the stagnation line, as the coolant flow direction is from the stagnation line (0°) to the side of half circle (90°). Figure 46 shows area averaged Nu on the film cooling hole surface. In the stagnation row, the normal jet is higher than the tangential jet; in the second row, the normal jet is lower than the tangential jet.

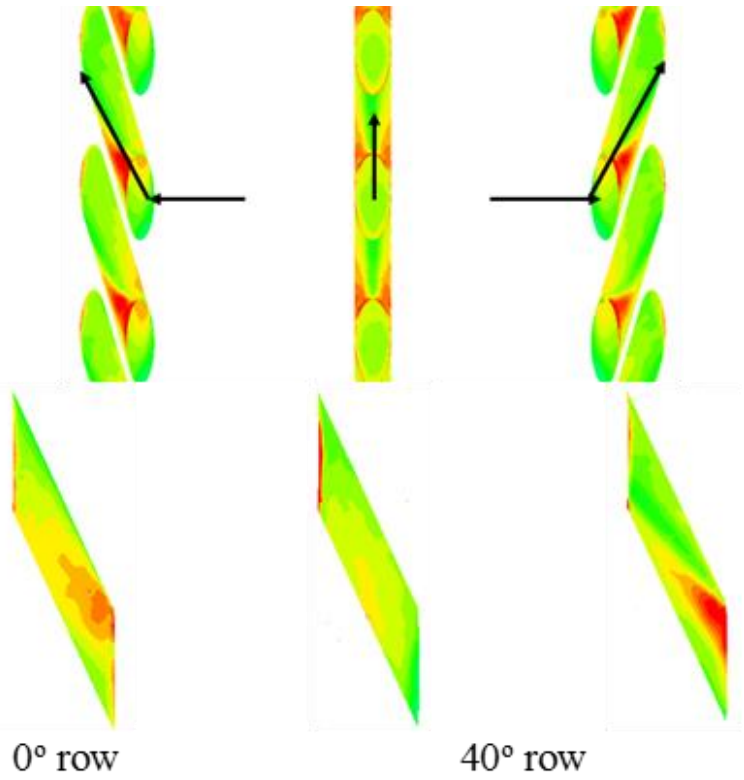

Figure 44 Nu contour on the film cooling hole surface for the normal jet.

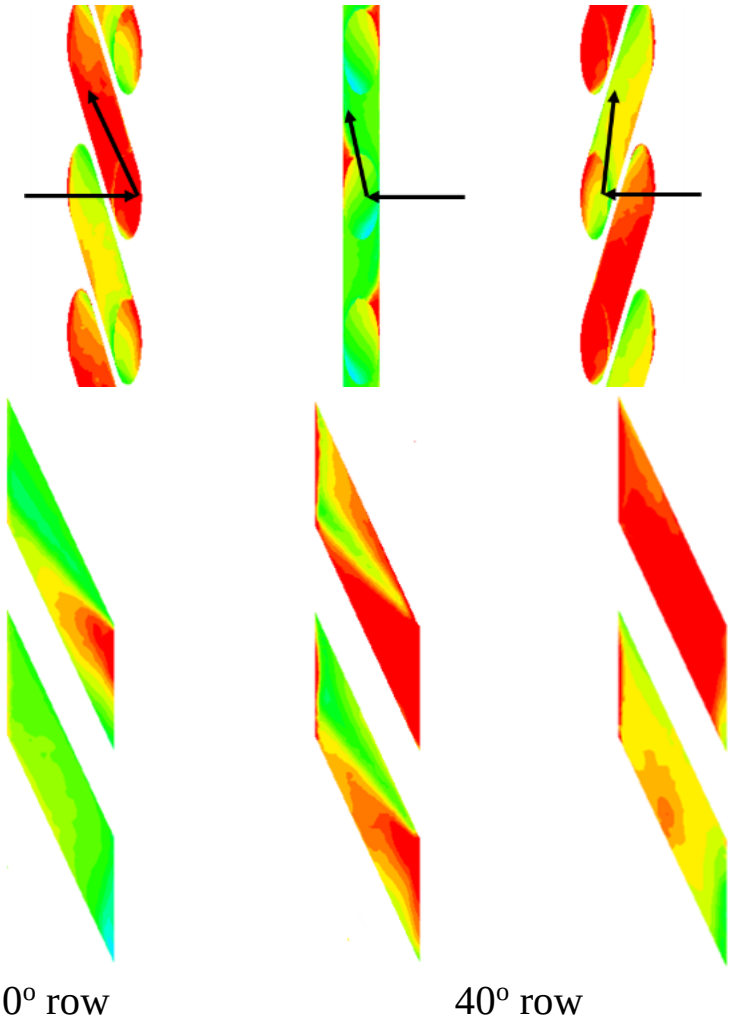

Figure 45 Nu contour on the film cooling hole surface for the tangential jet.

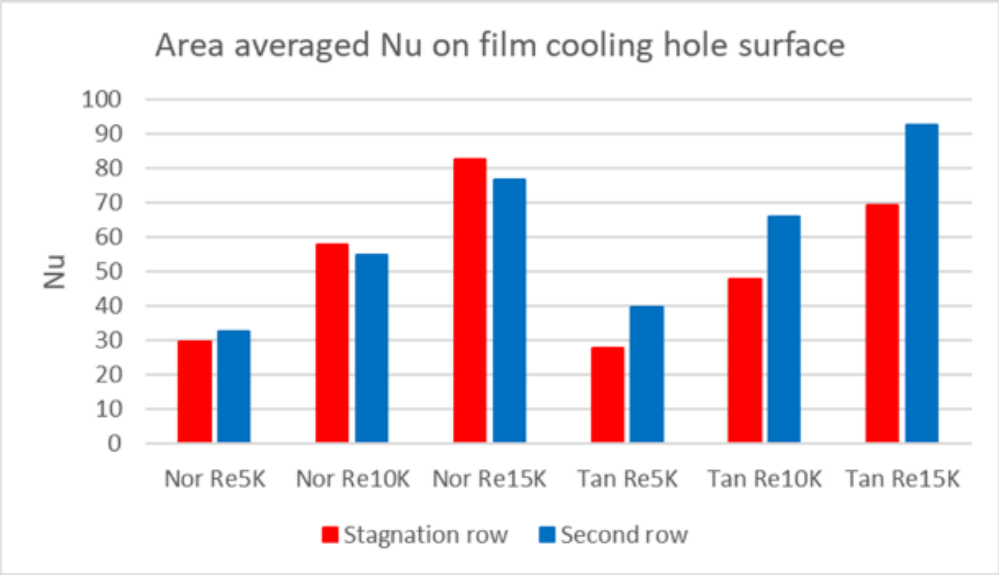

Figure 46 Area averaged Nu on film cooling hole surface.

3.5 Conclusions

We studied internal heat transfer of film-cooled leading edge with normal and tangential impinging jets. The main conclusions are drawn as follows.

Two impinging jet position designs show different jet spread, velocity and vortex structures in the leading edge cavity, resulting in different internal heat transfer distributions. For the normal jet, Nu is high in the stagnation region due to jet impingement. Nu is low on the two sides of leading edge as the increase of boundary layer thickness. For the tangential jet, Nu is low in the stagnation region. Triangle shape Nu contours are observed alternatively on the two sides, as the tangential jet spread in the span-wise direction after attaching on the leading edge internal surface. The normal jet is higher than the tangential jet for about $s/d < 2.5$, and the normal jet is lower than the tangential jet for about $s/d > 2.5$. For area averaged Nu, the tangential jet is higher than the normal jet. CFD Results show that, with mainstream, area averaged Nu on leading edge internal surface for the tangential jet is about 15% to 20% higher than the normal jet.

Mainstream can affect the internal heat transfer, as it changes coolant flow rate distribution for different rows of film cooling holes. The effects are different for the normal jet and the tangential jet because of different jet inlet locations and coolant flow distributions. For the normal jet, at $Re_j = 5000$, mainstream flow increase Nu by about 10% to 20% in the stagnation region and increases Nu by about 20% to 30% after the second cooling row. The influence of mainstream flow on heat transfer decreases with increasing jet Reynolds number. At $Re_j = 10000$, mainstream flow increases Nu less than 5% in the stagnation region and about 10% after the second film cooling row. At $Re_j = 15000$, mainstream effect is very small. For the tangential jet, after the second row, mainstream increase Nu about 10%, 10% and 5% for $Re_j = 5000$, 10000 and 15000, respectively.

4. OVERALL EFFECTIVENESS OF FILM-COOLED LEADING EDGE MODEL WITH NORMAL AND TANGENTIAL IMPINGING JETS

4.1 Experimental Setup and Method

Figure 47 and Table 6 show the geometry of the leading edge model, which consist of a half cylinder, an impinging plate, and a rectangle plenum. The leading edge external diameter is 7.62 cm, the thickness is 0.635 cm, and the height is 25.4 cm. The internal height of the half cylinder cavity is 24.13 cm. The leading edge has three rows of film cooling holes, which is located at 0^o and $\pm 40^o$ of the half circle measured from the stagnation line. For each film cooling row, there are 16 film cooling holes with diameter 0.318 cm and hole spacing 1.27 cm. Film cooling holes are at an inclined angle of 25^o relatives to the surface. The jet impinging plate includes 16 jet impinging holes with diameter 0.635 cm. There are two jet impinging designs in this study: the normal jet and the tangential jet. The normal jet design has one row of 16 normal jet impinging holes which is perpendicular to the stagnation line. The jet impinging holes and leading edge cooling holes are staggered in the span-wise direction. The tangential jet design has two rows of tangential jet impinging holes located tangentially to the leading edge half circle. Each tangential jet row has 8 holes alternatively distributed on the two sides. The dimension of the rectangle plenum before the impingement plate is 6.35×5.08×50.8 cm. The coolant comes into the leading edge from the bottom. Through an inside rectangle plenum, it impinges on the leading edge internal surface from impinging holes, and discharges from leading edge film cooling holes, as presented in Figure 47(b). The leading edge cylinder is made of a Mica-filled PTFE material with thermal conductivity K = 0.764 W/mK. The jet impinging plate and rectangle plenum are made of Plexiglas with thermal conductivity K = 0.2 W/mK.

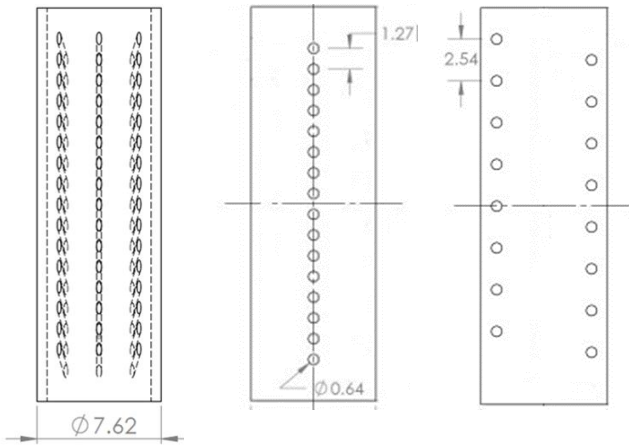

3 row film Normal jet Tangential jet

(a) Front view of leading edge and impinging plate

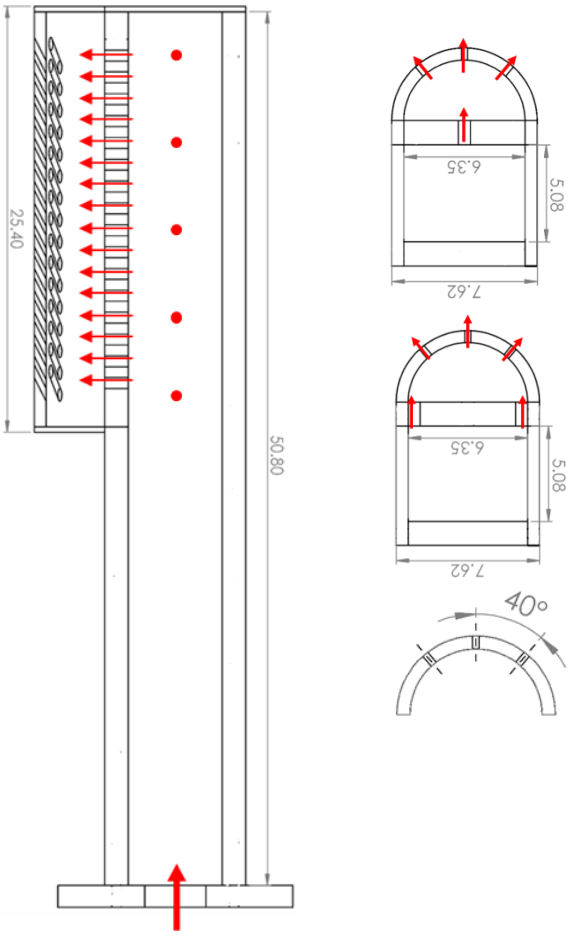

(b) Side view (c) Top view

Figure 47 Geometry of the leading edge model.

Table 6 Dimensions of the leading edge model.

Leading edge height (cm)	25.4
Leading edge external diameter (D, cm)	7.62
Leading edge thickness (cm)	0.635
Film cooling hole diameter (d_c, cm)	0.318
Film cooling hole to hole distance (p, cm)	1.27
Leading edge to hole diameter ratio (D/d_c)	24
Film cooling hole to hole spacing (p/d_c)	4
Angle to surface (α) (°)	25
Impinging hole diameter (d_j, cm)	0.635
Normal jet impinging hole to hole distance (cm)	1.27
Tangential jet impinging hole to hole distance (cm)	2.54
Impinging plate thickness (cm)	1.27

In this study, we use a suction type low-speed wind tunnel. The wind tunnel width is 76.2 cm, height is 25.4 cm, and the distance between the turbulence grid and outlet to the suction blower is 185 cm. The mainstream velocity is about 20.89 m/s, and mainstream Reynolds number is about 100,000 based on the external diameter of the leading edge. The turbulence intensity is 7%, and the turbulence length scale is 1.27 cm. The stagnation line of the leading edge is at 70 cm downstream of the turbulence grid.

Figure 48 shows the experimental setup schematically. Steady state liquid crystal technique is applied to measure the leading edge external surface temperature. The leading edge external surface is painted with a thin layer of liquid crystal sprayer coating (Hallcrest R25C10W). The coolant air flow is supplied by an air compressor system with a rotameter to measure the air flow rate. A pipe heater is employed to heat the flow. In the experiments, mainstream temperature is about 298K and coolant inlet temperature is about 318K. Five thermocouples are placed in the rectangle plenum before the impinging plate to record the coolant temperature during the test, as noted in Figure 47(b). The coolant inlet temperature is then obtained by polynomial fitting based on the temperatures of the five thermocouples. Four thermocouples are places in the upstream of the leading edge test section to measure the mainstream temperature, with temperature difference less than 0.1 ºC during the experiments. A digital camera is used to capture the liquid crystal color change. The camera is located in the middle plane of the leading edge model. The direction is toward the second film cooling row (40º), with camera viewing angle of 40º from the stagnation line. The overall effectiveness is then obtained when the values reach the steady state.

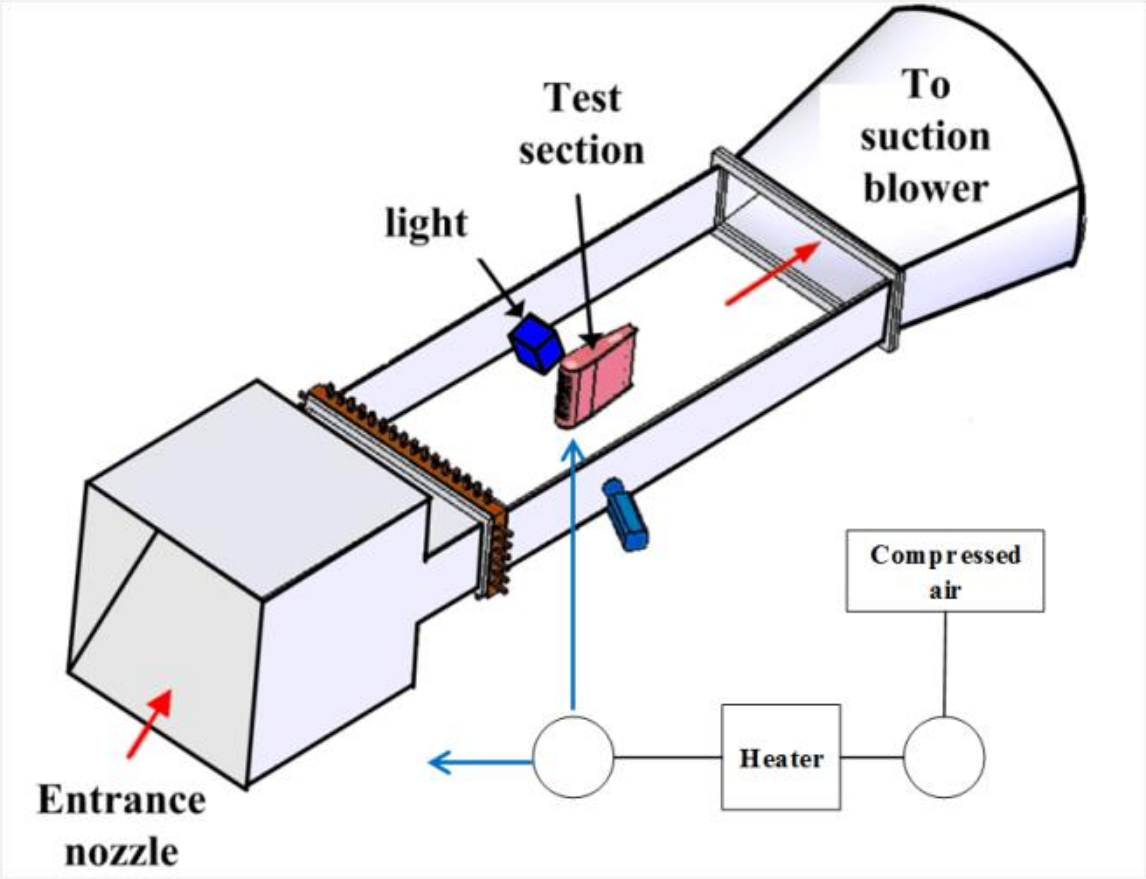

Figure 48 Schematic of experimental setup.

Figure 52 shows the schematics of leading edge conjugate heat transfer. Here, T_c is the coolant temperature, T_∞ is the mainstream temperature, q''_f is the heat flux from the mainstream to the leading edge solid material, q''_{in} is the heat flux from the the leading edge solid material to the coolant, T_{film} is the driven temperature, h_f is the external heat transfer coefficient, h_i is the internal heat transfer coefficient, k is the solid material thermal conductivity, T_w is the leading edge external surface temperature, $T_{w,in}$ is the leading edge internal surface temperature, $T_{c,out}$ is the coolant temperature in the film cooling hole exit. We have $q''_f = h_f\left(T_{film} - T_w\right)$ and $q''_{in} = h_i\left(T_{w,in} - T_c\right)$

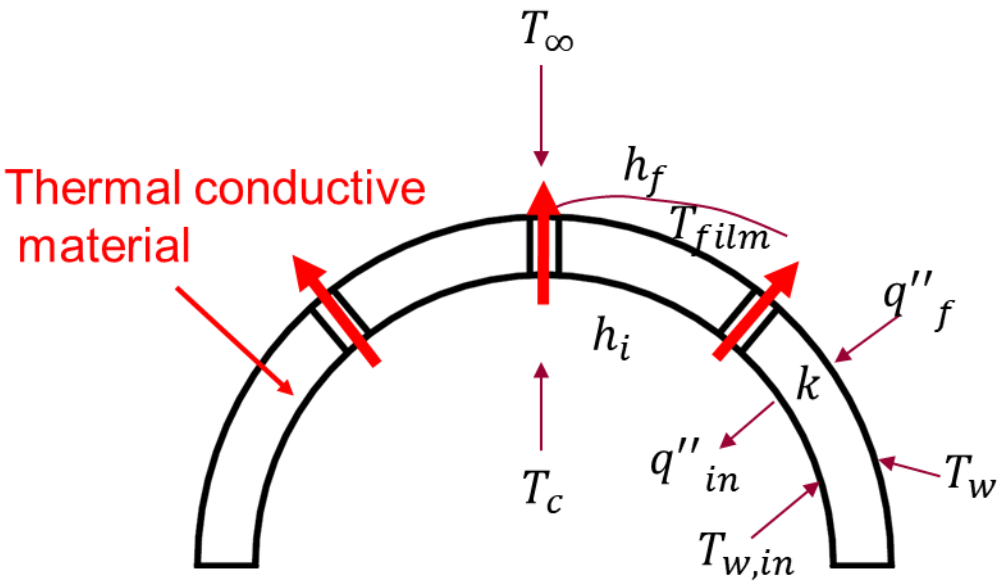

Figure 49 Schematic of leading edge conjugate heat transfer.

Overall effectiveness ϕ is defined as

$$\phi = \frac{T_m - T_w}{T_m - T_{c_{in}}} \tag{4.1}$$

, where T_m, $T_{c_{in}}$, T_w are mainstream temperature, coolant inlet temperature, and external wall temperature, respectively.

A liquid crystal calibration test was carried out, due to the curved test surface and the angle between the camera and the light. In the calibration, the leading edge is replaced by a semi-cylindrical aluminum with the same external diameter = 7.62 cm and internal diameter = 6.35 cm. The external surface of the semi-cylindrical aluminum is also painted with black painting and liquid crystal coating. The aluminum internal surface is attached with a rubber heater. Figure 50 shows schematics of the semi-cylindrical aluminum, the rubber heater, the thermocouples positions and the impinging plate. Six thermocouples are embedded in the aluminum to measure the temperatures, with temperature difference less than 0.2 C during the calibration test. The distance between the thermocouples and the aluminum external surface is 0.16 cm. The calibration tests are performed under the same testing environment as experiments but without flow conditions. Based on the temperatures and the hue values, the hue to temperature relation at each point on the leading edge surface can be obtained. It is found that the hue to temperature relation is mainly dependent on the degrees of the half cylinder. Figure 51 shows calibration curves at different degrees of the leading edge half cylinder. Here, Hue values are averaged for a given degree, temperature values are averaged by the six thermocouples. The stagnation line is at 0 degree and the side of half cylinder is at 90 degrees. It shows that at a fixed temperature, Hue value decreases when the degree increases. As temperature increases, Hue variation for different degrees decreases.

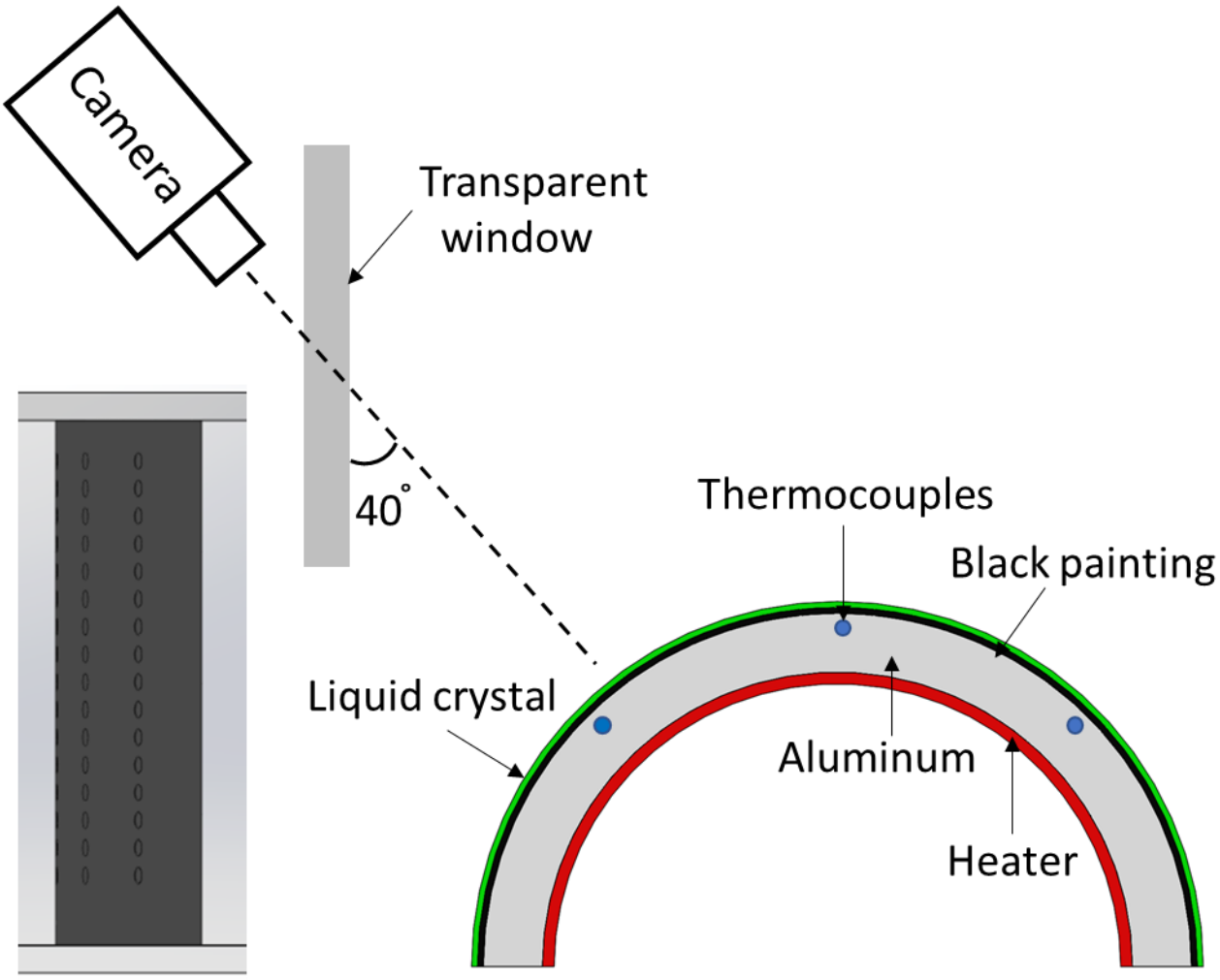

Figure 50 Camera view of test section and calibration.

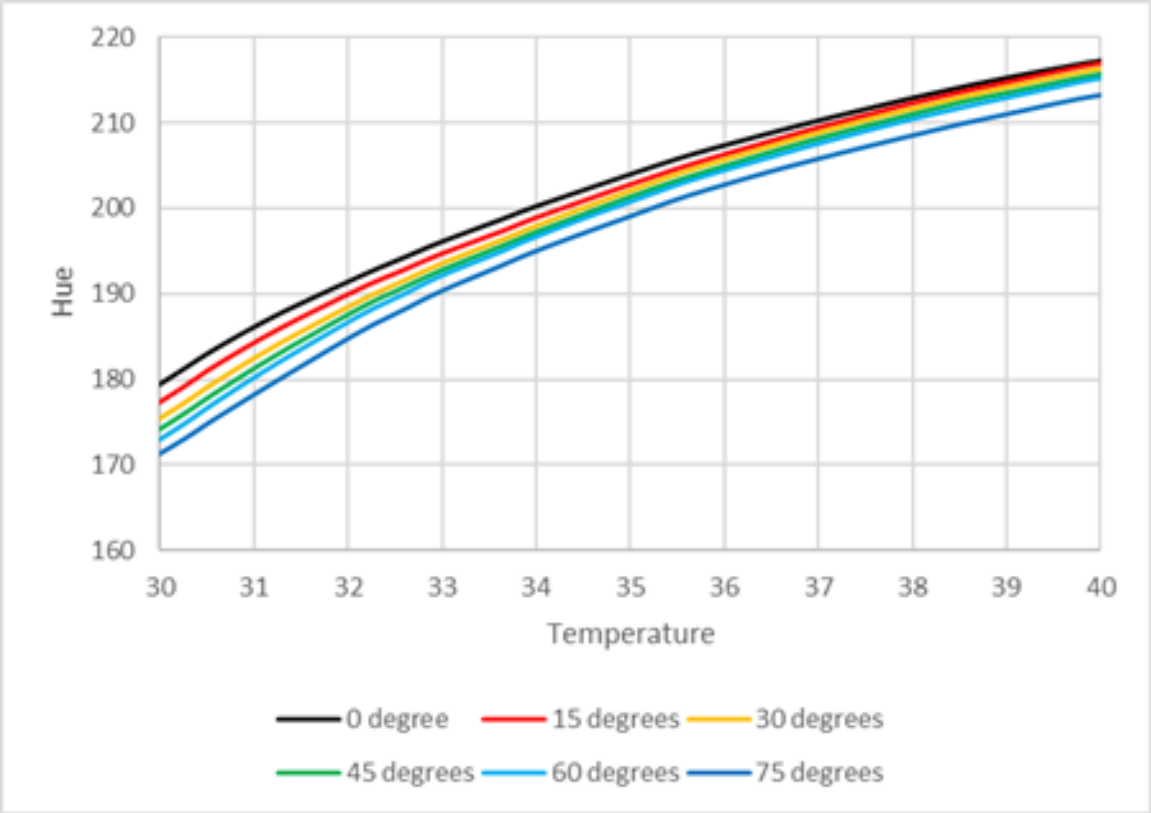

Figure 51 Liquid crystal calibration curves.

Figure 52 shows coolant temperature during the experiment from 0 min to 40 min, measured by five thermocouples Tc_1 to Tc_5. It is found that from Tc_1 to Tc_5, the temperature decreases. The temperatures recorded by Tc_1 to Tc_3 are about the same, which is higher than Tc_4 and Tc_5, because in the plenum from Tc_3 to Tc_5 the coolant flow rate decreases a lot. From 20 min to 40 min, the coolant temperature increases about 1 degree. The reason is that the room temperature and also the mainstream temperature increases during the running of wind tunnel.

Figure 56 shows mainstream temperature during the experiment from 0 min to 40 min, measured by 4 thermocouples. The mainstream temperature increases as the room temperature increases. The wind tunnel is a suction type low speed wind tunnel, and the inlet mainstream is from the room.

Figure 54 and Figure 55 show the calculated overall effectiveness at different time for the normal jet and tangential jet at M = 0.77, 1.54, and 2.31. It is observed that the overall effectiveness is almost the same and reaches the steady state after about 10 min to 20 min.

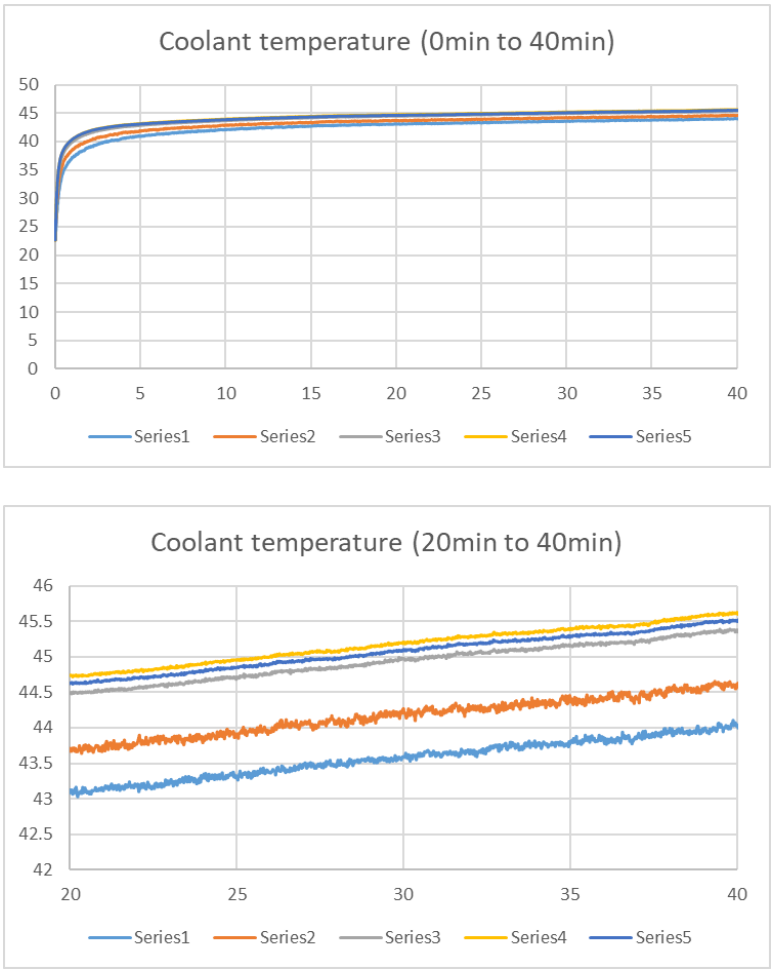

Figure 52 Coolant temperature as functions of time.

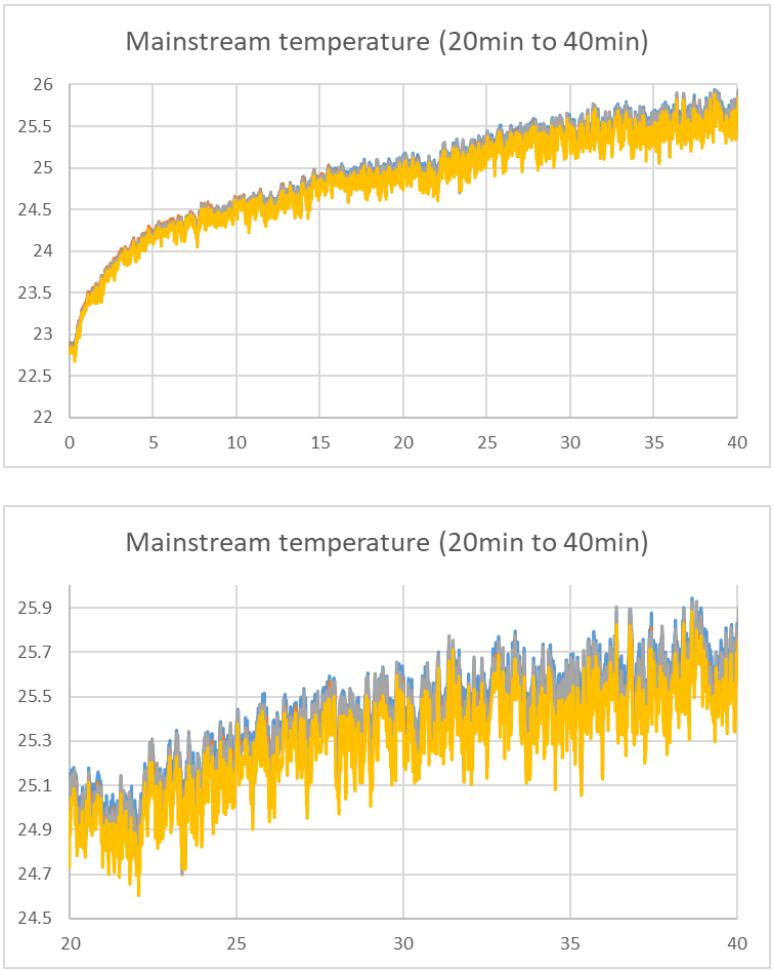

Figure 53 Mainstream temperature as functions of time.

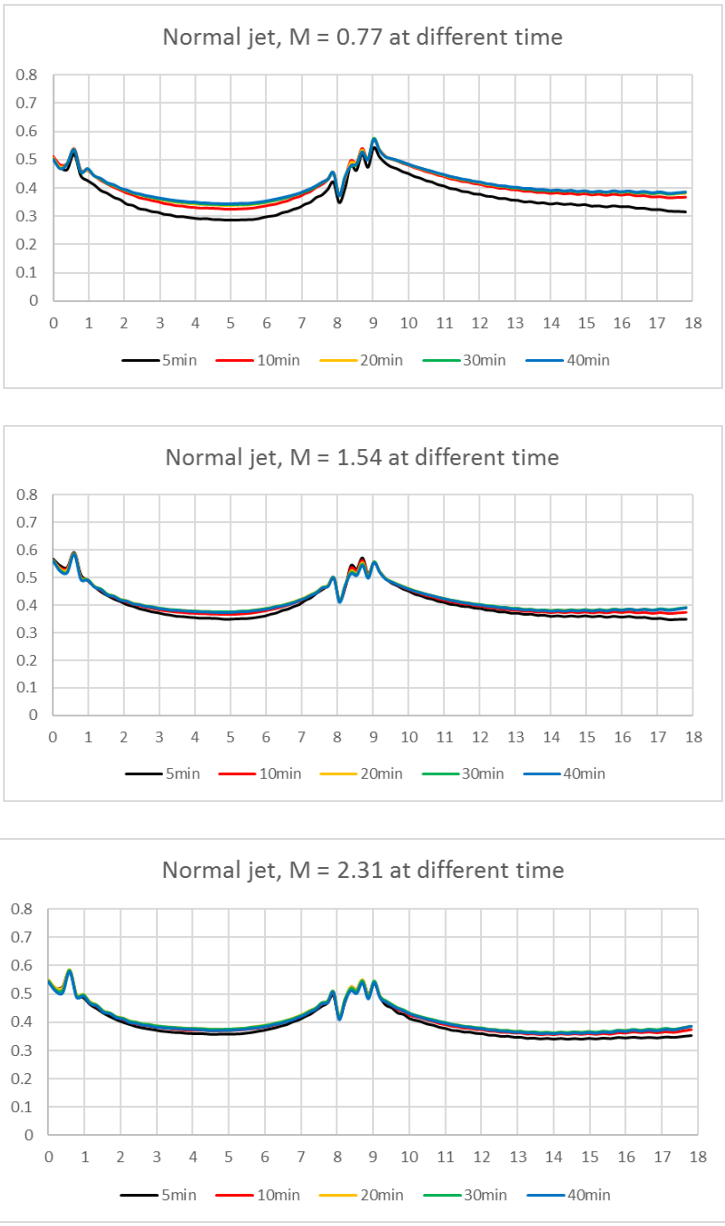

Figure 54 Span-wise averaged overall effectiveness at different time for the normal jet.

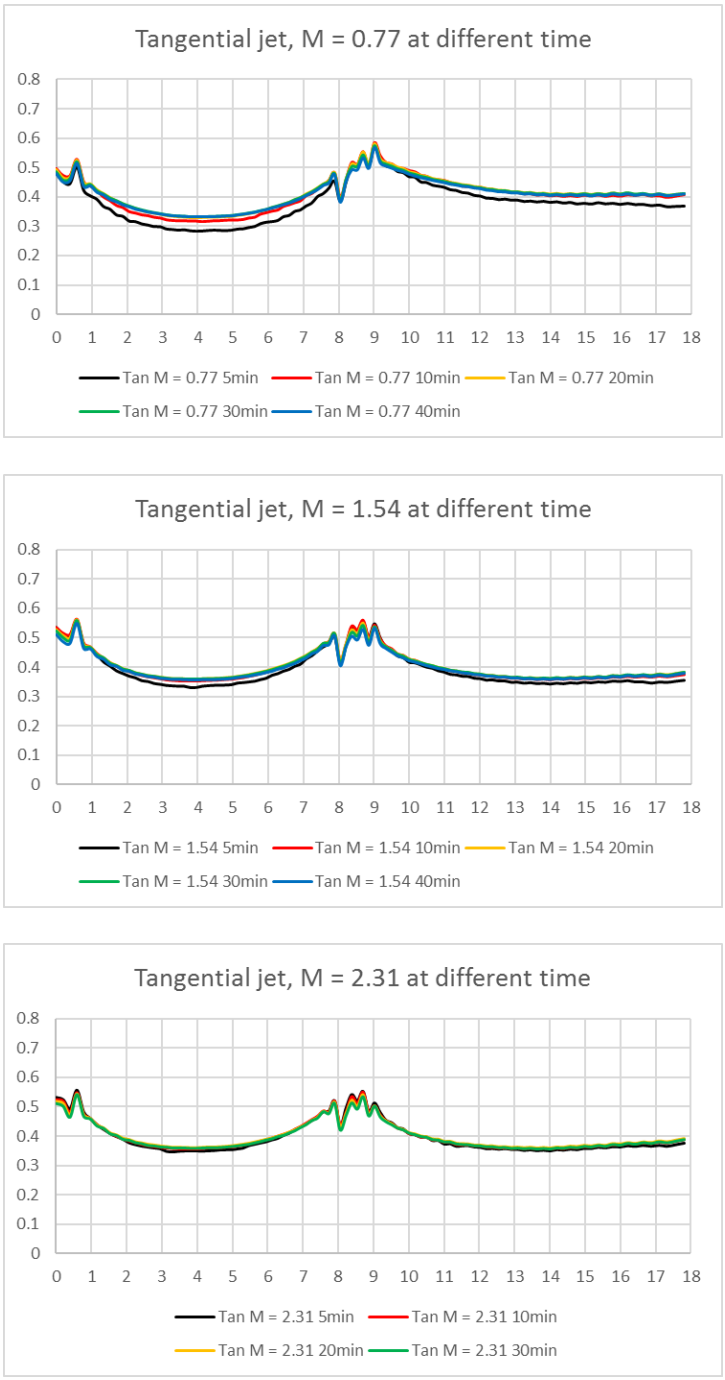

Figure 55 Span-wise averaged overall effectiveness at different time for the tangential jet.

Pressure sensitive paint (PSP) technique is used to obtain the adiabatic effectiveness. PSP is made of luminescent molecules embedded in an oxygen-permeable polymer binder. The luminescent molecules will emit fluorescent light when it relaxes from the excited state to the ground state, excitated by a light source,. The emitted light intensity is inversely proportional to the partial pressure of oxygen on the painted surface. The paint used in this study was UniFIB UF470-750 from ISSI Inc. As shown in Figure 2, a LED light was used to excite the luminescent molecules in the paint, which emits fluorescent light with the wavelength larger than 600 nm. A Cooke Sensicam CCD camera with a long pass filter was used to capture the paint emission intensity. In the experiments, the coolant temperature and the mainstream temperature is the same. Calibration was performed to obtain the relationship between the PSP emission intensity and the oxygen partial pressure. Nitrogen is selected to obtain the coolant to mainstream density ratio 0.97.

Based on mass transfer analogy, the adiabatic effectiveness can be calculated as:

$$\eta = \frac{T_m - T_{aw}}{T_m - T_{c_{out}}} \approx \frac{C_{O_2,fg} - C_{O_2,air}}{C_{O_2,c} - C_{O_2,air}} = 1 - \frac{C_{O_2,fg}}{C_{O_2,air}} = 1 - \frac{1}{\left[1 + \left(\frac{P_{O_2,air}/P_{O_2,ref}}{P_{O_2,fg}/P_{O_2,ref}} - 1\right)\frac{W_{fg}}{W_{air}}\right]} \quad (4.2)$$

, where $C_{O2,c}$ is the oxygen concentration inside film cooling holes, $C_{O2,air}$ and $P_{O2,air}$ are the oxygen concentration and partial pressure with air injection, $C_{O2,fg}$ and $P_{O2,fg}$ are the oxygen concentration and partial pressure with foreign gas injection, W_{air} is the molecular weight of air, and W_{fg} is the molecular weight of the foreign gas.

The uncertainty of the coolant flow rate is about 1.5%. The uncertainty of jet inlet temperature measured by thermocouples is about 2%. The uncertainty of experimental time

reading is about 2%, According to the method proposed by Kline and McClintock [24], the overall uncertainty in heat transfer coefficient calculations is estimated at 7%.

4.2 Numerical Setup and Method

Numerical simulations were done using ANSYS FLUENT 18.2. Grids including unstructured meshes and structured meshes were generated using ICEM CFD. Unstructured meshes are generated near the leading edge model and structured meshes are generated away from the leading edge to simulate the wind tunnel. There are 20 prism layers near the walls of leading edge and cooling holes, with $y+ \leq 1$. The total number of meshes was about 18 million (16 million unstructured meshes and 2 million structured meshes). Mesh interface is used between the two types of meshes. The height and width of the wind tunnel are 25.4 cm and 76.2 cm, respectively. The mainstream inlet is located 38.1 cm in front of the stagnation line of leading edge. Figure 56 shows the schematic of the computational meshes near the leading edge for the normal jet. Boundary conditions are summarized in Table 7. Adiabatic wall boundary conditions are used to calculate the adiabatic effectiveness. Coupled wall boundary conditions are applied between the fluid zone and solid zone to calculate the overall effectiveness. Calculations were assumed converged when the residuals were in order 10^{-8} for energy, in order 10^{-5} for the continuity equation, and in order 10^{-6} for all other residuals.

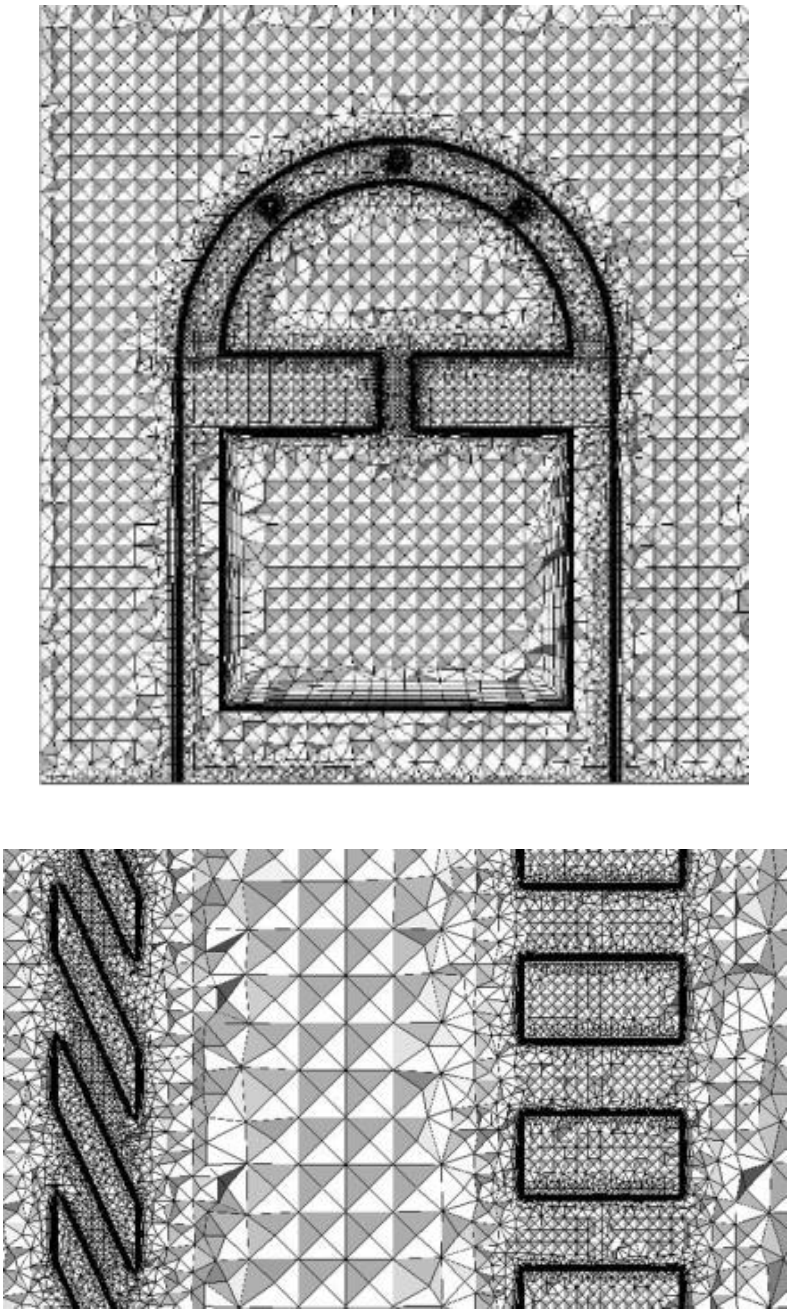

Figure 56 Schematic of computational domain for the normal jet.

Table 7 CFD boundary conditions.

Mainstream velocity (m/s)	20.89 m/s
Mainstream turbulence intensity	7%
Mainstream temperature	298K
T_c for adiabatic effectiveness	307.2K
T_c for overall effectiveness	318K

Based on one dimensional conjugate heat transfer analysis, the heat flux can be expressed as

$$q = h_f\,(T_{aw} - T_w) = \frac{\left(T_{aw} - T_{c_{in}}\right)}{\frac{1}{h_f} + \frac{t}{K} + \frac{1}{h_i}}, \tag{4.3}$$

Then we can obtain that

$$\phi = \frac{T_m - T_w}{T_m - T_{c_{in}}} = \frac{1 - \chi\eta}{1 + Bi + \frac{h_f}{h_i}} + \chi\eta, \tag{4.4}$$

$$Bi = \frac{h_f t}{K}, \chi = \frac{T_m - T_{c_{out}}}{T_m - T_{c_{in}}},$$

$$\eta = \frac{T_m - T_{aw}}{T_m - T_{c_{out}}}$$

Here, Bi is the Biot number, h_f is the external heat transfer coefficient, h_i is the internal heat transfer coefficient, t is the leading edge thickness, K is the leading edge material thermal

conductivity. Based on CFD results, we estimated the averaged values of h_f/h_i and *Bi* as shown in Table 8.

Table 8 Averaged h_f/h_i and *Bi* for the normal jet and tangential jet.

	Normal Jet			Tangential Jet		
M	0.77	1.54	2.31	0.77	1.54	2.31
Bi	1.27	1.47	1.67	1.29	1.49	1.70
h_f/h_i	2.16	1.50	1.28	1.70	1.23	1.03

4.3 Experimental Results and Discussion

In this section, adiabatic effectiveness and overall effectiveness at three blowing ratios M = 0.77, 1.54 and 2.31 are discussed. Results are shown by effectiveness contours, span-wise averaged effectiveness and stream-wise averaged effectiveness.

4.3.1 Adiabatic effectiveness contours - experiments

Detailed adiabatic effectiveness contours at M = 0.77 and 1.54 are presented in Figure 57. It is observed that, in the stagnation region, the adiabatic effectiveness decreases quickly. It is because the coolant penetrates into the mainstream where the mainstream velocity is low in this region. After the second film cooling row, when M increases from 0.77 to 1.54, the coolant trail becomes thinner and the adiabatic effectiveness decreases a lot. It is due to the coolant lifted off instead of attaching to the leading edge surface at high M.

4.3.2 Averaged adiabatic effectiveness - experiments

Figure 58 shows the span-wise averaged adiabatic effectiveness at M = 0.77 and 1.54. Results show that the impinging jet hole positions have a similar effect on the span-wise averaged adiabatic effectiveness, with the tangential jets higher than the normal jets. Near film cooling rows, the adiabatic effectiveness is the highest. The values are about 0.1 to 0.2 between the stagnation row and the second row ($1 < s/d < 7$). When M increases from 0.77 to 1.54, the adiabatic effectiveness decreases a lot after the second row. The values are about 0.3 to 0.2 at M = 0.77, and about 0.2 to 0.14 at M = 1.54.

Figure 59 shows the stream-wise averaged adiabatic effectiveness. Here, data around the film cooling holes are not used in calculating averaged effectiveness. At M = 0.77, values are in the range about 0.1 to 0.3. The variation in adiabatic effectiveness decreases when M increases. At M = 1.54, values are in the range about 0.14 to 0.22.

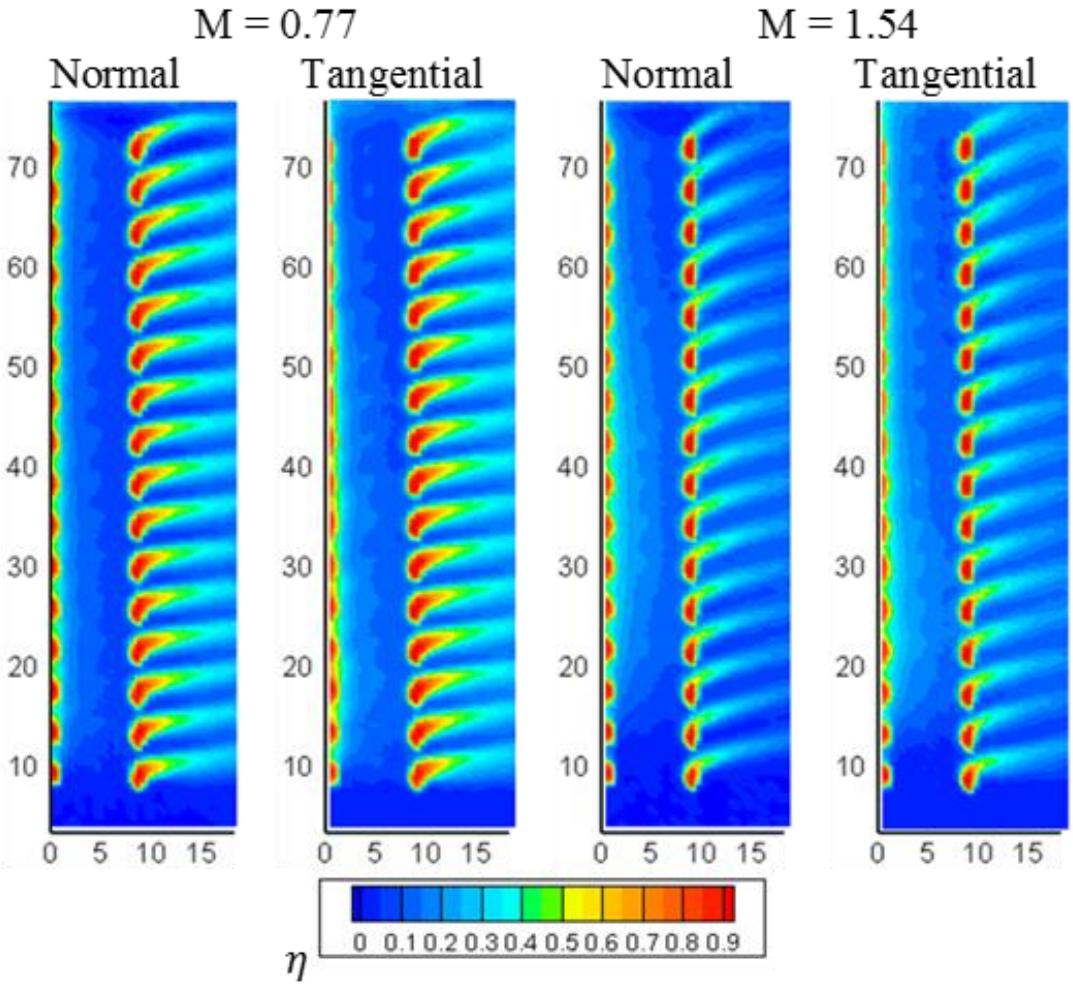

Figure 57 Adiabatic effectiveness contours.

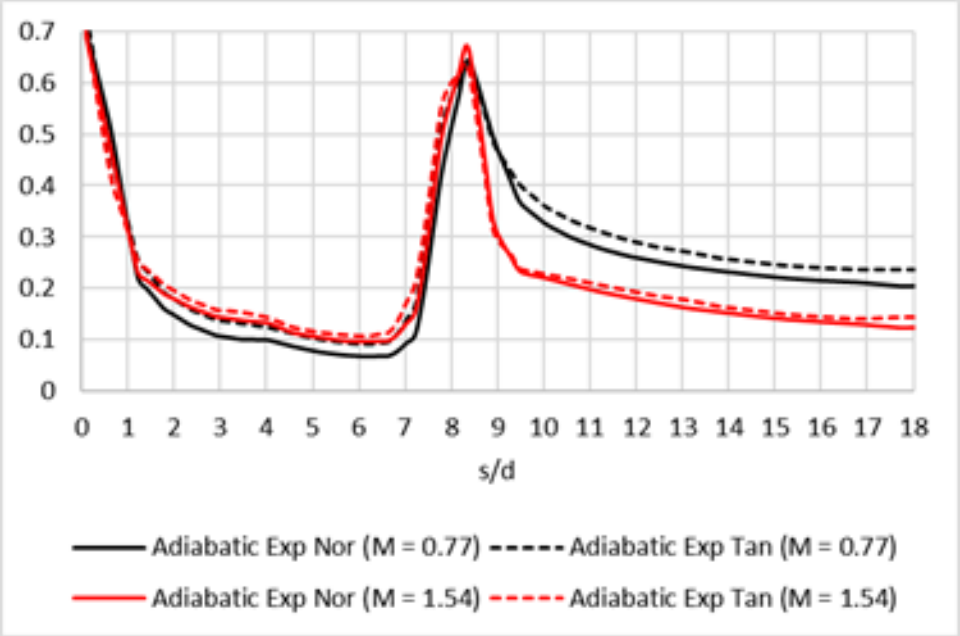

Figure 58 Span-wise averaged adiabatic effectiveness.

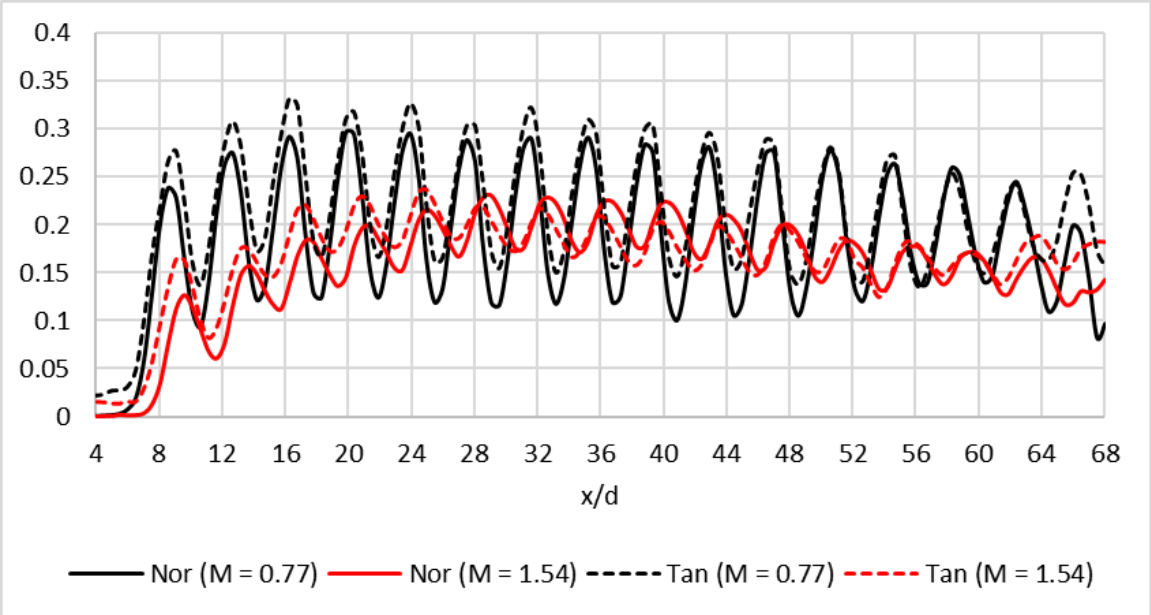

Figure 59 Stream-wise averaged adiabatic effectiveness.

4.3.3 Overall effectiveness contours - experiments

Detailed overall effectiveness contours are presented in Figure 60. High value is observed near film cooling holes. Compared with adiabatic effectiveness, overall effectiveness near the film cooling holes reduces due to conduction effect. It is observed that before the second row, overall effectiveness is about the same at a given s/d. Compared results between the normal jet and the tangential jet, before the second row, the normal jet is higher than the tangential jet; after the second row, the normal jet is also higher than the tangential jet at high blowing ratio M = 1.54 and 2.31.

4.3.4 Averaged overall effectiveness - experiments

Figure 61 shows the span-wise averaged overall effectiveness. Before the second row, overall effectiveness at M = 1.54 and 2.31 is about the same, which is higher than effectiveness at M = 0.77. After the second row, the overall effectiveness decreases as M increases. It is because, after the second row, the adiabatic effectiveness decreases a lot as M increases.

Figure 62 shows the comparison of span-wise averaged overall effectiveness for different blowing ratio M. Before the second row, overall effectiveness at M = 1.54 and 2.31 is about the same, which is higher than effectiveness at M = 0.77. After the second row, overall effectiveness decreases as M increases. It is found that, for the tangential jet, overall effectiveness decreases a lot from M = 0.77 to 1.54, as adiabatic effectiveness decreases a lot.

Figure 63 shows the stream-wise averaged overall effectiveness. Here, data around the film cooling holes are not used in calculating averaged overall effectiveness. Overall effectiveness is periodical in the middle portion with the value around 0.4. At M = 0.77, the normal jet and the

tangential jet is about the same. At M = 1.54 and 2.31, the normal jet is higher than the tangential jet.

Figure 64 shows the comparison of span-wise averaged adiabatic effectiveness and overall effectiveness. It is found that the overall effectiveness is higher than the adiabatic effectiveness. After the second row, the difference of adiabatic effectiveness for different M is higher than the difference of overall effectiveness for different M.

Figure 65 presents the comparison of stream-wise averaged adiabatic effectiveness and overall effectiveness. The overall effectiveness is more uniform than the adiabatic effectiveness due to conduction effect, especially at low blowing ratio M = 0.77.

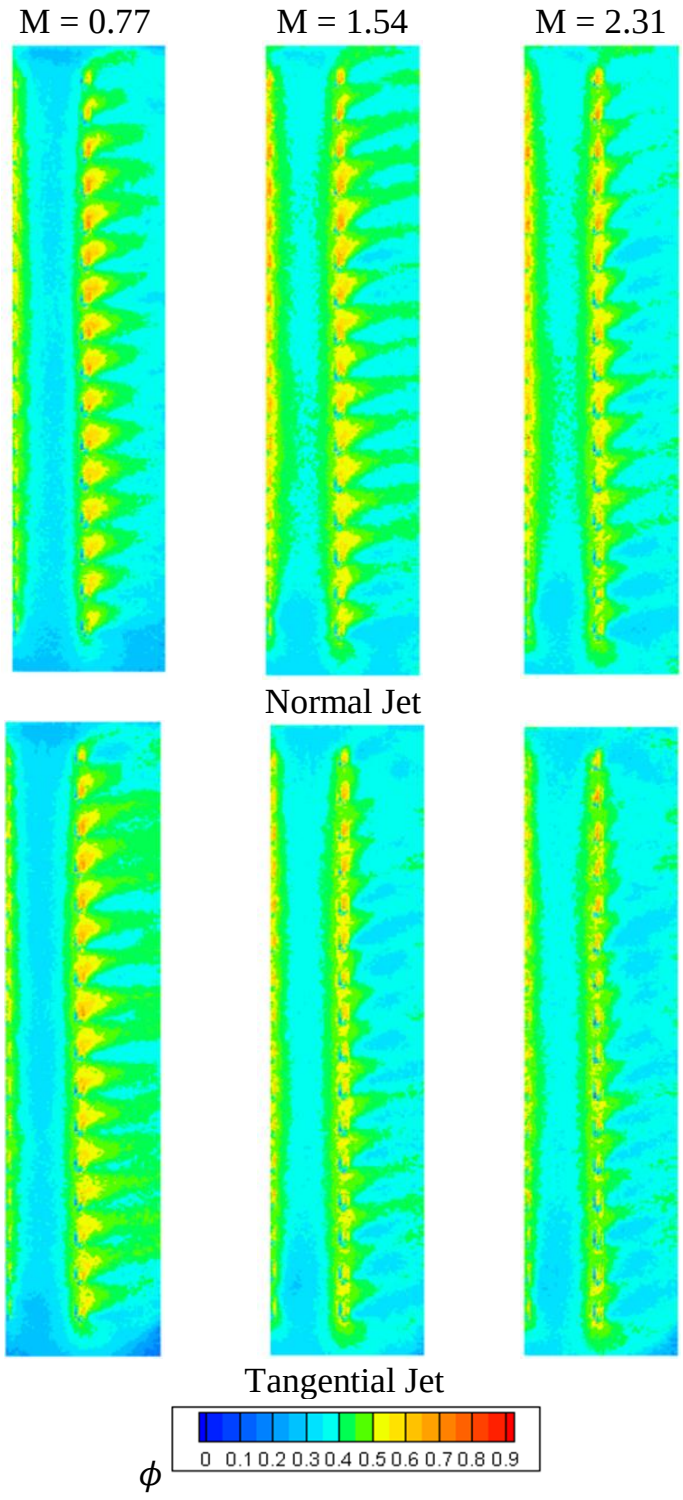

Figure 60 Overall effectiveness contours.

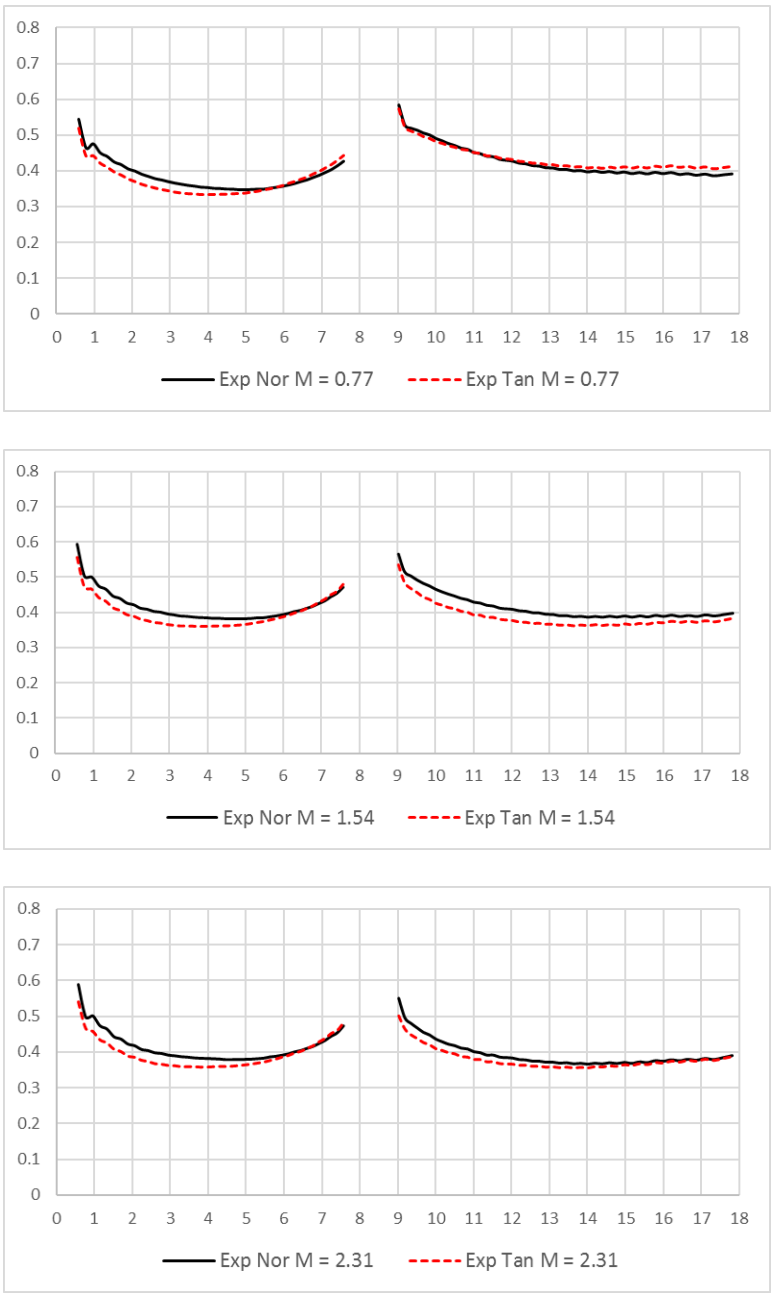

Figure 61 Span-wise averaged overall effectiveness.

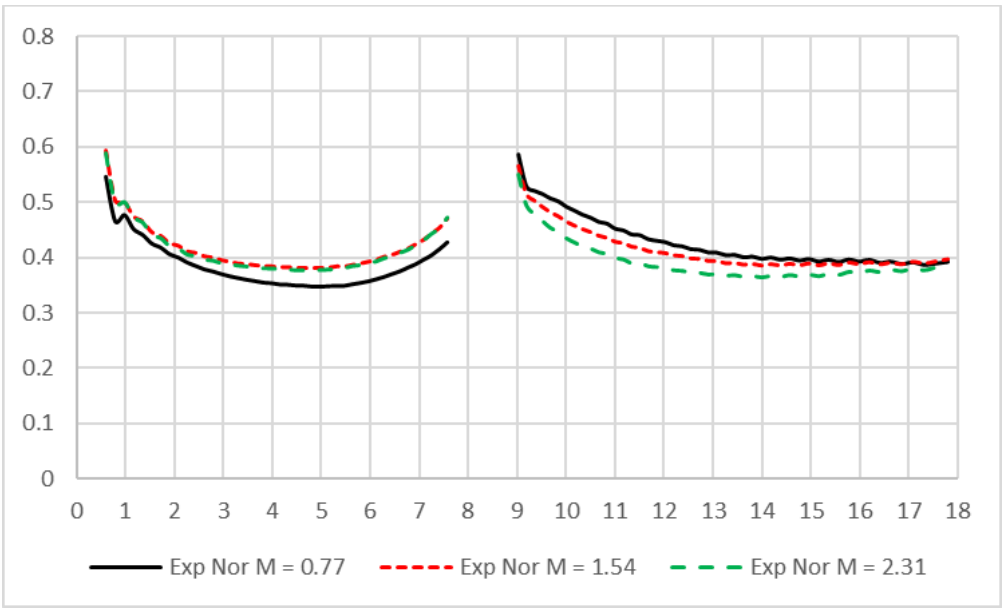

Normal Jet

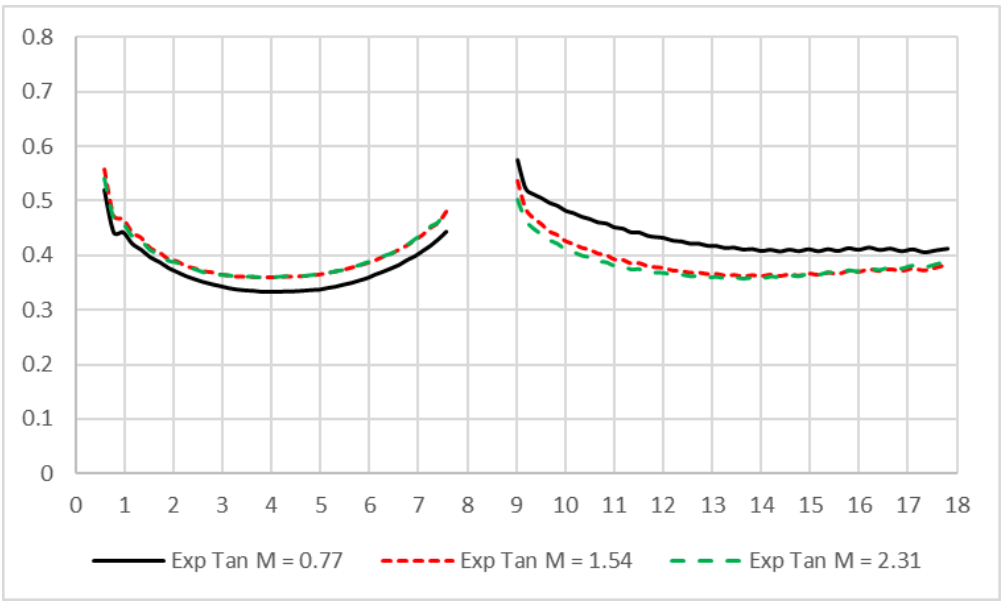

Tangential Jet

Figure 62 Span-wise averaged overall effectiveness.

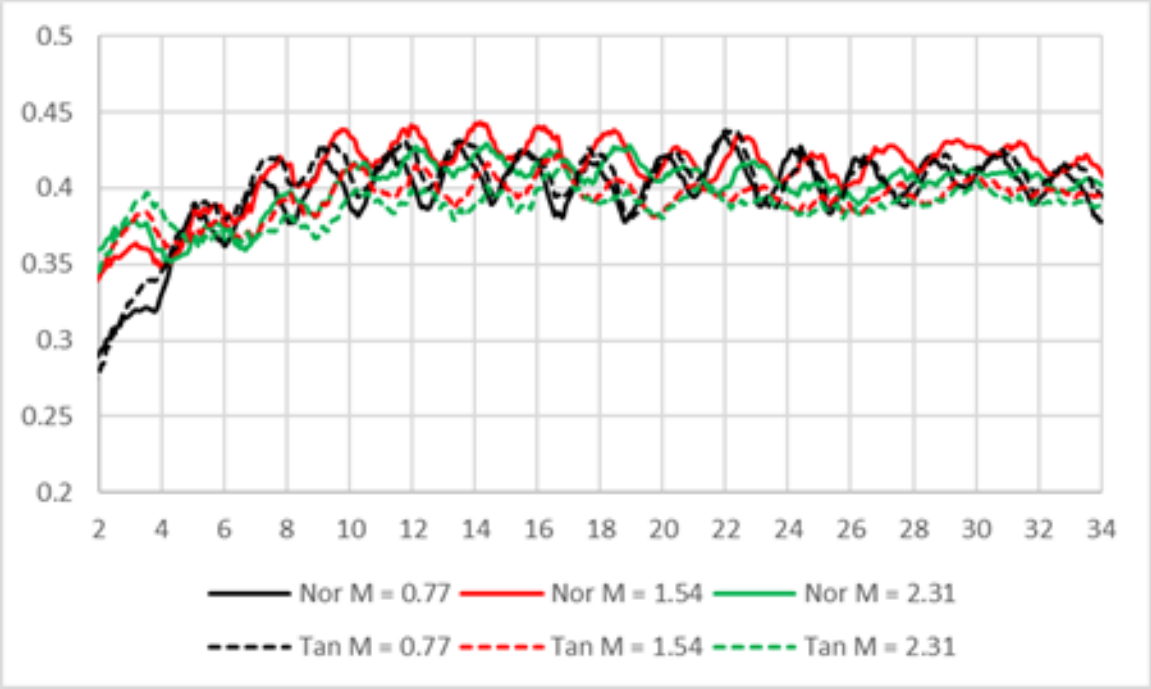

Figure 63 Stream-wise averaged overall effectiveness.

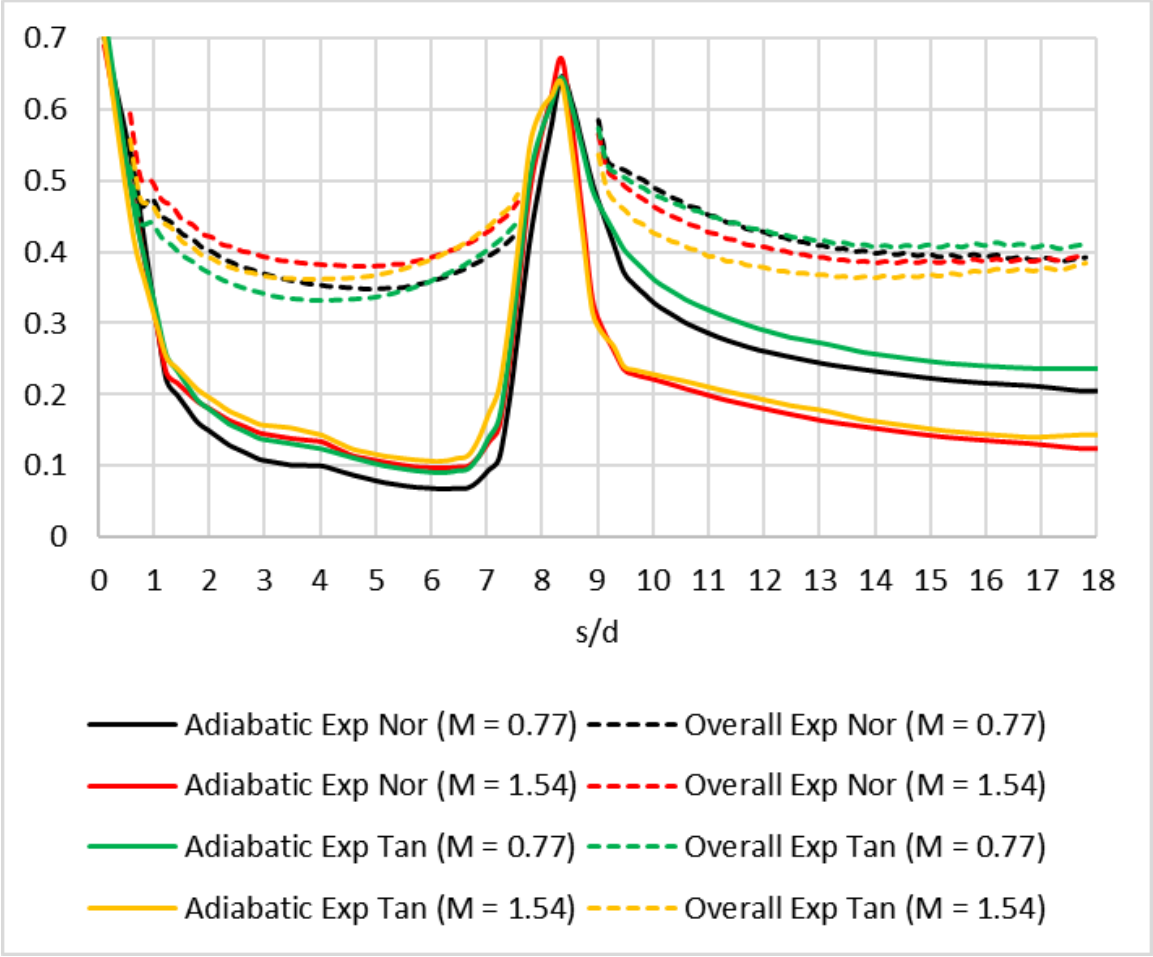

Figure 64 Comparison between measured adiabatic effectiveness and overall effectiveness.

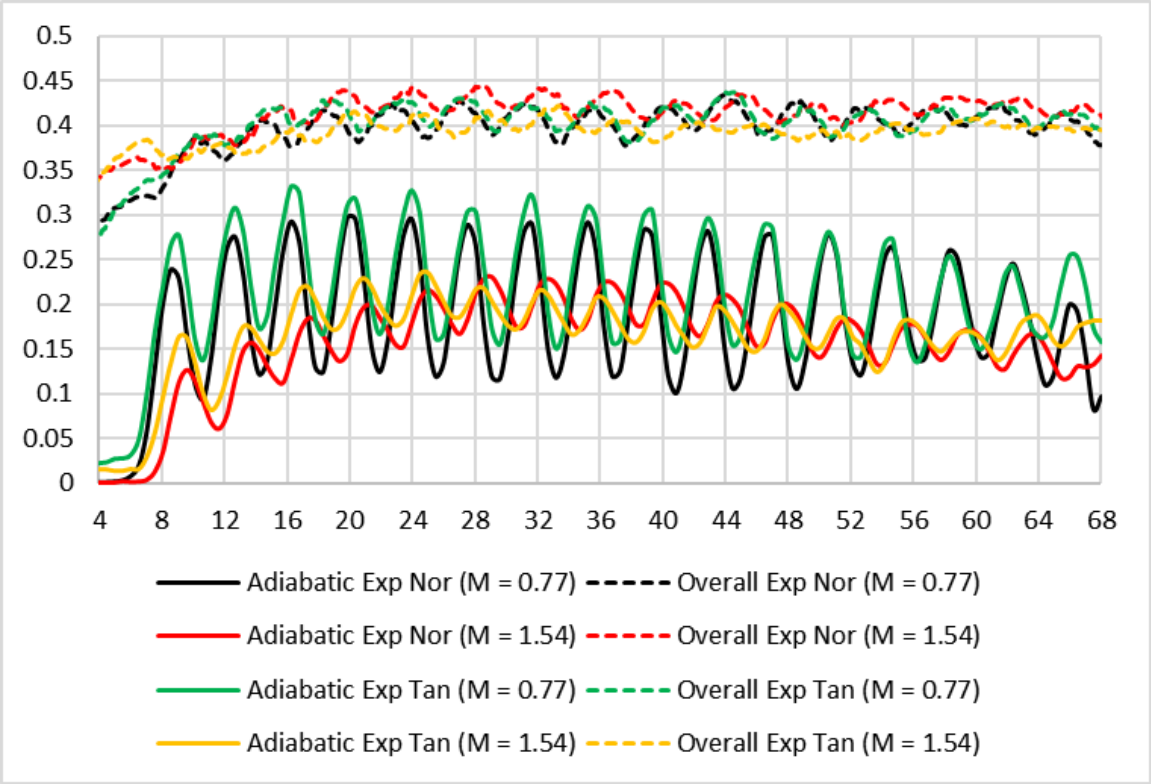

Figure 65 Comparison between measured adiabatic effectiveness and overall effectiveness.

4.4 Numerical Results and Discussion

In this section, Numerical simulations using RKE model are carried out. Results are shown by velocity magnitude contours and streamlines, followed by adiabatic effectiveness and overall effectiveness.

4.4.1 Velocity contours and streamlines - simulations

Velocity magnitude contours and streamlines are presented in Figure 66. Local mainstream velocity increases from the stagnation line to the downstream. Note that for the tangential jet, the cut plane is in the middle of the left row of the tangential jet, and the velocity contour and flow pattern will reverse when the cut plane is in the middle of the right row.

It is found that the flow structure in the half cylinder is different for the two designs. For the normal jet, there are two symmetric vortexes in the leading edge cut plane. For the tangential jet, the two vortexes are not symmetry. One vortex is located near the second (40^o) row in the same side of the tangential jet, which is generated by the interaction between the left side tangential jet and the reverse flow from the right side tangential jet. The other vortex is located between the second row and the impingement plate on the opposite side of the tangential jet.

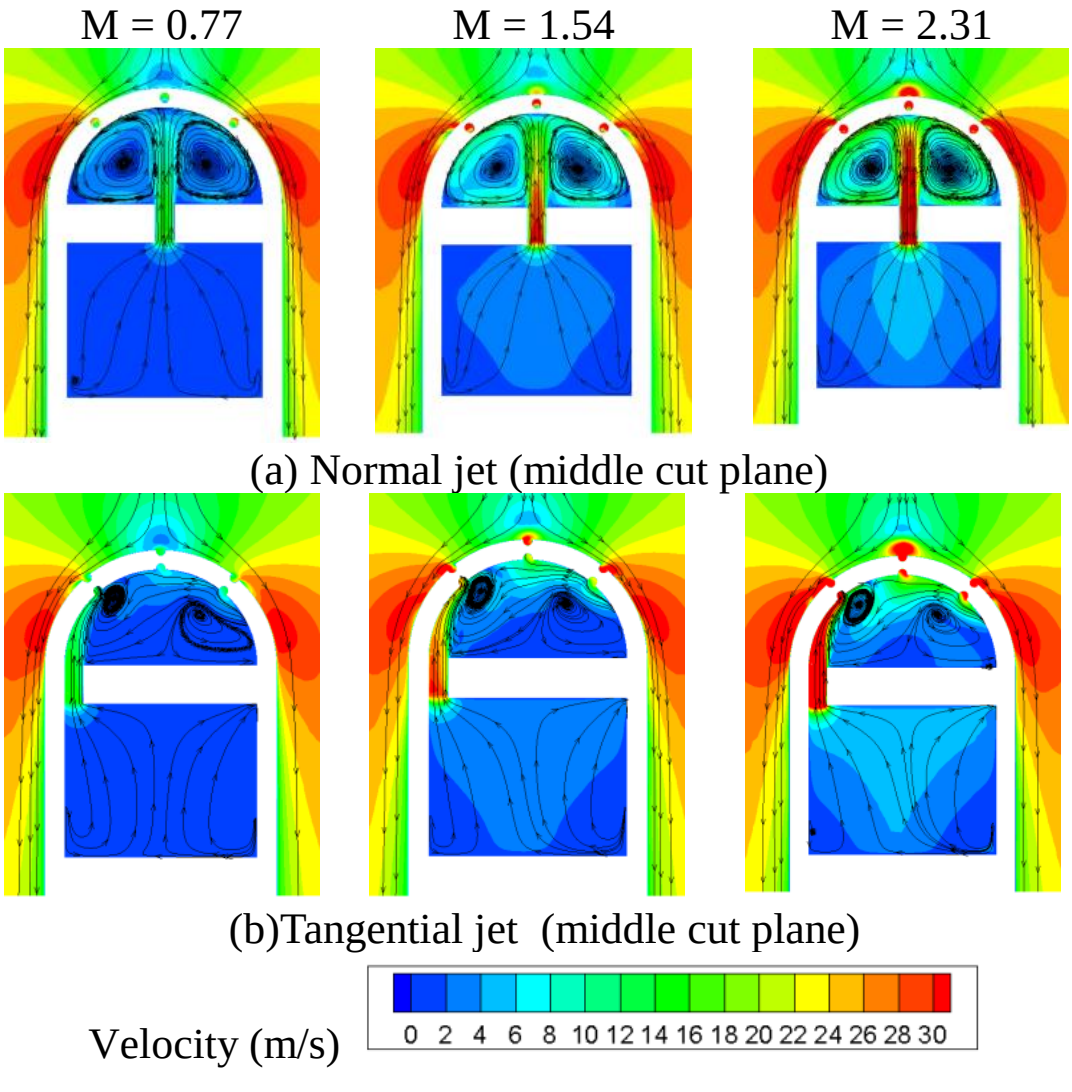

Figure 66 Velocity magnitude contours and streamlines.

4.4.2 Blowing ratio distribution - simulations

Using the coolant mass flow rates from each film cooling rows obtained by RKE and the wind tunnel mainstream velocity, we can calculate the local blowing ratios from each row. The local blowing ratio is about 0.5, 1.3 and 2.1 in the stagnation row and about 0.9, 1.6 and 2.4 in the second row for M = 0.77, 1.54 and 2.31 respectively. Note that local blowing ratio for the normal jet and the tangential jet is about the same.

4.4.3 Adiabatic effectiveness contours - simulations

Detailed adiabatic effectiveness contours by simulations at DR = 0.97, M = 0.77 and 1.54 are presented in Figure 67 and Figure 68. Compared with experimental results, simulations overpredict values before the second row. After the second row, contours by simulations are similar with experiments.

4.4.4 Averaged adiabatic effectiveness - simulations

Figure 69 shows the comparison of span-wise averaged adiabatic effectiveness between experiments and CFD simulations. Before the second row, CFD overpredicts the adiabatic effectiveness. After the second row, CFD predicts well at M = 0.77, but overpredict at M = 1.54. The reason CFD overpredicts the adiabatic effectiveness should be that CFD underpredicts the jet liftoff at low density ratio DR = 0.97. Figure 70 shows stream-wise averaged adiabatic effectiveness by CFD simulations.

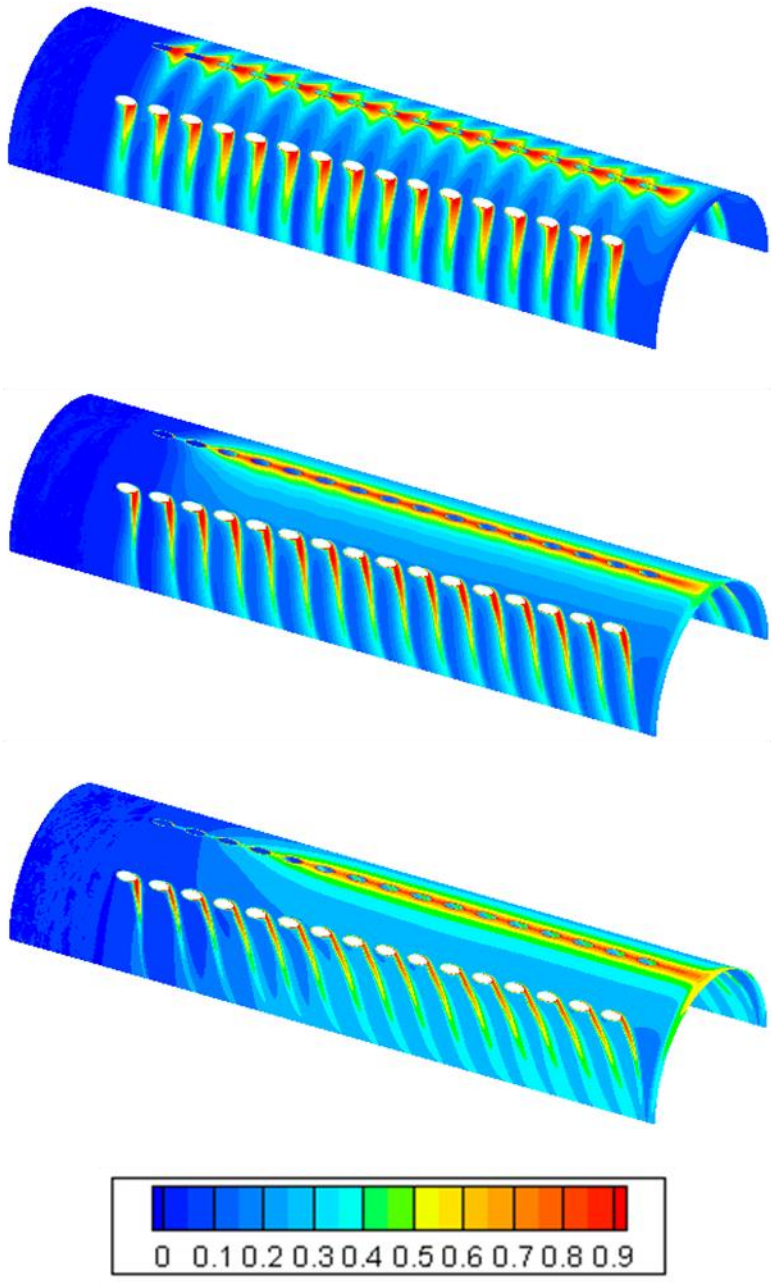

Figure 67 Adiabatic effectiveness contours for the normal jet.

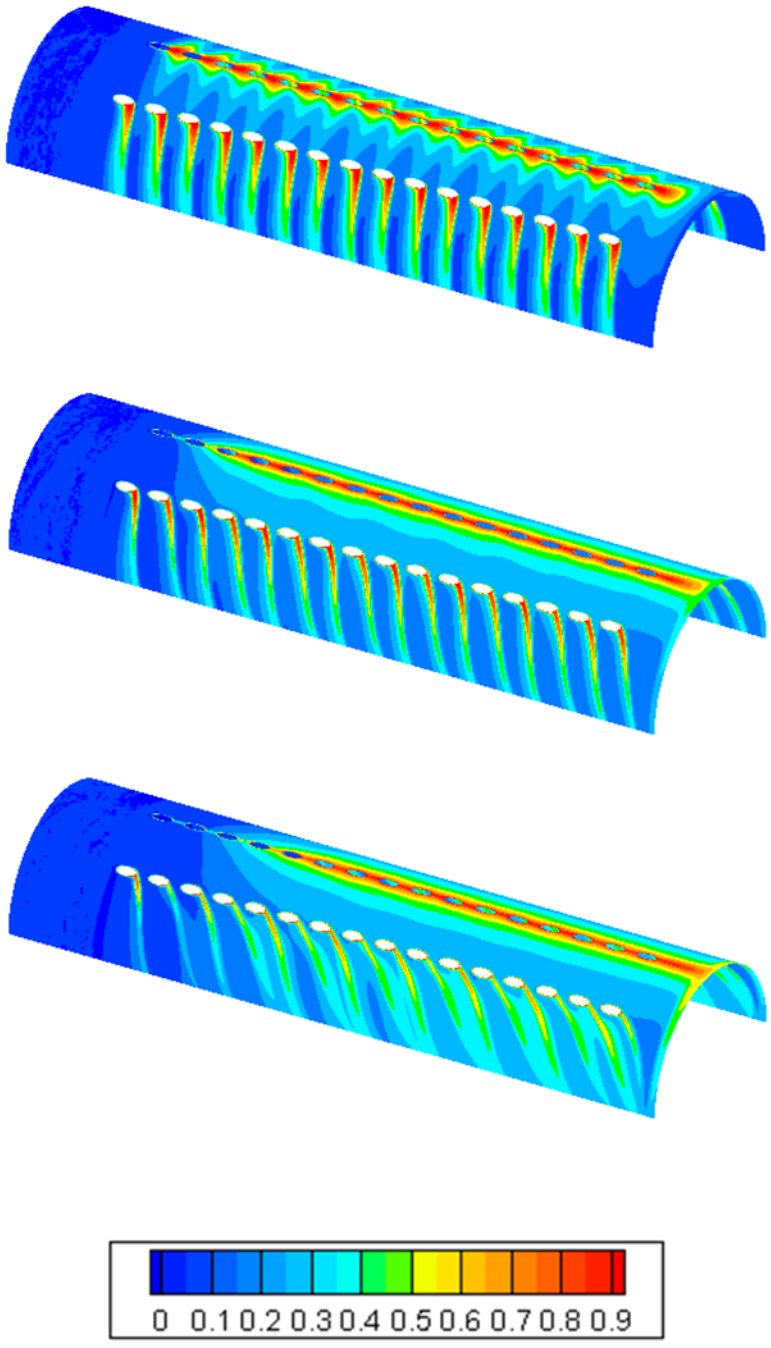

Figure 68 Adiabatic effectiveness contours for the tangential jet.

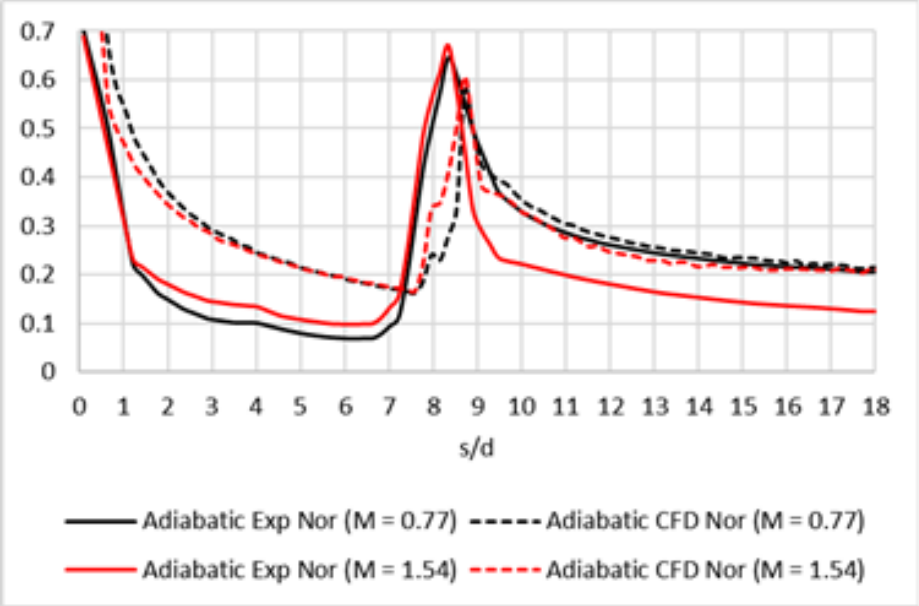

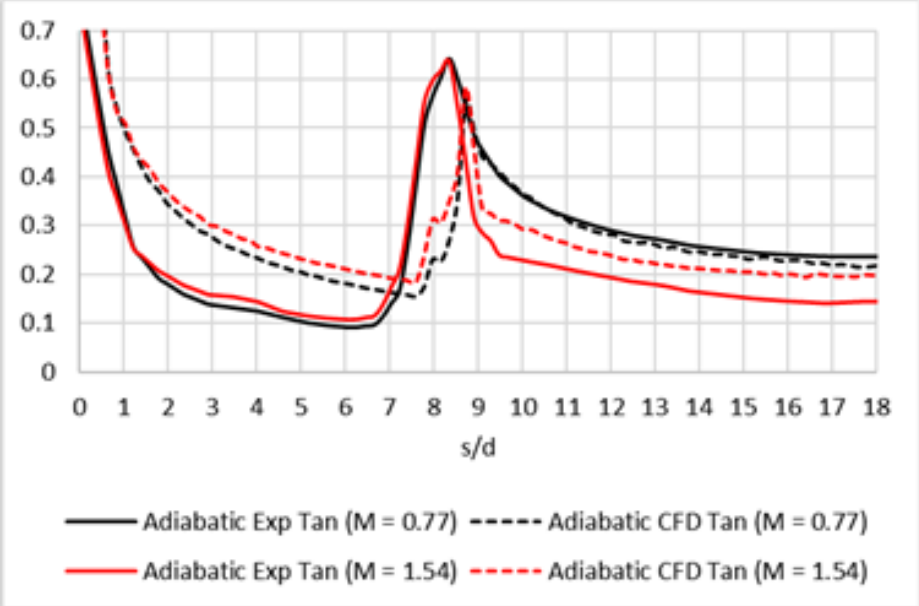

Figure 69 Comparison of span-wise averaged effectiveness between experiments and CFD.

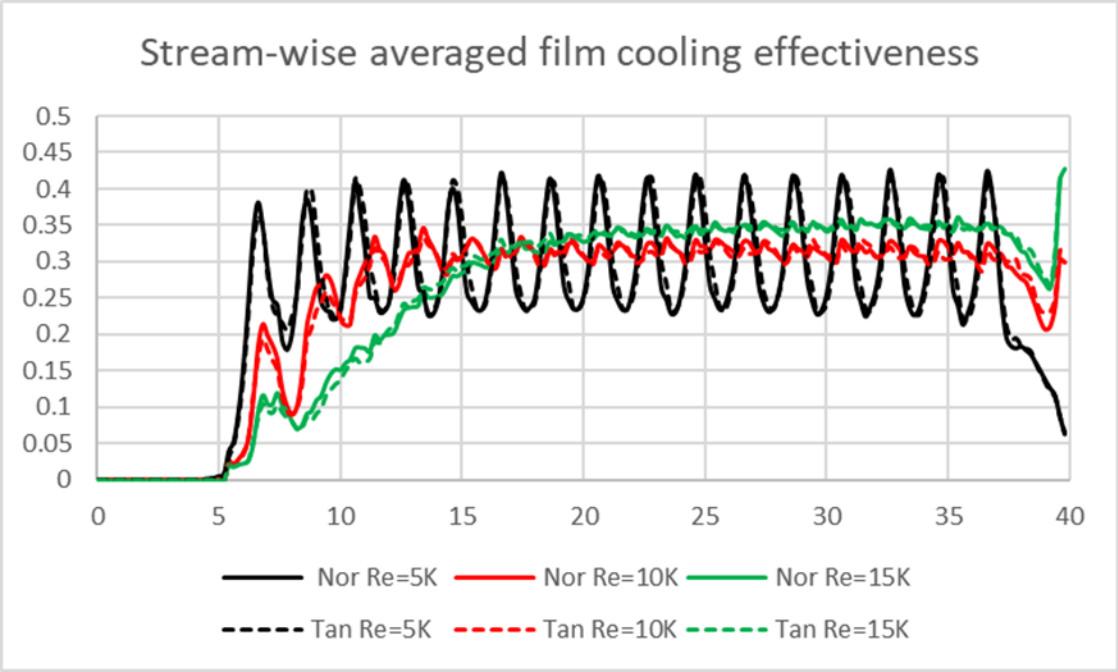

Figure 70 Stream-wise averaged adiabatic effectiveness by CFD.

4.4.5 Overall effectiveness contours - simulations

Figure 71 shows overall effectiveness contour of the whole external surface of the leading edge test section at M = 1.54 for the normal jet. Detailed overall effectiveness contours by simulations are presented in Figure 72 and Figure 73. Compared with experimental results, simulations over predict values before the second row. After the second row, contours by simulations are similar with experiments at M = 0.77 and 1.54; while, at M = 2.31, simulations underpredict overall effectiveness near the hub and overpredict overall effectiveness in the middle and tip.

4.4.6 Averaged overall effectiveness - simulations

Figure 74 shows the comparison of span-wise averaged overall effectiveness between experiments and numerical simulations. Before the second row, simulations overpredict overall effectiveness about 20% to 30%. Over effectiveness at M = 1.54 and 2.31 is about the same, which is higher than effectiveness at M = 0.77. After the second row, the difference between simulations and experiments is about 10% to 20%. However, experimental results show that effectiveness decreases with increasing M; while, numerical results increase as M increases. It may be because CFD underpredict the jet liftoff at high blowing ratios.

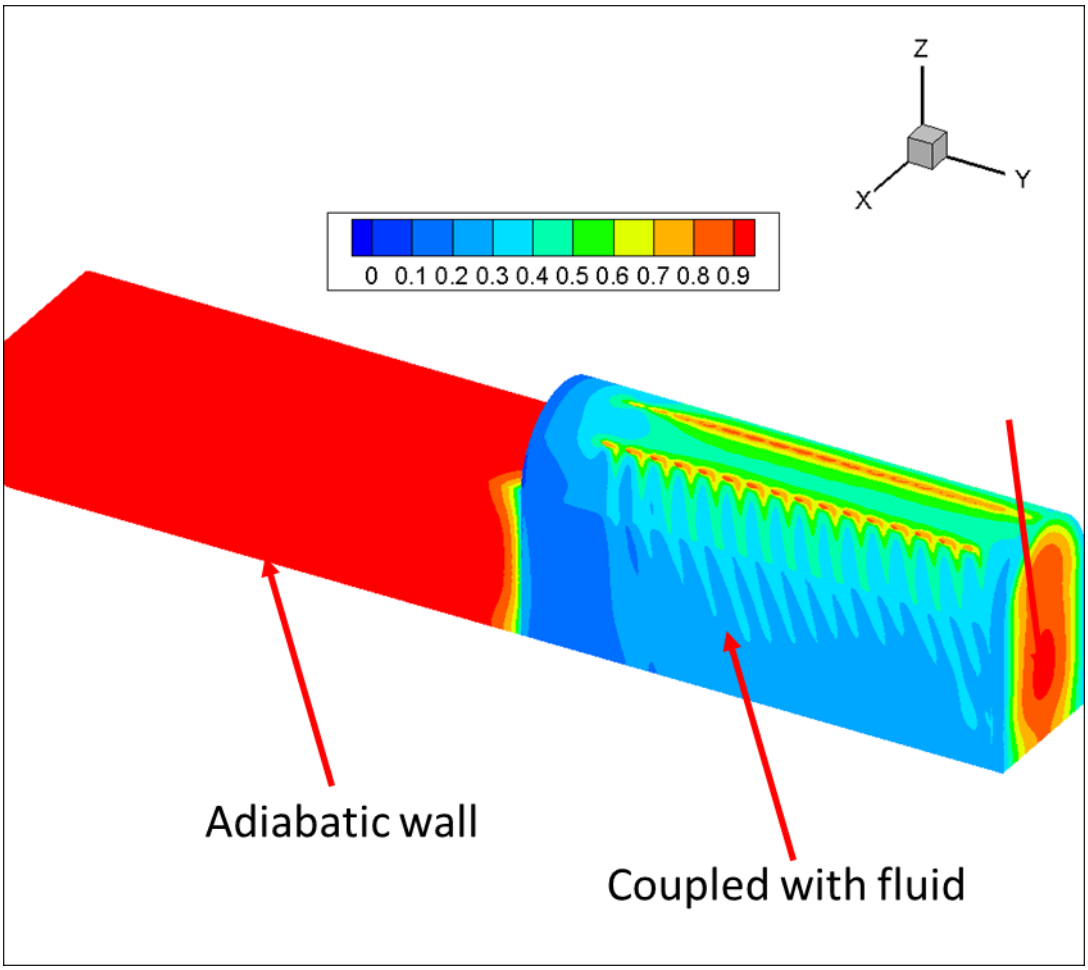

Figure 71 Overall effectiveness contours by simulations at M = 1.54 for the normal jet.

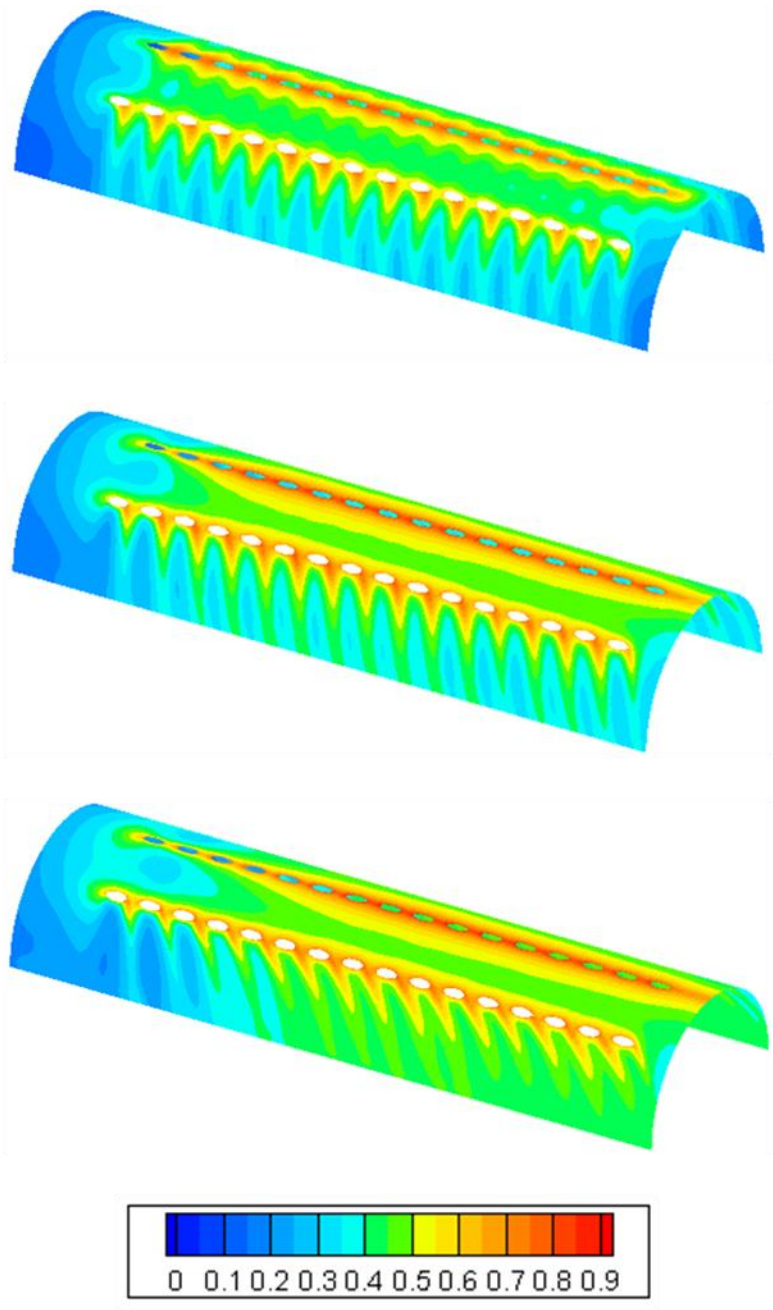

Figure 72 Overall effectiveness contours for the normal jet by simulations.

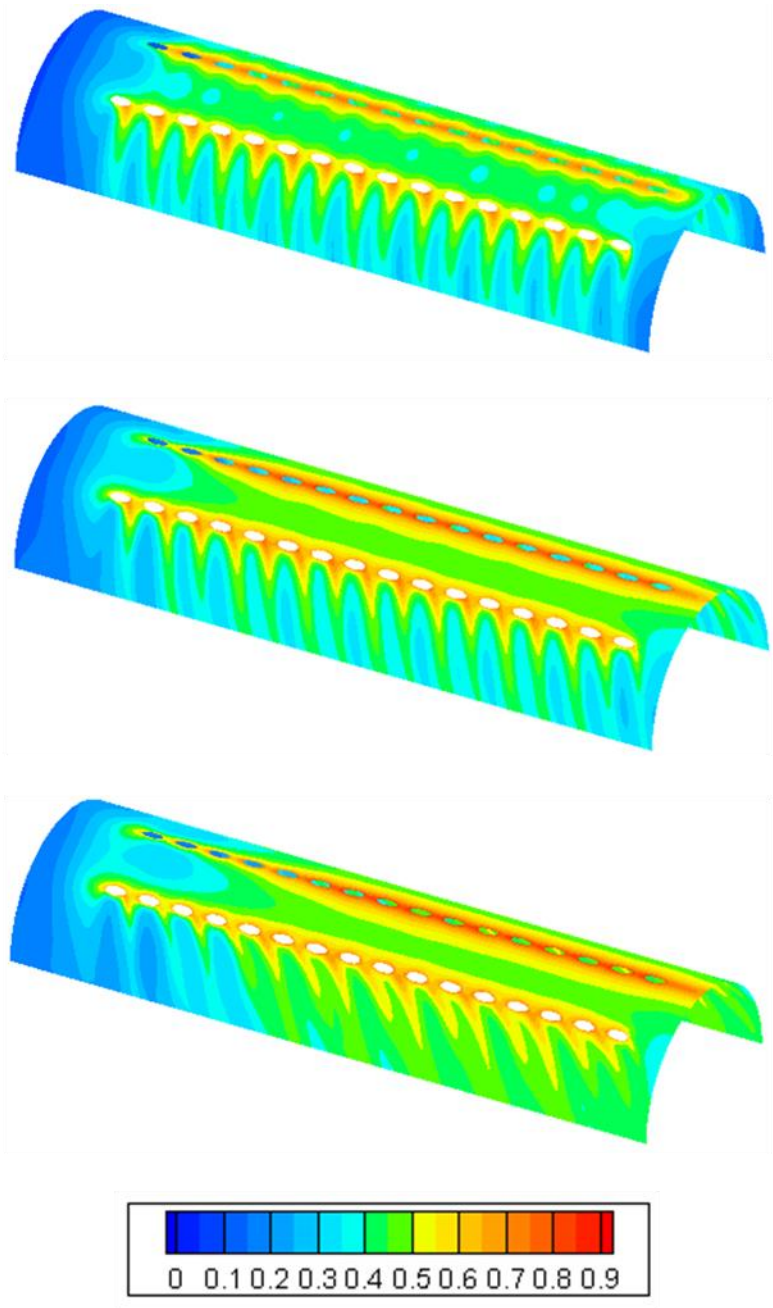

Figure 73 Overall effectiveness contours for the tangential jet by simulations.

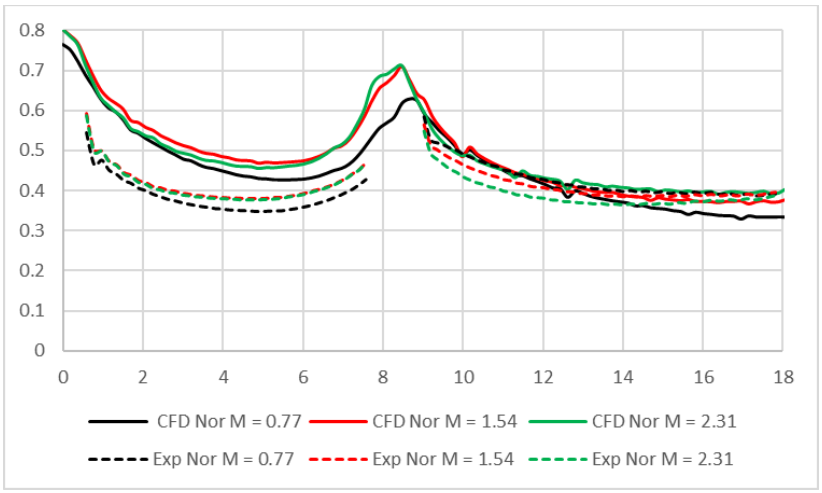

Normal Jet

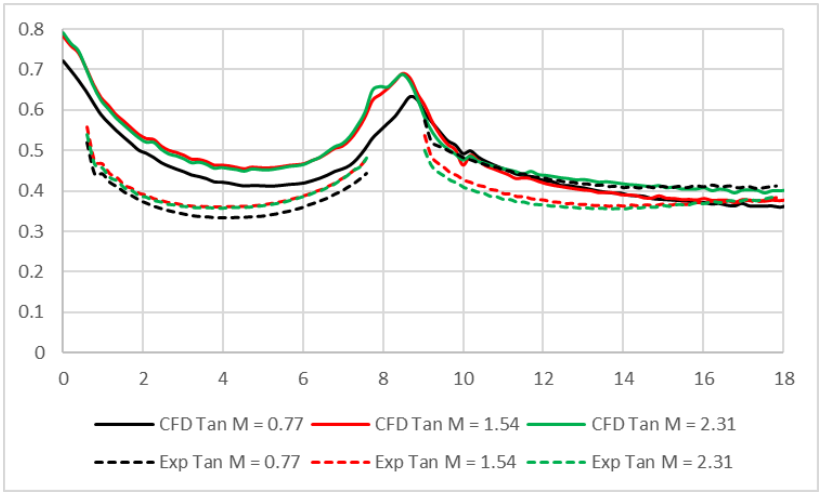

Tangential Jet

Figure 74 Comparison of overall effectiveness between experiments and simulations.

4.5 Conclusions

We studied turbine blade adiabatic and overall cooling effectiveness of a film-cooled leading edge model with normal and tangential impinging jets. The main conclusions are drawn as follows.

Adiabatic effectiveness at M = 0.77 and 1.54 with DR = 0.97 are studied using PSP. The difference between the normal jet and the tangential jet is small. After the second row, increasing blowing ratio M decreases adiabatic effectiveness. Numerical simulations fail to predict the adiabatic effectiveness before the second row. After the second row, numerical simulations agree well at M = 0.77 but overpredict at M = 1.54. The reason should be that RKE model underpredicts the jet liftoff at low density ratio DR = 0.97 and high blowing ratio.

Overall effectiveness at M = 0.77, 1.54 and 2.31 with DR = 0.94 are studied. Before the second row, overall effectiveness at M = 1.54 and 2.31 is about the same, which is higher than the effectiveness at M = 0.77. After the second row, increasing blowing ratio M decreases overall effectiveness. Numerical simulations overpredict overall effectiveness values before the second row about 20% to 30%, and the difference between simulations and experiments is about 10% to 20% after the second row. Compared with adiabatic effectiveness and overall effectiveness for a given impingement design, it is found that the difference of overall effectiveness between M = 0.77 and 1.54 is smaller than the difference of the adiabatic effectiveness.

5. SUMMARY

In this study, we investigated three topics: (1) influence of turbine blade leading edge profile on film cooling with shaped holes, (2) internal heat transfer of film-cooled leading edge model with normal and tangential impinging jets, (3) overall effectiveness of film-cooled leading edge model with normal and tangential impinging jets. Pressure sensitive paint (PSP) technique is used to measure the adiabatic effectiveness, transient liquid crystal technique is used to obtain the internal heat transfer coefficient, liquid crystal technique is used to measure the overall effectiveness. Numerical simulations using realizable k-ε (RKE) turbulence model are applied to calculate the adiabatic effectiveness, internal heat transfer coefficient and overall effectiveness.

In Topic 1, we studied the turbine blade leading edge model film cooling effectiveness with shaped holes. It was found that, at low density ratio (DR = 1.0), 1.0R is little better than 1.5R, while 2.0R is the worst due to its higher surface curvature in the stagnation region. At high density ratio (DR = 2.0), 1.5R is the best, while 1.0R and 2.0R are about the same.

In Topic 2, we studied turbine blade leading edge internal heat transfer for normal and tangential impinging jets with mainstream. The influence of mainstream flow on heat transfer decreases with increasing jet Reynolds number.

In Topic 3, we studied turbine blade leading edge overall cooling effectiveness for normal and tangential impinging jets with mainstream. Numerical simulations overpredict overall effectiveness about 20% to 30%, and the difference between simulations and experiments is about 10% to 20% after the second row.

REFERENCES

1. Han, J. C., Dutta, S., and Ekkad, S., 2012, “Gas Turbine Heat Transfer and Cooling Technology,” CRC Press, Taylor & Francis Group, Florida.

2. Bogard, D. G., and Thole, K. A., 2006, "Gas turbine film cooling," J Propul Power, 22(2), pp. 249-270.

3. Han, J. C., 2013, "Fundamental Gas Turbine Heat Transfer," J Therm Sci Eng Appl, 5(2), p. 021007.

4. Goldstein, R. J., Eckert, E. R. G., and Burggraf, F., 1974, "Effects of Hole Geometry and Density on 3-Dimensional Film Cooling," International Journal of Heat and Mass Transfer, 17, pp. 595-607.

5. Ekkad, S.V., and Han, J.C., “A Review of Hole Geometry and Coolant Density Effect on Film Cooling,” Frontiers in Heat and Mass Transfer, Vol. 6, No. 8, 2015, pp. 1-14.

6. Luckey D. W., Winstanley, D. K., Hames, G. J., and L’Ecuiyer, M. R., 1977, “Stagnation Region Gas Film Cooling for Turbine Blade Leading-Edge Applications,” AIAA Journal of Aircraft, Vol. 14, pp. 494-501.

7. Mick, W. J. and Mayle, R. E., 1988, “Stagnation Film Cooling and Heat Transfer Including Its Effect Within the Hole Pattern,” ASME Journal of Turbomachinery, Vol. 110, pp. 66-72.

8. Mehendale, A. B. and Han, J. C., 1992, “Influence of High Mainstream Turbulence on Leading Edge Film Cooling Heat Transfer,” ASME Journal of Turbomachinery, Vol. 114, No. 4, pp. 707-715.

9. Ou, S., and Han, J. C., 1994, “Leading Edge Film Cooling Heat Transfer Through One Row of Inclined Film Slots and Holes Including Mainstream Turbulence Effect,” ASME Journal of Heat Transfer, Vol. 116, No. 3, pp. 561-569.

10. Reiss, H., and Bölcs, A., 2000, “Experimental Study of Showerhead Cooling on a Cylinder Comparing Several Configurations Using Cylindrical and Shaped Holes,” J. Turbomach., 122, pp. 161–169.

11. Kim, Y. J., and Kim, S. M., 2004, “Influence of Shaped Injection Holes on Turbine Blade Leading Edge Film Cooling,” Int. J. Heat Mass Transfer, 49, pp. 1287-1298.

12. Mouzon, B. D., Terrell, E. J., Albert, J. E., and Bogard, D. G., 2005, "Net Heat Flux Reduction and Overall Effectiveness for a Turbine Blade Leading Edge," ASME Paper No. GT2005-69002.

13. Lu, Y., Allison, D., and Ekkad, S. V., 2006, "Influence of Hole Angle and Shaping on Leading Edge Showerhead Film Cooling," ASME Paper No. GT2006-90370.

14. Gao, Z., and Han, J. C., 2009, "Influence of Film-Hole Shape and Angle on Showerhead Film Cooling Using PSP Technique," J. Heat Transfer, 131(6), p. 061701.

15. Li, S. J., Yang, S. F., and Han, J. C., 2014, "Effect of Coolant Denity on Leading Edge Showerhead Film Cooling Using the Pressure Sensitive Paint Measurement Technique," J. Turbomach., 136, 051011.

16. Cruse, M. W., Yuki, U. M., and Bogard, D. G., 1997, "Investigation of Various Parametric Influences on Leading Edge Film Cooling," ASME Paper No. 97-GT-296.

17. Chowdhury, N. H. K., Qureshi, S. A., Zhang, M. J. and Han, J. C., 2017, "Influence of turbine blade leading edge shape on film cooling with cylindrical holes," International Journal of Heat and Mass Transfer, 115(2017), pp. 895-908.

18. York, W. D., and Leylek, J. H., 2003, "Leading Edge Film-Cooling Physics–Part III: Diffused Hole Effectiveness," J. Turbomach., 125, pp. 165-187.

19. Beimaert-Chartrel, G., and Bogard, D. G., 2012, "CFD Predictions of Heat Transfer Coefficient Augmentation on a Simulated Film Cooled Turbine Blade Leading Edge," ASME Paper No. GT2012-70015.

20. Rutledge, J. L. and Polanka, M. D., 2014, "Computational Fluid Dynamics Evaluations of Unconventional Film Cooling Scaling Parameters on a Simulated Turbine Blade Leading Edge," J. Turbomach., 136, 101006.

21. Han, B., and Goldstein, R. J., 2001, "Jet-Impingement Heat Transfer in Gas Turbine Systems," Annals of the New York Academy of Sciences, Volume 934, pp.147-161.

22. Amano, R.S., Sundén, B, 2014, Impingement Jet Cooling in Gas Turbines, WIT Press.

23. Weigand, B. and Spring, S., 2011, "Multiple Jet Impingement –A Review," Heat Transfer Research, vol.42, no.2, pp. 101-142.

24. Wright, L.M., Han, J.C., 2013, ''Heat Transfer Enhancement for Turbine Blade Internal Cooling,'' ASME Paper No. HT2013-17813.

25. Chupp, R. E., Helms, D. E., McFadden, P. W., and Brown, T. R., 1969, "Evaluation of Internal Heat Transfer Coefficients for Impingement Cooled Turbine Airfoils," AIAA J. of Aircraft, Vol. 6(3), pp. 203-208.

26. Florschuetz, L.W. and Isoda, Y., 1982, “Flow distributions and discharge coefficient effects for jet array impingement with initial crossflow,” Journal of Engineering for Power, 105: 3.

27. Florschuetz, L.W., Truman, C.R., and Metzger, D.E., 1981, “Streamwise Flow and Heat Transfer Distributions for Jet Array Impingement with Crossflow,” ASME J. Heat Transfer, Vol. 103, pp. 337-342.

28. Florschuetz, L. W., Berry, R. A., and Mezger, D. E., 1980, “Periodic Streamwise Variations of Heat Transfer Coefficients for Inline and Staggered Arrays of Circular Jets with Crossflow of Spent Air,” ASME J. Heat Transfer, Vol. 102, pp.132–137.

29. Metzger, D. E., and Bunker, R. S., 1990, “Local Heat Transfer in Internally Cooled Turbine Airfoil Leading Edge Regions—Part I: Impingement Cooling Without Film Coolant Extraction,” ASME J. Turbomach. 112(3) 451-458.

30. Bunker, R. S., and Metzger, D. E., 1990, “Local Heat Transfer in Internally Cooled Turbine Airfoil Leading Edge Regions—Part II: Impingement Cooling With Film Coolant Extraction,” ASME J. Turbomach. 112(3) 459-466.

31. Taslim, M. E., Khanicheh, A., 2006, “Experimental and numerical study of impingement on an airfoil leading-edge with and without showerhead and Gill film holes,” ASME J. Turbomach. 128 (2006) 310–320.

32. Taslim, M.E., Bethka, D., 2009, “Experimental and numerical impingement heat transfer in an airfoil leading-edge cooling channel with cross-flow,” ASME J. Turbomach, vol. 131, pp. 011–021.

33. Liu, Z., and Feng, Z.P., 2011, “Numerical simulation on the effect of jet nozzle position on impingement cooling of gas turbine blade leading edge,” Int. J. Heat Mass Transfer, vol. 54, pp. 4949-4959.

34. Huang, Y., Ekkad, S. V., and Han, J. C., 1998, “Detailed Heat Transfer Coefficient Distributions Under an Array of Inclined Impinging Jets Using a Transient Liquid Crystal Technique,” 9th International Symposium on Transport Phenomenon in Thermal Fluids Engineering, ISTP-9, Singapore, June 25–28.

35. Ekkad, S.V., Huang, Y., and Han, J.C., 1999, "Impingement Heat Transfer on Target Plate with Film Cooling Holes,” AIAA J. Thermophysics and Heat Transfer, Vol. 13, No. 4, pp. 522-528

36. Jordan, C.N., Wright, L.M., and Crites, D.C., 2012, “Impingement Heat Transfer on a Cylindrical, Concave Surface with Varying Jet Geometries,” ASME Paper No. GT2012-68818.

37. Jordan, C.N., Wright, L.M., and Crites, D.C., 2012, “Effect of Impingement Supply Condition on Leading Edge Heat Transfer with Rounded Impinging Jets,” ASME Paper No. HT2012-58410.

38. Jordan, C.N., Elston, C.A., Wright, L.M., and Crites, D.C., 2013, “Leading Edge Impingement with Racetrack-shaped Jets and Varying Inlet Supply Conditions,” ASME Paper No. GT2013-94611

39. Yang, L., Kan, R., Ren, J. and Jiang, H. D., 2013, “Effect of Film Cooling Arrangement on Impingement Heat Transfer on Turbine Blade Leading Edge,” ASME Paper GT2013-95261.

40. Ling, J. P. C. W., Ireland, P. T., and Harvey, N. W., 2006, “Measurement of Heat Transfer Coefficient Distributions and Flow Field in a Model of a Turbine Blade Cooling Passage with Tangential Injection,” ASME Paper GT2006-90352.

41. Wang, N., Chen, A. F., Zhang, M. J., and Han, J. C, 2018, “Turbine blade leading edge cooling with one row of normal or tangential jets,” J. Heat Transfer., 140(6), 062201.

42. Hylton L.D., Milhec M.S., Turner E.R., Nealy D.A. and York R.E., “Analytical and Experimental Evaluation of the Heat Transfer Distribution Over the Surface of Turbine Vanes,” NASA CR 168015, 1983

43. Hylton L.D., Nirmalan V., Sultanian B.K. and Kaufman R.M., “The Effects of Leading Edge and Downstream Film Cooling on Turbine Vane Heat Transfer,” NASA CR 182133., 1988

44. E.R. Turner, M.D. Wilson, L.D. Hylton, R.M. Kauffman, Turbine vane external heat transfer. Volume 1: analytical and experimental evaluation of surface heat transfer distributions with leading edge showerhead film cooling, NASACR-174827, 1985.

45. Bohn, D. E., Ren, J., and Kusterer, K., 2003, “Conjugate Heat Transfer Analysis for Film Cooling Configurations With Different Hole Geometries,” ASME Paper No. GT2003-38369.

46. Kusterer, K., Hagedorn, T., Bohn, D., Sugimoto, T., and Tanaka, R., 2006, “Improvement of a Film-Cooled Blade by Application of the Conjugate Calculation Technique,” ASME J. Turbomach., 128, pp. 572–578.

47. Ramachandran, S. G., and Shih, T. I-P., 2015, “Biot Number Analogy for Design of Experiments in Turbine Cooling,” Journal of Turbomachinery, Vol. 137, 061002.

48. Albert, J. E., Bogard, D. G., and Cunha, F., 2004, “Adiabatic and Overall Effectiveness for a Film Cooled Blade,” ASME Paper GT2004-53998.

49. Maikell, J., Bogard, D., Piggush, J., and Kohli, A., 2011, "Experimental Simulation of a Film Cooled Turbine Blade Leading Edge Including Thermal Barrier Coating Effects," Journal of Turbomachinery, Vol. 133, 011014.

50. Dyson, T. E., Bogard, D. G., Piggush, J. D., and Kohli, A., 2013, "Overall Effectiveness for a Film Cooled Turbine Blade Leading Edge with Varying Hole Pitch," Journal of Turbomachinery, Vol. 135, 031011.

51. Dobrowolski, L. D., Bogard, D. G., Piggush, J., and Kohli, A., 2009, "Numerical Simulation of a simulated Film Cooled Turbine Blade Leading Edge Including Conjugate Heat Transfer Effects," IMECE2009-11670.

52. Ravelli, S., Dobrowolski, L. D., and Bogard, D. G., 2010, "Evaluation the Effects of Internal Impingement Cooling on a Film Cooled Turbine Blade Leading Edge," GT2010-23002.

53. Montomoli, F., Massini, M., Yang, H., and Han, J. C., 2012, "The benefit of high-conductivity materials in film cooled turbine nozzles," International Journal of Heat and Fluid Flow, Volume 34, p 107-116.

54. Chandran, D., and Prasad, B.,2015, "Conjugate Heat Transfer Study of Combined Impingement and Showerhead Film Cooling Near NGV Leading Edge," International Journal of Rotating Machinery, 315036.

55. Zhang, M. J., Wang, N., Chen, A. F., and Han, J. C., 2017, "Influence of Turbine Blade Leading Edge Profile on Film Cooling with Shaped Holes," J. Thermal Sci. Eng. Appl 10(5), 051006

56. York, W. D., and Leylek, J. H., 2002, "Leading Edge Film-Cooling Physics–Part I: Adiabatic Effectiveness," ASME Paper No. GT2002-30166.

57. York, W. D., and Leylek, J. H., 2002, "Leading Edge Film-Cooling Physics–Part II: Heat Transfer Coefficient," ASME Paper No. GT2002-30167.

58. Shiau, C. C., Chen, A. F., Han, J. C., Azad, S., and Lee, C.P., 2016, "Full-Scale Turbine Vane Endwall Film-Cooling Effectiveness Distribution Using Pressure-Sensitive Paint Technique," J. Turbomach., 138, 051002

59. Ekkad, S.V., and Han, J.C, 2000, "A transient liquid crystal thermography technique for gas turbine heat transfer measurements," Measurement Sci. Technol. Vol. 11 pp. 957–968.

60. Kline, S., and McClintock, F., 1953, "Describing Uncertainties in Single-Sample Experiments", Mechanical Engineering, 75(1), pp. 3 – 8.